MULTISCALE MODELING OF THE PROPERTIES OF TWO-DIMENSIONAL MATERIALS

by

Xiaonan Wang

A dissertation submitted to the faculty of
The University of North Carolina at Charlotte
in partial fulfillment of the requirements
for the degree of Doctor of Philosophy in
Mechanical Engineering

Charlotte

2017

Approved by:

Dr. Alireza Tabarraei

Dr. Qiuming Wei

Dr. Jordan C. Poler

Dr. David C. Weggel

ABSTRACT

XIAONAN WANG. Multiscale modeling of the properties of two-dimensional materials. (Under the direction of DR. ALIREZA TABARRAEI)

The main objective of this dissertation is to study the thermal and mechanical properties of two dimensional materials. For this purpose, we use and combine atomic level simulations with continuum level simulations. In this dissertation, molecular dynamics method is used to study the fracture properties of monolayer molybdenum disulfide (MoS_2) and hexagonal boron nitride (h-BN). Our results predict that the critical stress intensity factor of single layer MoS_2 and BN are 1.2$\sim$1.8 MPa$\sqrt{\text{m}}$ and 4.5$\sim$7 MPa$\sqrt{\text{m}}$ respectively. Moreover, our results predict that the chirality of the crack edges, the tip configuration and loading phase angle can significantly impact the critical stress intensity factor and the propagation path of the cracks.

Also, molecular dynamnics simulations are used to study the thermal conductivity of single layer MoS_2. The results show that by increasing the nanoribbon's length, the thermal conductivity of nanoribbons increases. For monolayer MoS_2, zigzag nanoribbons have higher thermal conductivity than armchair nanoribbons. Our results show that defect such as vacancies significantly impact the thermal conductivity of nanoribbons. By increasing the atomic vacancy density, the thermal conductivity of MoS_2 nanoribbon is reduced. We have studied the impact of uniaxial stretching on the thermal conductivity of MoS_2 nanoribbons. The MD simulations predict that, the thermal conductivity of MoS_2 is independent of the axial strain.

The high computation cost of MD simulations imposes severe constrains on the

size of modeling domain. To overcome this limitation, the molecular dynamics can be used only on the part of the domain which needs a high accuracy, while finite elements can be used in the rest of domain. Such coupling can reduce the computation cost but the artifacts associated with the presence of an interface between MD and FE zone should be removed. In this dissertation, a coupling technique is presented to alleviate the atomic-continuum interface effect. The proposed method is based on the bridging domain method (BDM). Using numerical examples, we show that the proposed method significantly improves the performance of bridging domain method. This is specially significant when discontinuities such as cracks are present in the domain or when the integration time step is small.

Since the finite element method is a mesh-based method, special techniques are required to simulate the fracture phenomenon. For example, a common way is to split a cracked element into two new elements. However, this method requires the re-meshing, which is not only time consuming, but also reduces the accuracy. Peridynamics is a more recently developed technique, which can resolve the issues associated with modeling cracks using FEM. In a peridynamics formulation, the domain is discretized by node only. Thus, without the re-meshing, the peridynamics can simulate the fracture phenomenon. In this dissertation, the peridynamics method is used to simulate the fracture behavior of the single layer MoS_2 and h-BN, at a continuum level.

Since peridynamics is a nonlocal method, computationally, it is more expensive than FEM. To reduce the computational cost, we propose to couple PD with FEM. In this coupling technique, the peridynamics method is used to simulate the part

which (may) contains cracks, while the finite element method is used for the rest domains. Two dimensional and three dimensional examples are used to verify the performance of the proposed method.

ACKNOWLEDGMENTS

First I would like to thank the significant help and guidance from Dr. Alireza Tabarraei. Second, I would like to thank the corporation and technique support from the Corvid Technologies. Third, I acknowledge the source of financial assistance from the University of North Carolina, NASA, NSF, and the Charlotte Research Institute.

TABLE OF CONTENTS

LIST OF FIGURES

LIST OF TABLES

CHAPTER 1: INTRODUCTION

1.1 MoS_2 and h-BN

The advent of nanotechnology provides the tools to create materials which is composed of only one or few layers of atoms [78, 81]. Such so-called two dimensional (2D) materials exhibit properties different from their counterpart three dimensional (3D) materials. Graphene is the first exfoliated two dimensional material. It contains only one layer of carbon atoms and is nearly transparent. It has a high thermal conductivity (5300 W/mK). It is one of the strongest material, with a 1 TPa Young's modulus. It is a zero-gap semiconductor. It is under development in the areas of electronics, biological engineering, filtration, lightweight and strong composite materials, photovoltaics and energy storage.

Monolayer molybdenum disulfide (MoS_2) is a more recently exfoliated graphene-like two dimensional material, in which two atomic layers of sulfur (S) encompass a close-packed layer of molybdenum (Mo) (see figure 1 and 2). Single layer MoS_2 displays an excellent electrical and optical properties which makes it appealing for a wide range of applications, such as flexible optoelectronic devices, photodetectors, integrated logic circuits, field effect transistors sensors and semiconductors [113, 161, 63].

Hexagonal boron nitride (BN) is another graphene-like two dimensional material. It has a honeycomb atomic structure in which boron (B) and nitrogen (N) atoms occupy

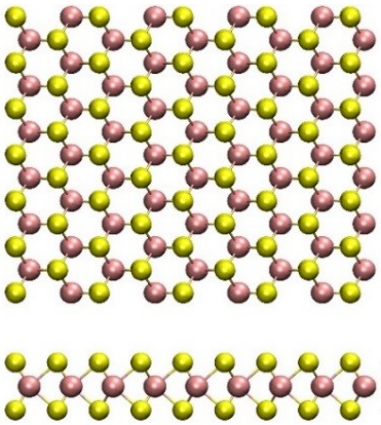

Figure 1: Atomic structure of MoS_2 from the top view.

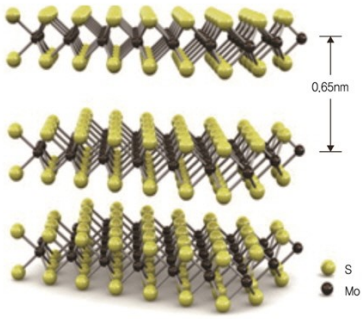

Figure 2: Atomic structure of MoS_2 from the side view.

alternating sites (see figure 3 and 4). BN shows remarkable physical and mechanical properties such as low dielectric constant, high temperature stability, high thermal conductivity and high strength [37, 126, 20].

To ensure that nano devices contains these materials preserve their structural integrity during the service time, it is necessary to gain a fundamental understanding of the fracture properties of monolayer MoS_2 and h-BN. Moreover, various potential application of these materials demand different requirements of the thermal properties. It is necessary to fundamentally understand the thermal transfer quality of these materials.

In this study, the atomic and continuum level methods are used to investigate the

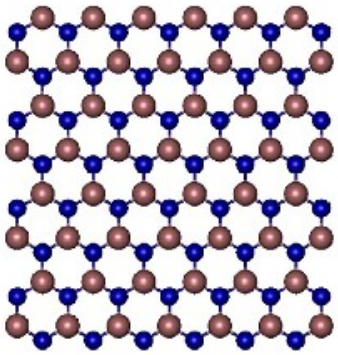

Figure 3: Atomic structure of h-BN from the top view.

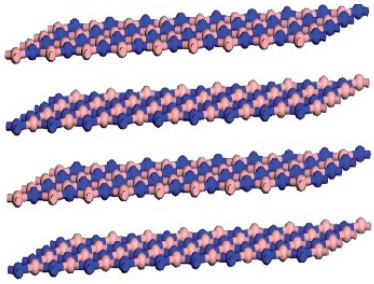

Figure 4: Atomic structure of h-BN from the side view.

fracture properties of single layer MoS_2 and h-BN under mixed-mode loading. The Nonequilibrium Molecular Dynamics (NEMD) method is used to study the thermal properties of MoS_2.

1.2 Brief review of molecular dynamics method

Molecular dynamics is a powerful tool of studying the mechanical, chemical and electrical properties of materials by simulating the physical movements of atoms and molecules.

In molecular dynamics, the atoms are the basic components. The interaction between atoms are considered using interatomic potentials. Different potentials have been developed in the past for different materials. In this study, we use (1) the AIREBO potential for the fracture study of MoS_2 [85]; (2) the SW potential for the

thermal conductivity study of MoS_2 [58] and (3) the Tersoff potential for the fracture and thermal studies of h-BN [139]. More details of the potentials and the reason we choose these potentials can be found in chapter 2, 3 and 4.

Based on proper potential, molecular dynamics can represent atomic level phenomena. It can be used to study the material's response under different scenarios, for example, different loading rates, temperatures, mix-mode loadings, different chiral directions, different configurations and so on. It is very challenging to apply or observe these nano-scale scenarios in the experiments. Thus, molecular dynamics is a powerful tool to explore the nano-scale mechanism of many experimental phenomenon. Moreover, the molecular dynamics simulation can even predict the materials property earlier than the experimental observation. For example, our study of the fracture property of single MoS_2 layer was later proved by the experimental studies [147].

In this study, the LAMMPS [76] package is used to conduct the molecular dynamics simulations of chapter 2, 3 and 4. LAMMPS is an open source code distributed by Sandia National Laboratories. It is a widely used molecular dynamics package for large scale parallel simulations. All the simulations are performed by the super computer clusters at the University of North Carolina at Charlotte.

1.3 Brief review of peridynamics method

Peridynamics is a nonlocal method, which is developed to resolve some of the deficiencies of classical continuum in modeling damage. In peridynamics, the equation of motion for a point is:

$$\rho(X)\ddot{d}(X,t) = b(X,t) + \int_H (T[X,t]\langle X' - X\rangle - T[X',t]\langle X - X'\rangle)dV_{X'}, \qquad (1)$$

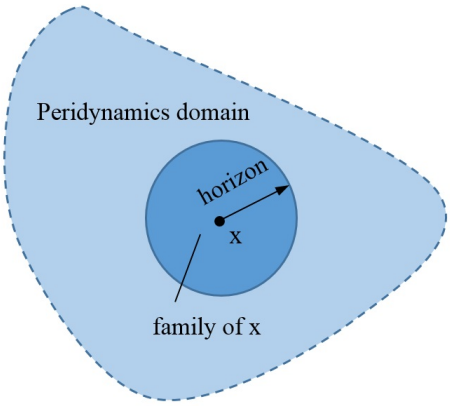

Figure 5: The motion of a point x is based on an integration over its family. The radius of the family domain is called the horizon.

where ρ is the mass density, $\ddot{u}$ is the acceleration, X is the original coordinate of the current position and X' is the position of a neighbor point within the family of X, t is the time and b is the body force density. $T[X,t]\langle X'-X\rangle$ is the force state, which determines the interaction forces between the pairs of points.

1.4 Coupling the molecular dynamics and finite element methods

Finite Element Method (FEM) is a widely used numerical method which can do the simulation of continuous problems with very high efficiency. Since, FEM is based on the gridded mesh and elements, it is very simple to detect the free surfaces, which are the surfaces who only have one attached element. As a result, it can simulate the contact problem with a high accuracy. However, without advanced enrichments [99], FEM can not simulate the discontinuity naturally. One common way to represent the failure and fracture is to delete the element when its failure criterion is reached [55, 62, 57]. This method lead to the non-convergency of the global mass and energy. Another common way to let the crack propagate is to split the nodes and elements, this method requires the remeshing during the simulation and is computationally expensive [17,

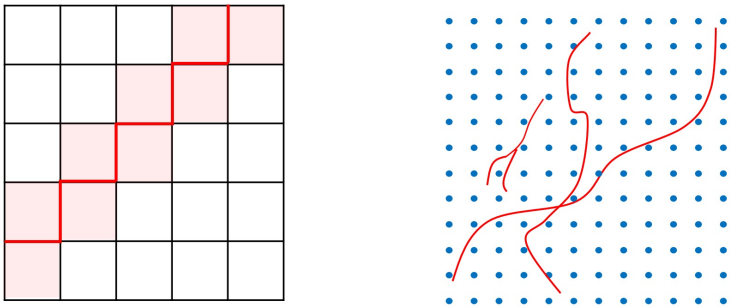

(a) (b)

Figure 6: (a) In FEM, the cracks propagation direction is in the compliance with the mesh. (b) In PD, the crack can propagate by cutting through interaction between points.

64, 127]. Whats more, the cracks propagation direction is in the compliance with the mesh, which reduces the accuracy of the simulation. (Figure 6(a))

On the other side, for the molecular dynamics, it allows the discontinuity to pass through the interactions of particles and the direction of the cracks propagation can be arbitrary. Thus these methods can simulate the crack's propagation and nucleation naturally without remeshing (figure 6(b)).

Molecular dynamics simulations provide vast amount of information about material behavior at nanoscale. They have been particularly used to study how defects such as cracks, grain boundaries or dislocations affect macroscale processes such as elasticity or plasticity. However, the high computational costs associated with atomistic simulations limit their applicability to systems made of limited number of atoms. Coupled atomistic-continuum methods have been introduced as a remedy to this limitation. In the coupled methods, full atomistic resolution is maintained where deformations are highly inhomogeneous (e.g., at the vicinity of defects) and continuum models are used elsewhere [136, 96, 132, 118, 119, 2, 21, 144, 11, 152, 40, 122, 84, 121, 155, 15]. The

challenge lies in appropriate gluing of atomistic and continuum zones such that the atomistic region behaves as if the entire domain is atomistic. To achieve this objective, the effects of the atomistic-continuum interface should be minimized. In static problems ghost forces can be generated at the coupling interface [91] and a number of techniques have been developed to overcome this issue [11, 40]. In dynamic problems an additional difficulty related to the passage of the propagating wave from atomistic to continuum across the interface is encountered; the change of the constitutive equations from inherently nonlocal atomistic to local continuum along with the change of the resolution from atomistic to continuum lead to spurious wave reflection at the interface. Since in the coupling methods atomistic zone usually has a small size, the spuriously reflected wave can quickly increase the temperature of atomistic zone, whereby destroys the simulation. To avoid the spurious wave reflections, the interface between the atomistic and continuum should be such that coarse scale information (low frequency waves) can be accurately transmitted in both directions, whereas the fine scale oscillations which cannot be transmitted into the continuum zone should be eliminated at the interface. Several such interfaces have been developed in the past, among those are coarse-grained molecular dynamics (CGMD) method [118, 119], macroscopic-atomistic-ab initio dynamics (MAAD) method [2, 21], bridging scale method (BSM) [144, 143], bridging domain method (BDM) [11, 152], concurrent AtC coupling method [40, 8], embedded statistical coupling method (ESCM) [122] and heterogeneous multiscale method (HMM) [33, 34]. Reviews on concurrent atomistic-continuum multiscale methods can be found in [27, 98].

Belytschko et al. [11, 152] developed a bridging domain method (BDM) to couple

continuum mechanics with molecular models. Bridging domain method lies in the category of overlapping domain decomposition coupling methods, or Arlequin method, which has been developed earlier by Ben Dhia [13, 10]. This method has been used for modeling cracks and defects in graphene and carbon nanotubes [11, 152, 165, 164] and has been combined with extended finite element method (XFEM) [100] to study crack propagation and dislocation emission in nanomaterials [44, 104]. More recently, BDM applications are extended to multiscale analysis at finite temperature [6, 120].

In the bridging domain method, continuum and atomistic domains overlap in a bridging (handshaking) domain where a weight function is used to partition the atomistic and continuum energy. In the overlapping domain, the positions of atoms and nodes are not necessarily coincident and the compatibility between atomistic and continuum domain is imposed by Lagrange multipliers. This allows to use a uniform mesh in the entire domain and removes the need for mesh refinement in the overlapping region.

In this dissertation, The impact of the discretization of Lagrange multipliers and the time integration step size, on the performance of BDM method is studied. The new technique is proposed.

1.5 Coupling the peridynamics and finite element methods

Peridynamics is more computational expensive than FEM. To reduce the computational cost, we propose to couple FEM and peridynamics. Some previous studies discussed some simple ways to couple FEM and peridynamics. For example, Erkan etl. studied a submodeling approach in which the boundary conditions of peridy-

namics are imported from FEM [107]. However they assume that the submodeling details do not affect the FEM simulation and the boundary of the peridynamics is far enough from the local features. Richard and Steward studied a way to implement the peridynamics model in a conventional FEM code [92]. To save the computational time, the displacement constraint between the FEM and peridynamics is applied in a "fuzzy" zone [92]. Liu developed an interface element, in which the embedded points are firmly attached to the interface element, while the interaction force between the embedded points and the normal points are divided and assigned to the nodes of the interface elements [88]. Similar studies have been done by [41, 65, 115]. These coupling ideas are very similar: the overlapping zone of FEM and peridynamics is divided into two parts. In one part, peridynamics points move following the FEM, in the other part, the FEM nodes move following the peridynamics points. The attachment criterion can be based on displacement or force. However, these simple ways of coupling are only tested under the quasi-static loadings. In a real-world, for example, a bullet hitting a shield, or in an explosion, the loadings can be much more complex. In these cases, the coarsely meshed FEM zone can not resolve the high frequency waves coming from the finely meshed peridynamics zone. Thus the high frequency waves will be reflected back to the peridynamics zone and a redundant energy is introduced and trapped inside the peridynamics. The redundant energy leads to a subcritical nucleation or propagation of crack, it also may cause the failure near the coupling zone [135].

In this dissertation, peridynamics is used in the zones where fracture may occur and FEM is used in the rest of the domain. The purpose is to propose a seamless

coupling methodology of FEM and peridynamics. In this method, not only the load can be transferred from FEM, the FEM can also feel the feedback from peridynamics simultaneously. The loading is able to be a high rate dynamic loading. The mesh of the peridynamics and the overlapping can be generated easily without much artificial effort. At the end, the peridynamics can be linked to a FEM software to simulate real world problems by a general backgrounded user.

CHAPTER 2: MOLECULAR DYNAMICS STUDY OF THE FRACTURE BEHAVIOR OF MOS_2

2.1 Introduction

Monolayer molybdenum disulfide (MoS_2) is a recently exfoliated two dimensional material in which two atomic layers of close-packed sulfur (S) encompass a close-packed layer of molybdenum (Mo) (see figure 1 and 2). Monolayer MoS_2 displays excellent electrical and optical properties which makes it appealing for a wide range of applications, such as flexible optoelectronic devices, photodetectors, integrated logic circuits, field effect transistors and sensors [160, 113, 93, 56, 110, 146]. Its semiconducting nature [94] allows it to overcome the zerobandgap of graphene, while still sharing many of graphenes advantages for electronic applications [106, 9]. Besides fantastic physical properties, its remarkable mechanical properties such as high Young's modulus and high flexibility [80] make it a promising candidate as a filler in nanocomposite materials.

To ensure that nanodevices and nanomaterials designed based on monolayer MoS_2 preserve their structural integrity during fabrication and service time, it is necessary to gain a fundamental understanding of the mechanical properties of monolayer MoS_2. In particular, to predict and prevent mechanical failure in the form of cracks, it is essential to understand the failure properties of monolayer MoS_2.

In contrast to three dimensional materials whose fracture properties have been

widely studied, research on the fracture properties of two dimensional (2D) materials is scarce. Most of the studies on the fracture properties of 2D materials are limited to graphene [155, 162, 31, 77, 54], fracture properties of other 2D materials have been rarely investigated. The failure mechanisms of MoS_2 are more complex than those of graphene. This is mainly due to the more complicated atomic structure of MoS_2. MoS_2 has a binary system (composed of two elements) and in contrast to graphene, which has a truly planar structure, a single sheet of MoS_2 has a triple-layered atomic structure. These differences in the atomic structure necessitate separate investigations of the failure mechanism of monolayer MoS_2.

2.2 Review of the REBO potential

The interactions among the atoms are modeled using a reactive empirical bond order (REBO) potential [85]. The REBO potential has the form:

$$E_b = \frac{1}{2}\sum_{i\neq j} f_{ij}^C(r_{ij})[V^R(r_{ij}) - b_{ij}V^A(r_{ij})] = \frac{1}{2}\sum_{i\neq j} f_{ij}^C(r_{ij})[(1+\frac{Q}{r_{ij}})A\cdot e^{-\alpha\cdot r_{ij}} - b_{ij}B\cdot e^{-\beta\cdot r_{ij}}], \tag{2}$$

where E_b is the binding energy of a system and r_ij is the distance between atoms i and j. $V^R(r_{ij})$ and $V^A(r_{ij})$ are the pairwise repulsion and attraction, respectively. $f_{ij}^C(r_{ij})$ is the cutoff function and b_{ij} is the bond-order term. The bond-order term can be regarded as a measure of bond strength, which is determined by the many-body interactions of the environment on an atom. Two cutoff distances R_{min} and R_{max} are used to allow a smooth transition of cutoff function from one to zero.

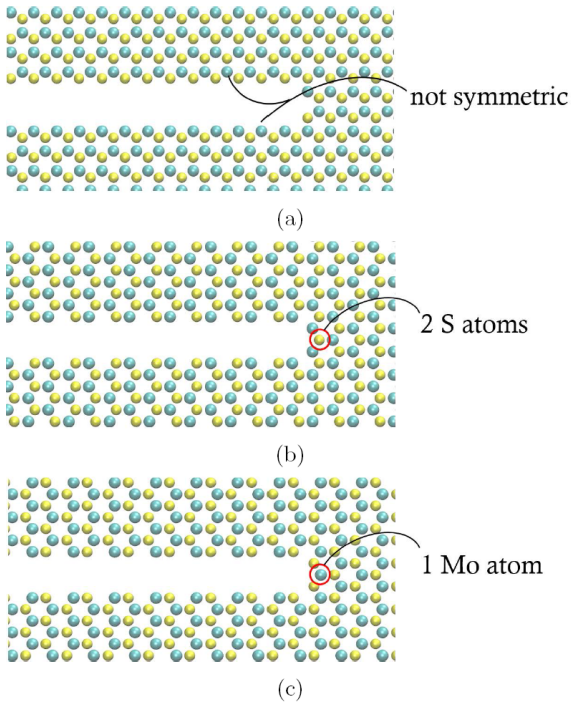

Figure 7: Three types of cracks: (a) zigzag crack, (b) armchair crack with two S atoms at the crack tip and (c) armchair crack with one Mo atom at the crack tip.

2.3 Geometry of the examples

Our MD model is a square domain with side lengths of 110 $\mathring{A}$, consisting of about 4700 atoms. There are three types of cracks: zigzag crack, armchair crack with a Mo atom at the crack tip and armchair crack with two S atoms at the crack tip (see figure 7). These three types of cracks are initially generated by removing three or four layers of atoms, respectively. Due to the lattice structure of MoS_2, the edges of zigzag cracks are not symmetric: one edge is composed of two S atoms at its outermost atomic layer while the other surface is made of Mo atoms. On the other hand, the surfaces of armchair cracks are symmetric. The effects of the crack tip structure on its toughness are studied here.

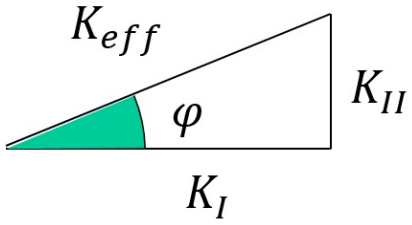

Figure 8: The loading phase angle is used to represent the ratio between K_{I} and K_{II}.

2.4 Mixed-mode loading of the examples

The molecular dynamics simulations are performed by applying crack tip asymptotic displacement fields to the outermost layers of atoms shown in figure 9. We have assumed that the far field behavior is linear and isotropic since the crack tip strain field reduces rapidly and MoS_2 behavior is anisotropic only under large strains [26, 79]. The crack tip asymptotic displacement fields for a linear isotropic material under mixed mode I and II of fracture is given by

$$u_x = \frac{1+\upsilon}{E}\sqrt{\frac{r}{2\pi}}[K_{\mathrm{I}}^{\mathrm{app}}\cos\frac{\theta}{2}(\kappa - 1 + 2\sin^2\frac{\theta}{2})] + K_{\mathrm{II}}^{\mathrm{app}}\sin\frac{\theta}{2}(\kappa + 1 + 2\cos^2\frac{\theta}{2}) \tag{3a}$$

$$u_x = \frac{1+\upsilon}{E}\sqrt{\frac{r}{2\pi}}[K_{\mathrm{I}}^{\mathrm{app}}\sin\frac{\theta}{2}(\kappa + 1 - 2\sin^2\frac{\theta}{2})] - K_{\mathrm{II}}^{\mathrm{app}}\cos\frac{\theta}{2}(\kappa - 1 - 2\sin^2\frac{\theta}{2}) \tag{3b}$$

When the mode I and mode II are mixed, we use the loading phase angle to represent the ratio between $\mathrm{K_I}$ and $\mathrm{K_{II}}$: $\phi = \mathrm{atan}\frac{K_{\mathrm{II}}^{\mathrm{app}}}{K_{\mathrm{I}}^{\mathrm{app}}}$, as figure 8 shown. Thus, a loading phase angle of 0° corresponds to a pure mode I loading and a loading phase angle of 90° corresponds to a pure mode II loading.

The material coefficient of single layer MoS_2 is shown in table 1.

The boundary conditions are applied incrementally in increments of $\Delta K_{\mathrm{eff}}^{\mathrm{app}} = 0.01$ $\mathrm{MPa}\sqrt{\mathrm{m}}$. After each loading increment, the position of the boundary atoms are kept

Table 1: Material coefficient of single layer MoS_2 for generating the displacement field on the boundary.

Young's modulus	200 GPa
Poisson's ratio	0.29

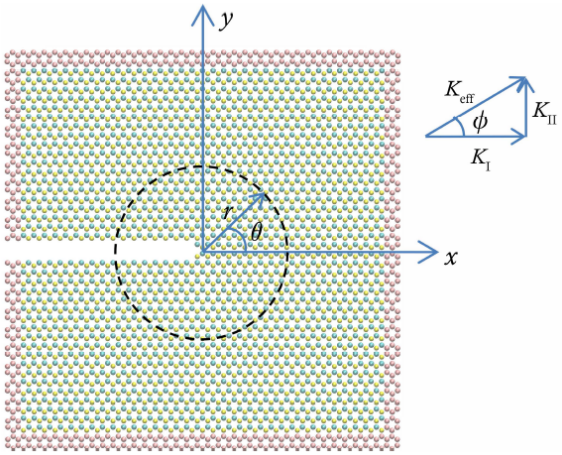

Figure 9: A pre-cracked MoS_2 sheet. The asymptotic crack tip displacement fields are applied to the boundary atoms shown in red.

fixed while the position of internal atoms are relaxed for 60000 time steps, which corresponds to a strain rate of 5×10^{-5} ps^{-1}. The velocity-Verlet scheme with a time step of 1 fm is utilized for the purpose of time integration.

To obtain the critical stress intensity factors, the bonds lengths are checked at the end of each load increment. If the length of any bonds at the crack tip is larger than the R_{max} (equal to 3.05 Å for Mo−S interactions), the bonds are considered broken, and the K_{eff}^{app} corresponding to that load increment is considered as the critical stress intensity factor (K_{eff}^{cr}). All the MD simulations are conducted using LAMMPS package and a Nosé-Hoover thermostat is used to maintain the temperature at 300 K.

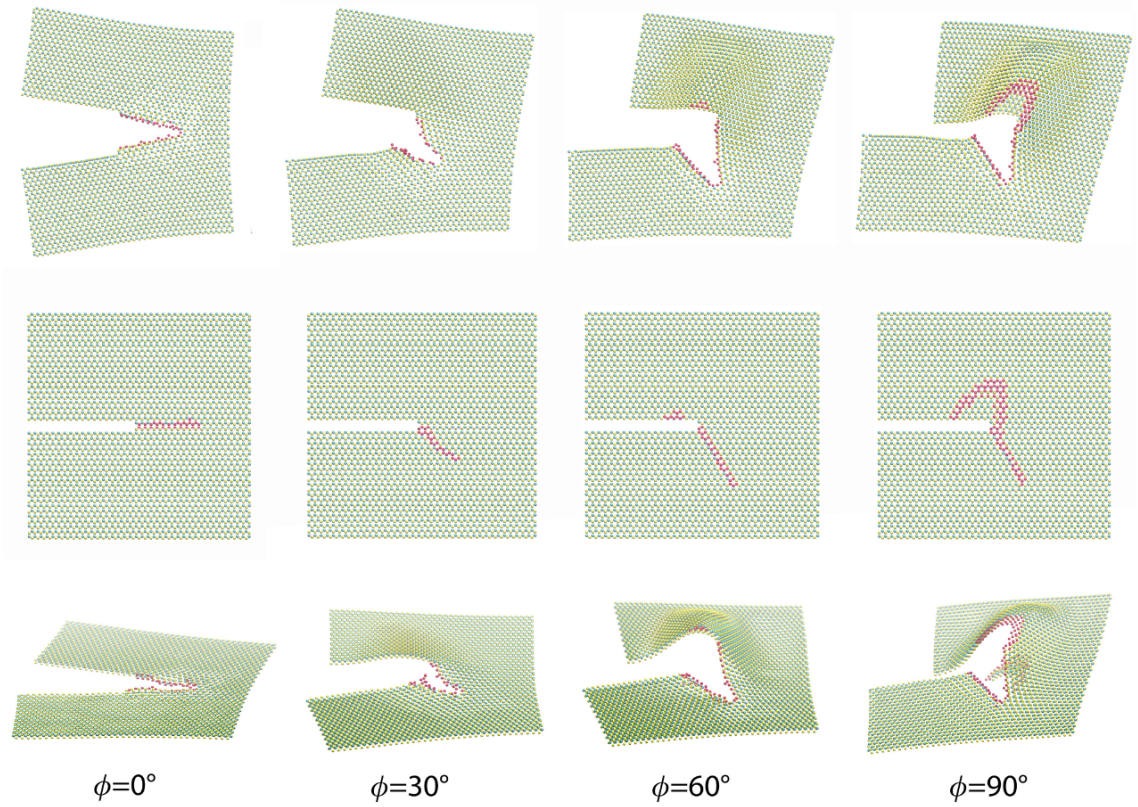

Figure 10: Crack propagation path of zigzag cracks. The first row is shown in the deformed configuration, the second row is shown in the undeformed configuration and the third row is shown in the out of plane deformation.

2.5 Simulation results

The crack propagation paths of zigzag cracks under mixed-mode loading are shown in figure 10. When the loading phase angle is not zero, the crack extends via a kink forming at an angle with the initial crack. The kink angle depends on the mixed mode phase angle and by increasing the phase angle, the kind angle also increases. The crack trajectories of an armchair cracks with two S atoms at the crack tip shown in figure 11. These figures indicate that even under pure mode I loading (opening load), armchair cracks propagate via a kink. Similar to zigzag cracks, an increase in the loading phase angle leads to increase in the kink angle. Investigation of the crack

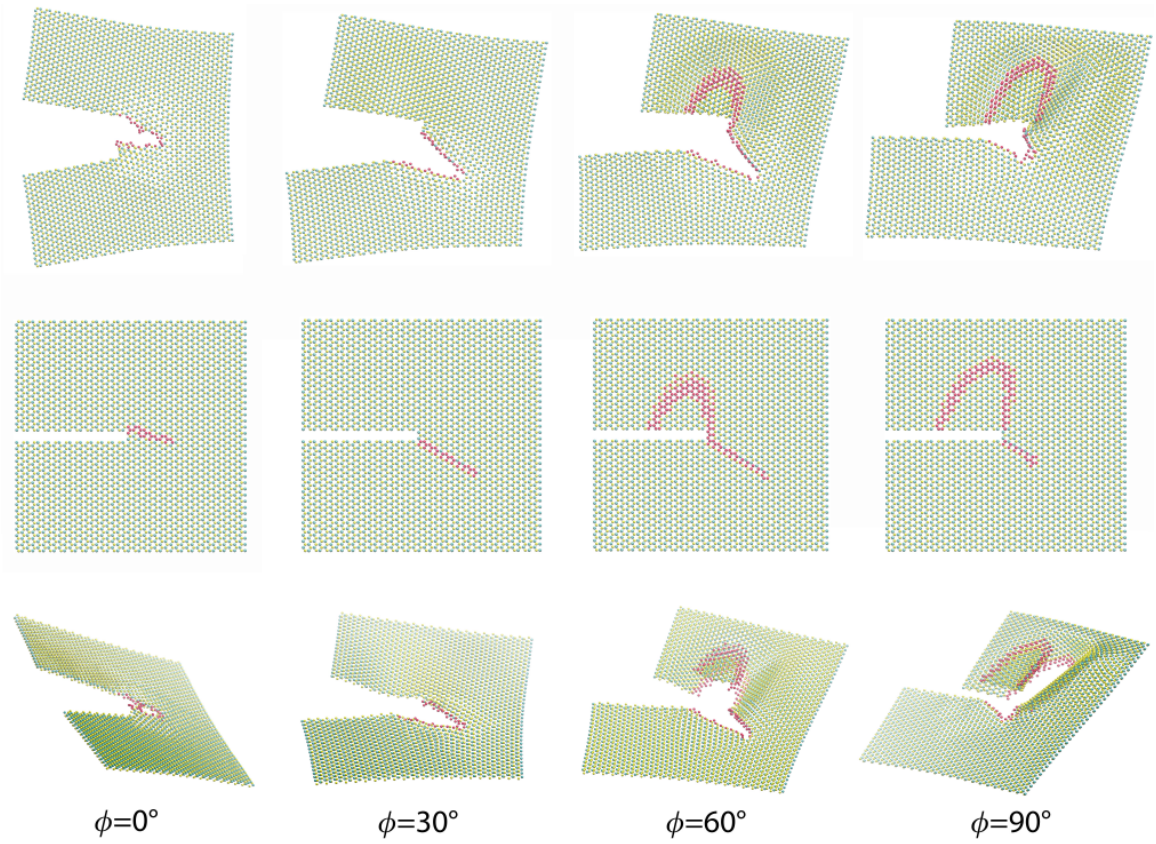

Figure 11: Crack propagation path of armchair cracks with two S atoms at the crack tip. The first row is shown in the deformed configuration, the second row is shown in the undeformed configuration and the third row is shown in the out of plane deformation.

propagation paths of armchair and zigzag cracks shows that both cracks propagate mostly along a zigzag surface, suggesting that zigzag crack has a smaller surface energy than armchair crack. For the armchair cracks with a Mo atom at the crack tip, the results are very similar as figure 11 shows. This observation is later proved by experimental studies [147].

The crack tip configurations under the pure mode I critical stress intensity factors are shown in figure 12 , in both the deformed and undeformed configuration. The very first broken bonds are shown in red demonstrating that under mode I loading, the crack propagates by braking Mo-S bonds at the crack tip.

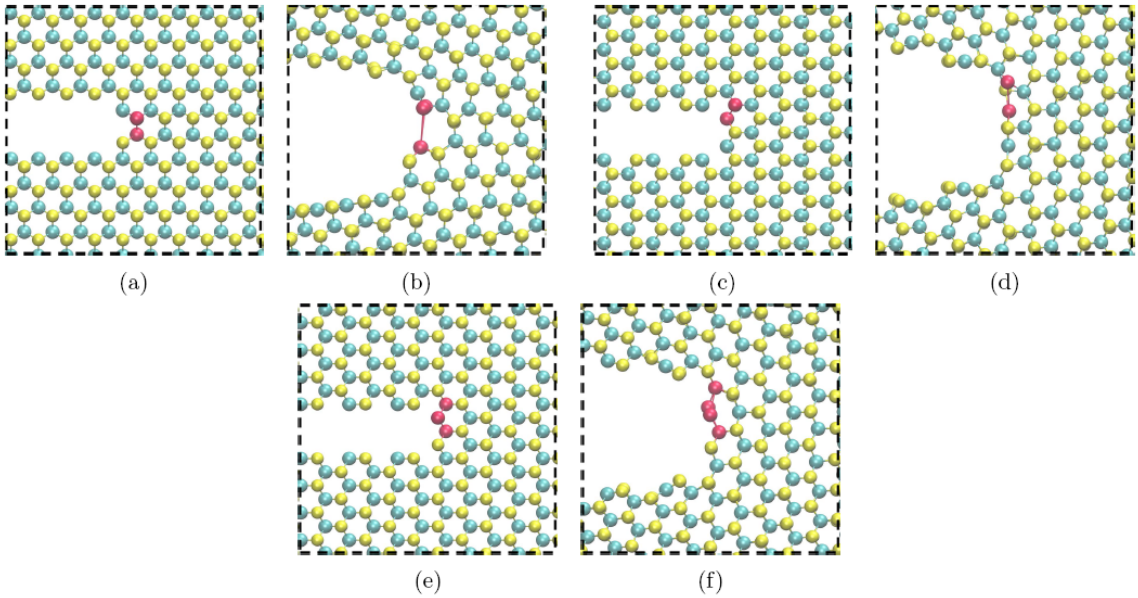

Figure 12: Snapshots near the crack tips at the critical stress intensity factors for (a) zigzag crack in a undeformed shape, (b) zigzag crack in a deformed shape, (c) armchair with two S atoms at the crack tip in a undeformed shape, (d) armchair crack with two S atoms at the crack tip in a deformed shape, (e) armchair crack with a Mo atom at the crack tip in a undeformed shape. (f) armchair crack with a Mo atom at the crack tip in a deformed shape.

It can be seen in figure 10 and 11 that when loading phase angle is large, which means when the mode II loading is dominant, the MoS_2 sheet undergoes the out-of-plane buckling. The buckling is due to the compressive stress generated by mode II component of loading. Since the thickness of the MoS_2 sheet is very small, the compressive stress induces out-of-plane deformation (buckling), a phenomenon reminiscent of buckling of thin cracked plates under tensile and shear loading. The magnitude of out-of-plane buckling is shown in figure 13, which clearly shows that the out-of-plane deformation is negligible when mode I component is dominant and becomes more severe when the phase angle increases.

As are shown in figure 10 and 11, if the out-of-plane buckling is excessive, buckling cracks nucleate away from the surface of the initial crack. The buckling cracks might

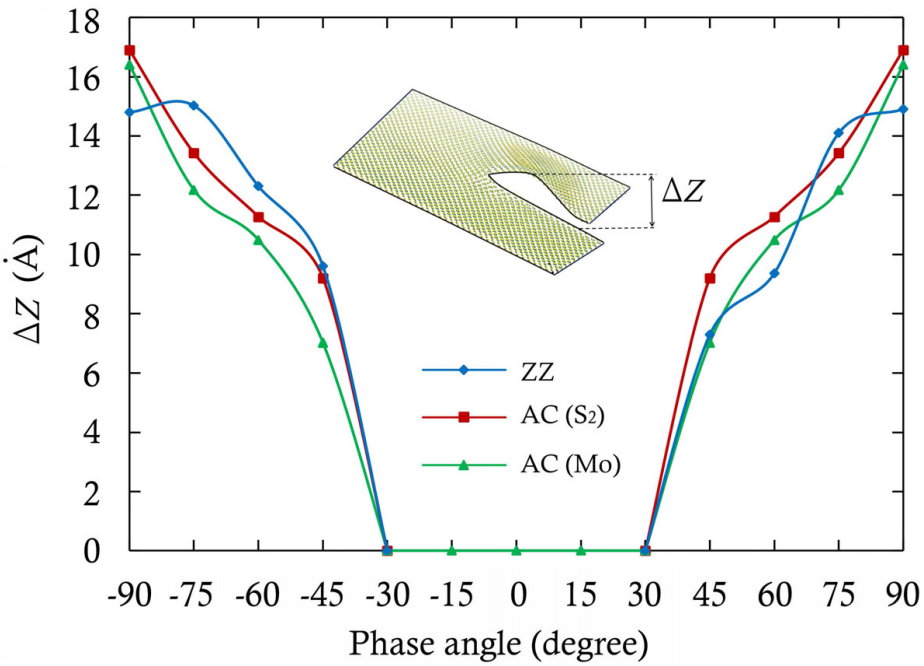

Figure 13: Maximum difference of the coordinates in the z-direction.

nucleate before or after the initial crack advances. In this dissertation, for each loading phase, two critical stress intensity factors are reported. One corresponds to the critical stress intentisy factor at which the initial crack propagates ($K_{\text{cp}}^{\text{cr}}$) , and the other corresponds to the critical stress intensity factor at which a bond breaks due to the buckling ($K_{\text{bp}}^{\text{cr}}$) of a crack surface.

Table 2: Critical stress intensity factors $K_{\text{eff}}^{\text{cr}}(\text{MPa}\sqrt{\text{m}})$ of cracks at different loading phase angles. The number in black corresponds to the stress intensity factor at which the initial crack propagates. The numbers in purple corresponds to the value at which the buckling crack nucleates.Critical stress intensity factors $K_{\text{eff}}^{\text{cr}}$ $(\text{MPa}\sqrt{\text{m}})$ of cracks at different loading phase angles. The number in black corresponds to the stress intensity factor at which the initial crack propagates. The numbers in purple corresponds to the value at which the buckling crack nucleates.

ϕ		**0°**	**15°**	**30°**	**45°**	**60°**	**75°**	**90°**
$\mathbf{K_{eff}^{cr}}$	**ZZ**	1.3	1.3	1.3	1.5 (4.6)	1.2 (2.9)	1.8 (2.5)	1.3 (2.3)
	ZZ(neg)	1.3	1.7	1.4	1.8 (4.0)	1.5 (2.8)	1.6 (2.7)	1.2 (2.8)
$(\mathbf{MPa}\sqrt{\mathbf{m}})$	**AC-S**	1.8	1.8	1.3	1.8 (4.0)	1.5 (3.2)	1.6 (2.0)	1.8 (2.2)
	AC_Mo	1.5	1.3	1.3	1.5 (5.7)	1.3 (4.5)	1.2 (2.5)	1.6 (2.6)

The critical effective stress intensity factors of the armchair and zigzag cracks are presented in figure 14 and table 2. Due to the unsymmetry of the zigzag crack edges, the loading phase angles is varied from the -90° to 90°. Plots of figure 14 show that the $K_{\mathrm{cp}}^{\mathrm{cr}}$ of armchair crack with two S atoms at its crack tip is larger than that of armchair cracks with one Mo atom at its crack tip. This is mainly due to different interatomic interactions between the Mo-Mo and S-S atoms in MoS_2. In the current potential, the cut-off distance of Mo-Mo interactions is 3.8 $\mathring{A}$ whereas the cut-off distance of S-S interactions is just 3.0 $\mathring{A}$. In an armchair crack with one Mo atom at the crack tip, the distance between the four S atoms at the immediate vicinity of the tip (see figure 12) is larger than S-S cut-off distance, hence they don't interact with each other. On the other hand, if two S atoms are located at the crack tip, the distance between the two Mo atoms located in the immediate vicinity of the crack tip (see figure 12) is less than their cut-off distance, hence they interact with each other. Due to this extra interatomic interaction, more energy is required to deform the crack tip neighborhood which in turn leads to an increase in the crack toughness.

Plots of figure 14 also indicate that in general $K_{\mathrm{cp}}^{\mathrm{cr}}$ of zigzag cracks are larger when the crack surface with Mo atoms at its outermost layer is under compression, i.e., loading phase angle is less than zero. Furthermore, comparing $K_{\mathrm{cp}}^{\mathrm{cr}}$ of armchair and zigzag cracks show that under pure mode I loading, armchair cracks are tougher than zigzag cracks.

When the loading phase angle is smaller than 45°, i.e., when mode I loading is dominating, no buckling crack is observed. By increasing the loading phase angle, the magnitude of the out-of-plane deformation increases and buckling cracks nucleate.

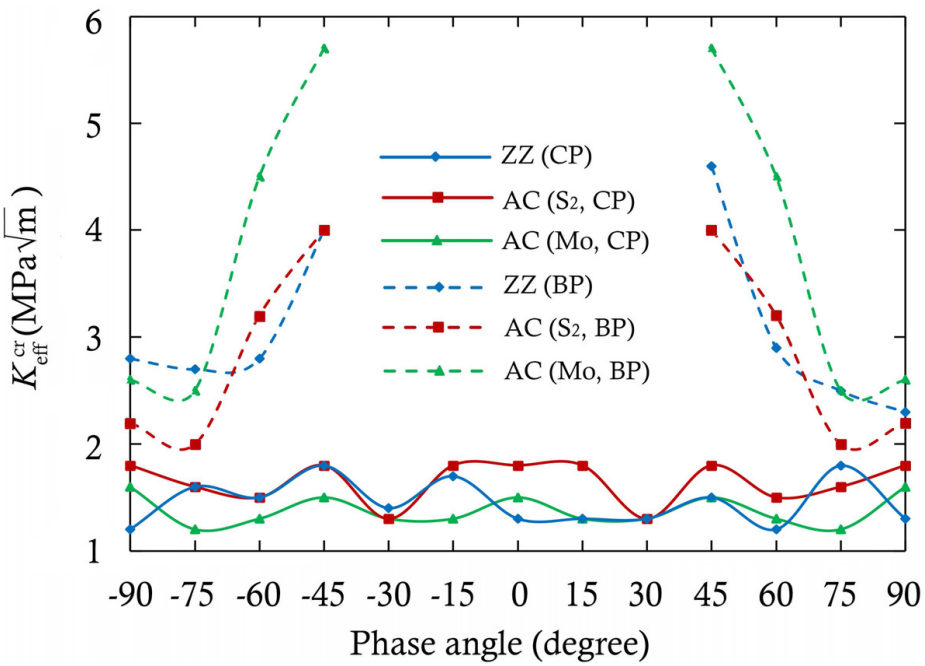

Figure 14: Critical stress intensity factors of armchair and zigzag cracks. K_{cp}^{cr} are shown with solid lines they represent the moment when the initial crack is about to propagate. K_{BP}^{cr} are shown with the dashed lines, they represent the moment when the buckling is about to occur.

Plots of figure 14 show that by increasing the loading phase angle, the magnitude of the $K_{\text{cp}}^{\text{cr}}$ reduces. The intersection point of the dashed curves and their corresponding solid lines represent the loading phase angle at which the nucleation of the bucking crack and the propagation of the initial crack occur simultaneously.

2.6 Conclusion

Our molecular dynamics simulations predict that, similarly to graphene, both the armchair and zigzag cracks prefer to propagate in the direction which makes a new zigzag crack. The critical stress intensity factors for MoS_2 sheets are in the range of $K_{\text{cp}}^{\text{cr}} = 1 \sim 2.5$ MPa$\sqrt{\text{m}}$. Buckling cracks have been observed. Buckling cracks develop only if the loading phase angle is larger than 45°.

CHAPTER 3: MOLECULAR DYNAMICS STUDY OF THE FRACTURE BEHAVIOR OF H-BN

3.1 Introduction

The current interest to graphene and the need to introduce an electronic bandgap to the gapless pristine graphene has brought intense interests to other graphene-like two dimensional materials such as hexagonal boron nitride [42, 29, 24]. Hexagonal boron nitride (h-BN) has a honeycomb atomic structure in which boron (B) and nitrogen (N) atoms occupy alternating sites. Despite similar morphology with graphene, the binary atomic structure of hexagonal boron nitride leads to mixed ionic-covalent atomic bonding. Such atomic bonding which is different from the covalent sp2 bonding of graphene gives h-BN distinct physical and mechanical properties than graphene. Opposed to graphene which displays a zero bandgap and is semimetallic [108], h-BN shows a band gap and is an insulator with a wide band gap of 5.6 eV [74]. Such differences in the physical properties of h-BN and graphene, has motivated the synthesize of hybrid grapheneboron nitride sheets with properties which are complementary to both graphene and boron nitride [24, 90].

Besides being complementary to graphene, the remarkable physical and mechanical properties h-BN such as low dielectric constant [20], high temperature stability [37], high thermal conductivity [126] and high strength [109, 49] make it appealing for a wide spectrum of applications in its own right. The wide spectrum of applications

of h-BN expose it to different thermal, electrical and vibrational loadings. For a reliable usage of h-BN in such sensitive devices it is essential to ensure that h-BN can sustain such loadings. This necessitates a fundamental understanding regarding the mechanical and fracture properties of h-BN.

Opposed to graphene whose mechanical and fracture has been studied in the past [156, 162, 114], the studies on the fracture properties of graphene-like two-dimensional materials is scarce. Considering that graphene-like two-dimensional materials such as h-BN have a more complex atomic structure than graphene, their fracture properties can be quite different from graphene. Such differences necessitate a separate study of the fracture of h-BN. Ideally, the fracture and mechanical properties of h-BN should be characterized experimentally, e.g., by uniaxial test. However, designing and conducting test at nanoscales is very complicated; to date no uniaxial test on two-dimensional materials has been reported. Computational studies such as molecular dynamics, on the other hand, can provide valuable insights regarding the behavior of twodimensional materials. In this dissertation, the molecular dynamics simulations with a Tersoff potential [140] is used to study the fracture properties of single layer boron nitride sheets under mixed mode I and II loading.

3.2 Tersoff potential

The molecular dynamics simulations are conducted using the LAMMPS package [76]. The interatomic interaction between the boron and nitrogen atoms in the BN sheets are prescribed using the Tersoff potential [140]. The Tersoff potential can be

written as

$$V_{ij} = f_C(r_{ij})[f_R(r_{ij}) + b_{ij} f_A(r_{ij})], \tag{4}$$

where f_C is a cut-off function defined as

$$f_C(r) = \begin{cases} 1 & r \leq= R - D \\ 0.5 - 0.5\sin(\frac{\pi}{2}\frac{r-R}{D}) & R - D < r < R + D \\ 0 & r \geq R + D \end{cases}, \tag{5}$$

The function f_r is a two body term and represents a repulsive pair potential whereas f_A is a three body term and represents the attractive pair potential due to the atomic bonds. The function $f_R(r_{ij})$ and $f_A(r_{ij})$ are given by

$$f_R(r_{ij}) = A \cdot \exp(\lambda_1 r_{ij}), \tag{6}$$

and

$$f_A(r_{ij}) = -B \cdot \exp(\lambda_2 r_{ij}). \tag{7}$$

Function b_{ij} represents a measure of the bond order which depends on the local coordination of the neighbors of atoms i and the angle θ_{ijk} between atoms i, j and k. Function b_{ij} is defined by

$$b_{ij} = (1 + \beta^n \zeta_{ij}^n)^{-\frac{1}{2n}} \tag{8a}$$

$$\zeta_{ij} = \sum_{k \neq i,j} f_C(r_{ij}) \cdot g(\theta_{ijk}) \cdot \exp(\lambda_3^3 (r_{ij} - r_{ik})^3) \tag{8b}$$

$$g(\theta) = 1 + \frac{c^2}{d^2} - \frac{c^2}{d^2 + (\cos\theta - h)^2} \tag{8c}$$

In the above equations, the summation is taken over all the neighbors j and k of

atoms i which are located within a cutoff distance of $R + D$.

Several sets of Tersoff potential parameters for interaction between B an N atoms have been developed in the past [126, 125, 142, 69]. Sekkal et al. [125] modified the Tersoff set of parameters of carbon [140] to describe the B and N interactions in cubic boron nitride (c-BN) systems. Verma et al. [142] modified this set of parameters to describe the interactions of B and N in hexagonal BN (h-BN) systems. More recently, adjusted set of Tersoff potential parameters for boron nitride are developed by fitting the obtained interatomic forces, bond lengths, cohesive energy and phonon dispersion curves to the experimental and *ab initio* modeling data [126, 69, 86]. Furthermore, Tersoff potential parameters have been extended to describe the interaction among carbon, boron and nitrogen [69, 102]. Such parameters are used to study the thermal transport and mechanical properties of more complex materials such as hybrid graphene-boron nitride [69] or graphitic carbon nitride [102].

In this dissertation, the potential parameters and their corresponding values for BN are provided by [69]. This potential parameter set has been successfully used in accurate reproduction of structural, mechanical, vibrational and thermal transport properties of hexagonal boron nitride nanostructures [126] and hybrid graphene-boron nitrid nanoribbons [69].

3.3 Numerical examples

Our molecular dynamics model is a circular domain cut around the crack tip as shown in figure 15. The circular domain is chose large enough that its boundary falls in the K-dominant zone. The initial zigzag and armchair cracks are generated

by eliminating respectively three and four rows of atoms. We investigate the effect of crack edge chirality on the fracture properties by considering both armchair and zigzag cracks. As are shown in figure 16(a), the edges of zigzag cracks are not alike. In one of the edges, boron atoms occupy the outermost layer while in the other edge, nitrogen atoms are located at the outermost layer. Since when loading phase angle is not zero, the deformation of the top and bottom edges of the crack is not symmetric. For example, under pure mode II loading, one edge is under the compression and the other edge is under tension. To take into account the crack edge unsymmetry, the loading phase angle is varied from -90° to 90°. This allows us to consider the effect of tension or compression in either of the edges on the critical stress intensity factor, K_{cr}.

The edges of cracks with armchair chirality are symmetric. However, the armchair cracks can have different tip configurations. The impact of tip configuration on the critical stress intensity factors and crack propagation paths are studied by considering the four different crack tips shown in figure 16. Depending on the location of the crack, a B or a N can occupy the crack tip. Furthermore, the crack tip can have a blunt shape or can have a sharp configuration. We refer to blunt and sharp cracks with a boron atom at the tip as AC-BB and AC-BS and to the blunt and sharp cracks with a N atom at the tip as AC-NB and AC-NS, respectively.

The equilibrim configuration of the cracked domain is obtained by first applying the crack tip asymptotic field to all the atoms in the domain and then while the boundary atoms are kept fixed the position of the interior atoms are relaxed. The crack tip asymptotic displacement fields for a linear isotropic material under combined

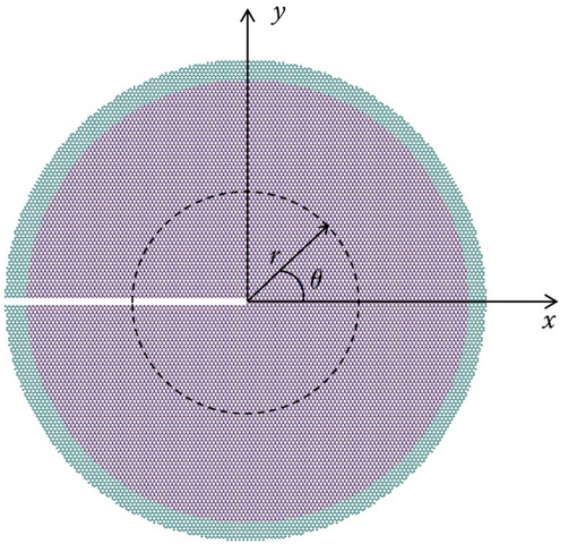

Figure 15: Molecular dynamic domain. The boundary atoms are shown in cyan.

mode I and II loading are shown in equation 3a in chapter 1.

Our goal is to model the crack propagation under quasi-static loading. For this purpose, the loading is increased in increments of $\Delta K_{\text{eff}} = 0.01$ MPa$\sqrt{\text{m}}$. After each loading increment, the position of boundary atoms are kept fixed while the position of interior atoms are relaxed using the conjugate gradient method. The temperature of interior domain is then increased to 300 K, using the velocity-rescaled Berendsen thermostat. After relaxing for 3 ps using a microcanonical (NVE) ensemble, a Nosé-Hoover thermostat is used to maintain the temperature at 300 K for 60 ps in a canonical (NVT) ensemble. The velocity-Verlet algorithm with a time step of 1 fs is used for the purpose of time integration of atoms trajectory.

The material coefficients for single layer h-BN are shown in table 3. These values are obtained based on the DFT simulations [109].

Table 3: Material coefficients of single layer h-BN for generating the displacement field on the boundary.

Young's modulus	925 GPa
Poisson's ratio	0.23

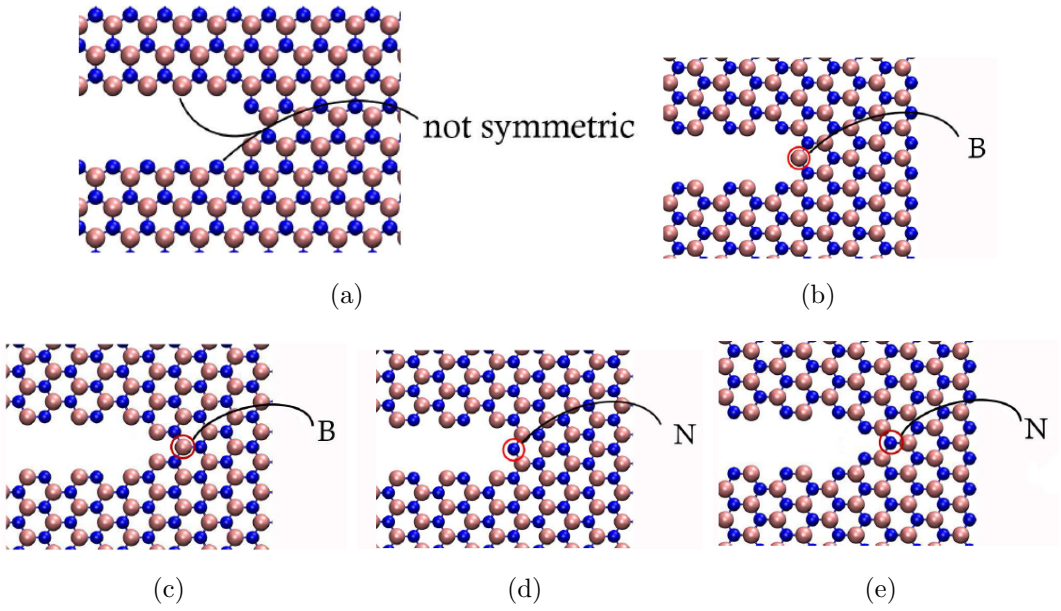

Figure 16: Five crack types: (a) zigzag crack, (b) a blunt armchair crack with a B atom at the crack tip, (c) a sharp armchair crack with a B atom at the crack tip, (d) a blunt armchair crack with a N atom at the crack tip, (e) a sharp armchair crack with a N atom at the crack tip.

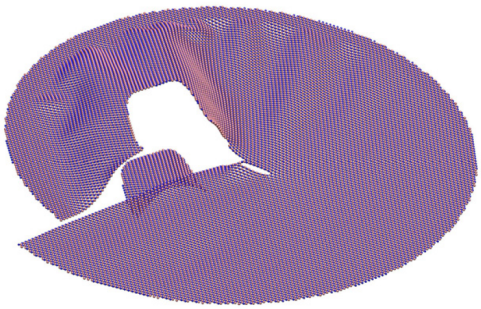

Figure 17: A buckling crack under pure mode II loading in h-BN sheet.

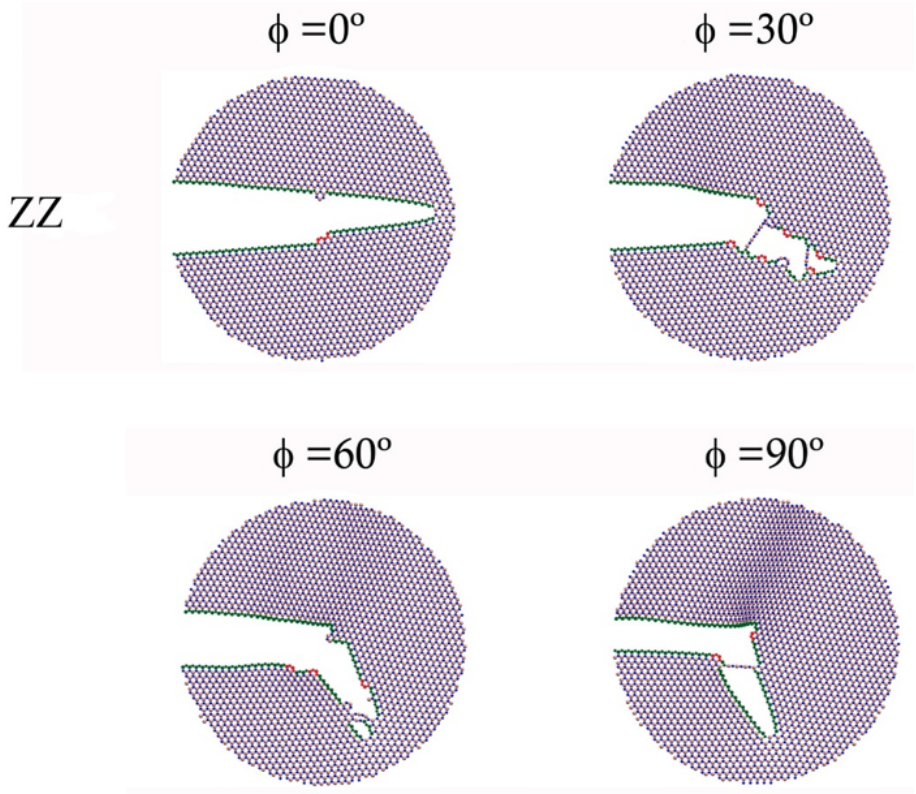

Figure 18: Crack propagation paths in a BN sheet, zigzag crack.

3.4 Results

The crack propagation path of the zigzag and armchair cracks are shown in figure 17. These figures show that loading phase angle, crack edge chirality and crack tip configuration affect the cracks growing path. An important observation is that regardless of the loading phase angle or crack geometry, cracks tend to advance along a zigzag path, which is similar to the observation in chapter 2 for MoS_2 and previous studies of graphene sheets ([155, 162]). The propagation paths show in figure 18 $\sim$ 22, indicate that as the cracks grow, they can kink. In that case the crack path might include segments of armchair direction. To clearly separate the armchair and zigzag segments of the propagation paths, the zigzag crack surfaces are shown in green and

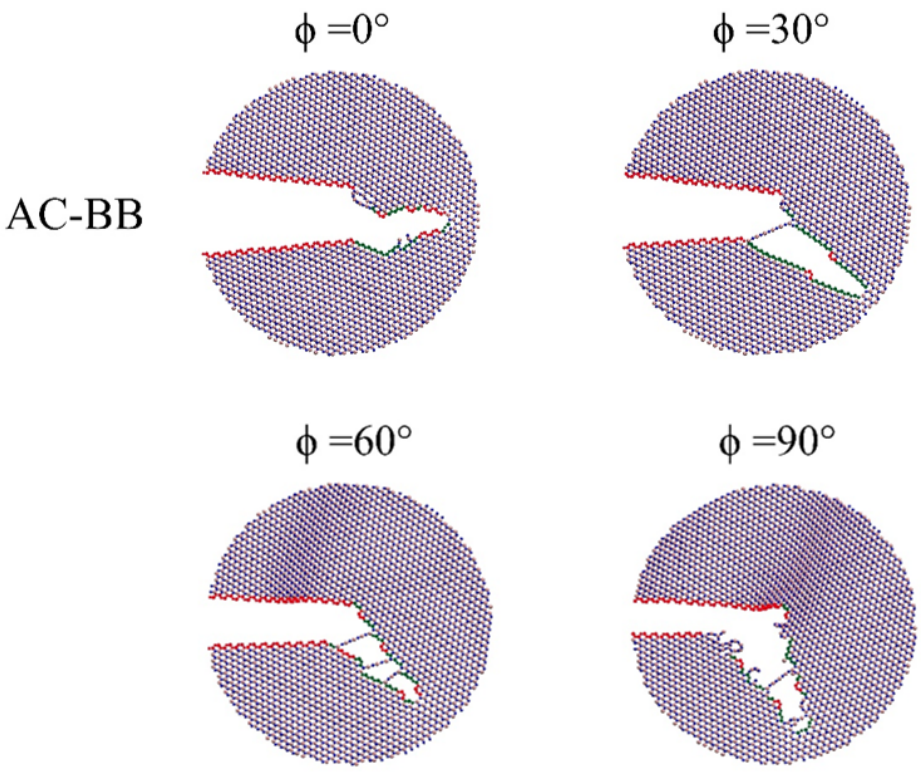

Figure 19: Crack propagation paths in a BN sheet, A blunt armchair crack with a B atom at the crack tip.

armchair atoms are shown in red. These figures show that the length of armchair segments are much smaller than the zigzag segments of the crack path.

The only condition in which the crack propagates along a self-similar path is a zigzag crack under the pure mode I loading (loading phase angle equals to zero). Armchair cracks kink even under mode I loading to propagate in a zigzag direction. Besides crack edge chirality and loading phase angle, crack tip configuration also impacts the propagation path.

Out-of-plane deformation occurs in the boron nitride sheet when the loading phase angle is not zero. The out of plane deformation is due to the buckling of BN sheet under compressive loading; since BN sheet is very thin, compressive stress can generate local buckling in the sheet. The out-of-plane deformation releases some energy

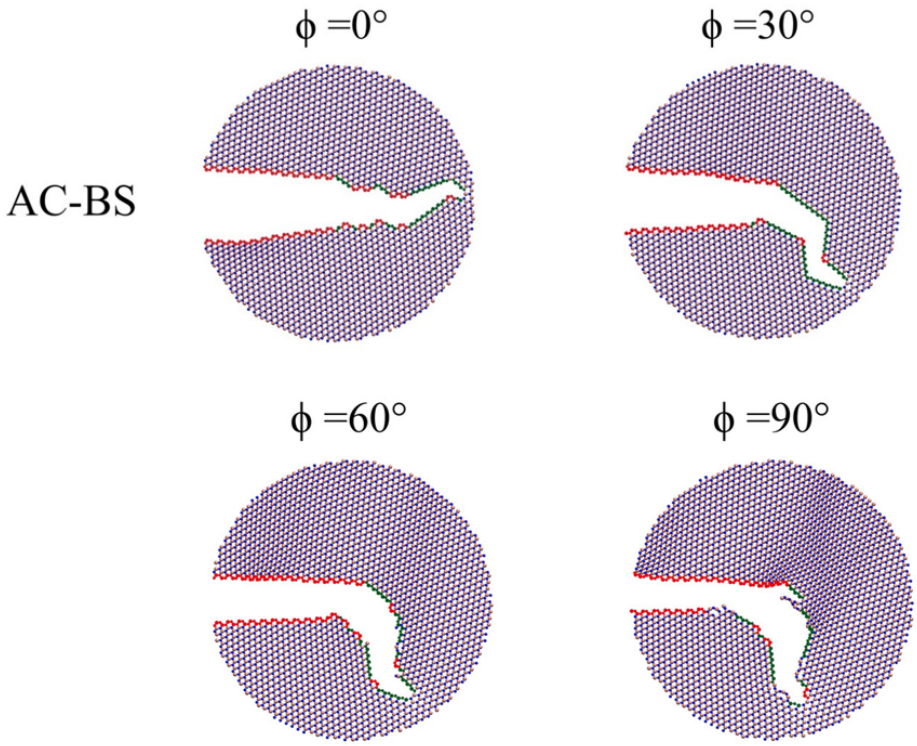

Figure 20: Crack propagation paths in a BN sheet. A sharp armchair crack with a B atom at the crack tip.

through bending and can postpone the crack's propagation. Such a phenomenon has been observed previously in the thin plates under the tensile or shear loading [95, 128, 18, 19] as shown in chapter 2 [148]. The maximum out-of-plane deformation as a function of the loading phase angle is shown in figure 23. The plots of this figure indicate that the out-of-plane deformation is negligible when the loading phase angle is close to zero and increases as the loading phase angle approaches 90°, i.e. out-of-plane deformation is considerable when mode II loading is dominant.

Excessive out-of-plane deformation can induce buckling cracks (BC) in the sheet. Since increase in the loading phase angle leads to increase in the out-of-plane deformation, it is expected that buckling cracks initiate when the loading phase angles are close to 90°. A buckling crack is shown in figure 17. As shown, buckling cracks

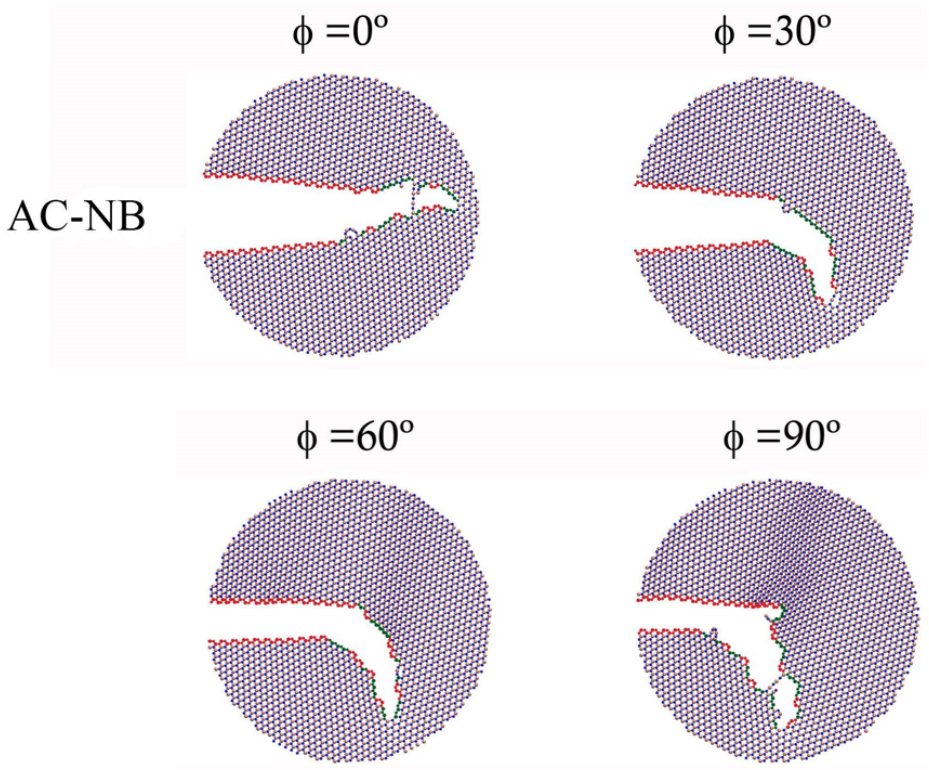

Figure 21: Crack propagation paths in a BN sheet. A blunt armchair crack with a N atom at the crack tip.

start at the crack edge in a direction orthogonal to the initial crack. The buckling crack ends at the tip of the original crack. Hence, due to the buckling crack, a segment of the boron nitride sheet is separated from the rest of the sheet.

The effective critical stress intensity factor ($K_{\text{cr}}^{\text{eff}}$) associated with the propagation of the original crack (CP) and nucleation of buckling cracks (BC) are shown in figures 24, 25 and 26 for zigzag and armchair cracks. The plots of figure 24 show that the mode I critical stress intensity factor for a zigzag crack is about 5.56 MPa$\sqrt{\text{m}}$. This can be used to find the surface energy of a armchair crack by using the Griffith relation for brittle materials which relates the critical stress intensity factor to the surface energy density γ, by

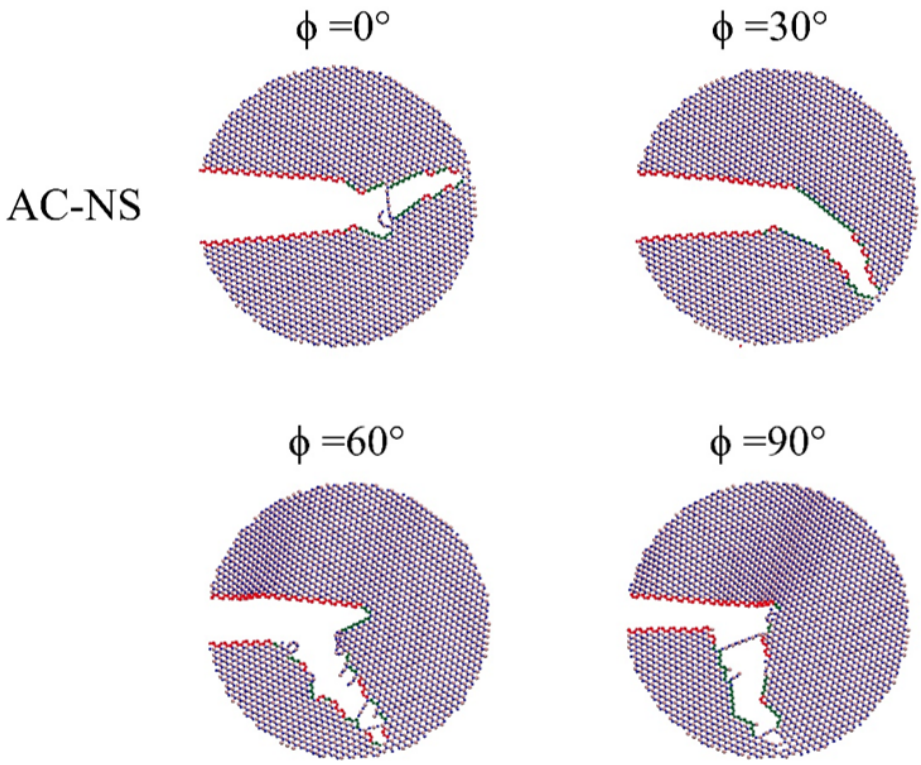

Figure 22: Crack propagation paths in a BN sheet. A sharp armchair crack with a N atom at the crack tip.

$$K_{\mathrm{cr}} = \sqrt{2\gamma E} \tag{9}$$

Using equation 9, the armchair surface energy density is 18.06 J/m^2 which is bout 50 % higher than the zigzag surface energy of 12 J/m^2 for graphene [50]. The critical stress intensity factors are larger when the loading phase angle is less than zero, i.e. the edge with nitrogen atoms at its outermost layer are in compression. The pure mode II (ϕ = 90° or -90°) critical stress intensity factor for a zigzag crack is about 6.60 MPa$\sqrt{\mathrm{m}}$. This indicates that crack propagation under shearing mode demands more energy compared to the energy required for crack propagation under opening load. This is partly due to the out-of-plane deformation generated when mode II is

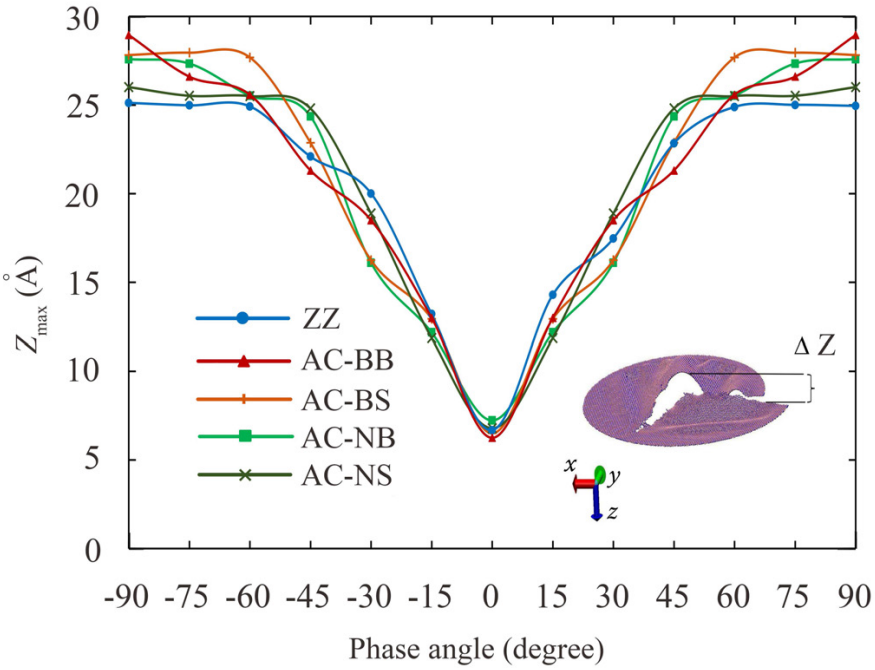

Figure 23: Maximum out-of-plane deformation of cracked boron nitride sheet as a function of loading phase angle.

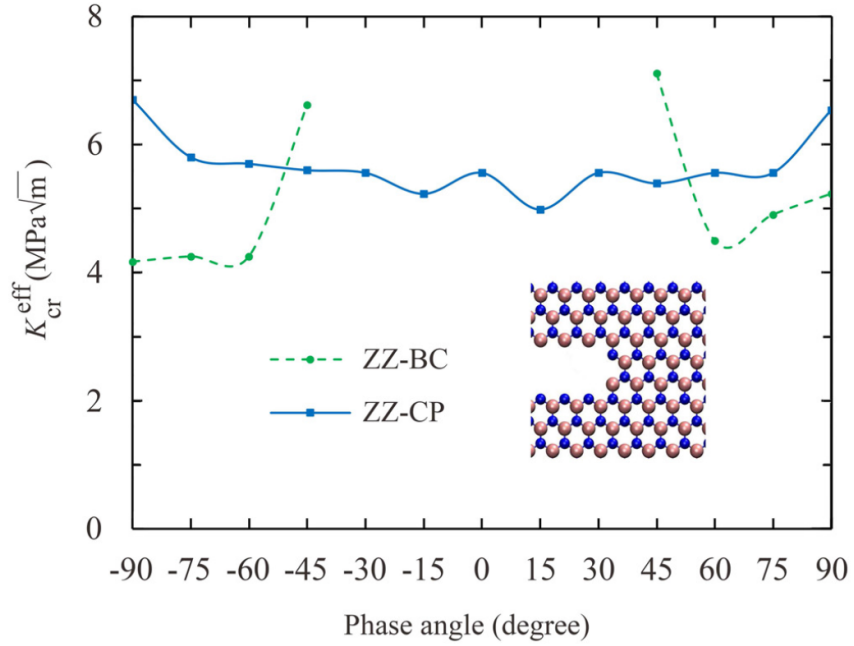

Figure 24: Critical stress intensity as a function of loading phase angle for a zigzag crack.

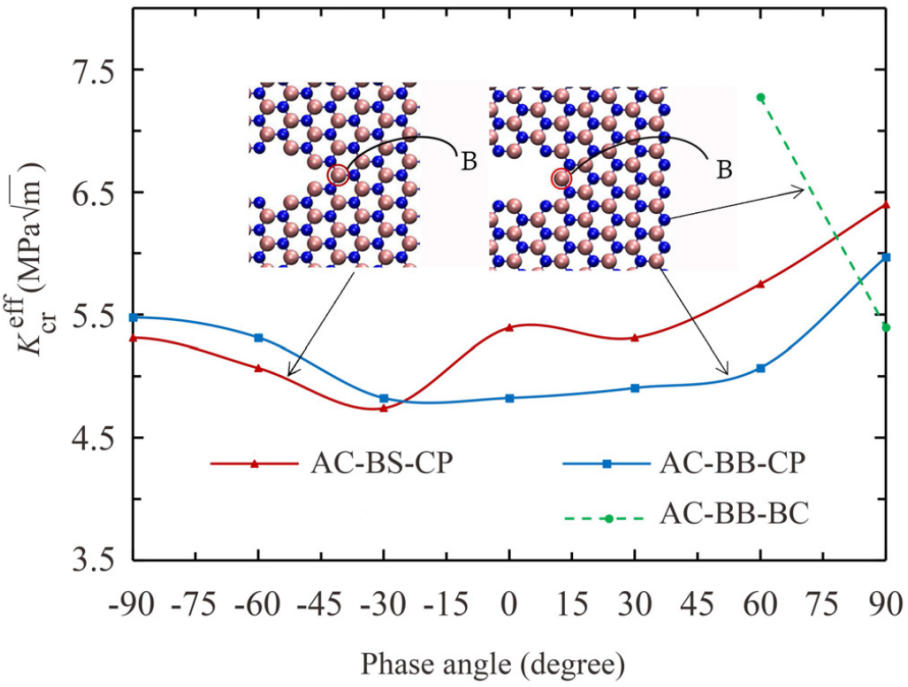

Figure 25: Critical stress intensity as a function of loading phase angle for an armchair crack with a boron atom at its tip.

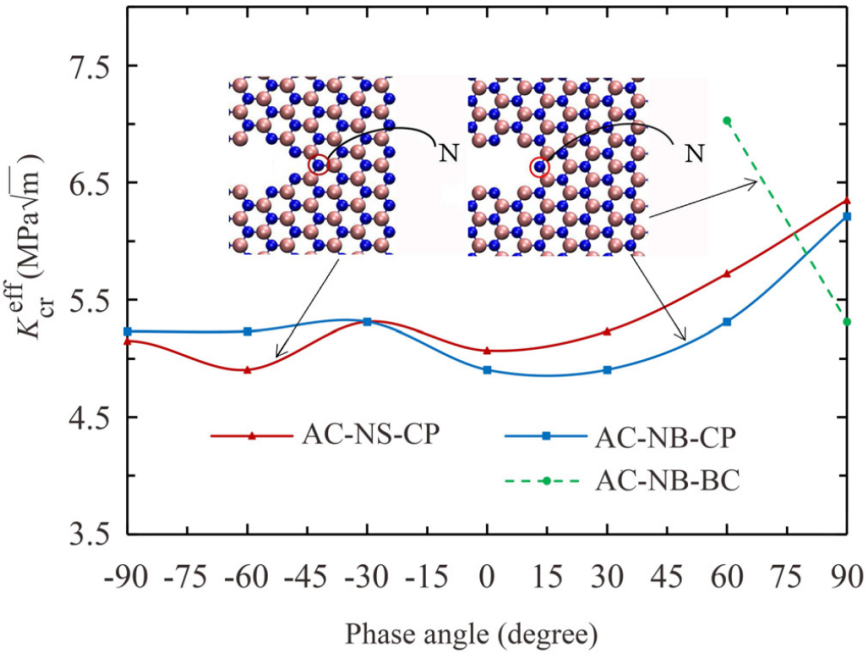

Figure 26: Critical stress intensity as a function of loading phase angle for an armchair crack with a nitrogen atom at its tip.

dominant. Some of the energy of the applied loading is used by the elastic energy of buckling bending, hence more external energy should be applied to the system before a bond at the crack tip breaks.

The dashed curve in figure 24 corresponds to the stress intensity factor at which a buckling crack nucleates. These curves show that when loading phase angle is less than 45°, no buckling crack is generated. This is in consistency with the out-of-plane deformation curves shown in figure 26, i.e. the amount of out-of-plane deformation is negligible when the loading phase angle is less than 45°. Moreover, buckling cracks nucleate before the propagation of the original crack when loading phase angle is larger than 52°.

The effective critical stress intensity factors for armchair cracks with boron and nitrogen atoms at their tips are shown in figure 25 and figure 26; respectively. Comparing the plots of these figures with the plots of figure 24 show, that in general the critical stress intensity factors of zigzag cracks is higher than those of armchair cracks. The plots of these figures indicate that crack tip configuration can affect the critical stress intensity factor. Mode I stress intensity factor is almost the same for sharp and blunt configurations. The mode I critical stress intensity factor of an armchair crack is 5.35 MPa$\sqrt{\text{m}}$ and 5.15 MPa$\sqrt{\text{m}}$ for tips with a boron and nitrogen atom at their tips; respectively. The mode II critical stresss intensity factor is higher than of mode I and depending of the tip configuration varies from 6.2 MPa$\sqrt{\text{m}}$ to 7.2 MPa$\sqrt{\text{m}}$. For both cases of cracks with a boron or nitrogen atom at the tip, when the loading phase angle is less than 30°, the critical stress intensity factor of cracks with a blunt tip is larger than $K_{\text{cr}}^{\text{eff}}$ of cracks with a sharp tip and when the loading phase angle is larger

than 30° cracks with a sharp tip configuration have a higher critical stress intensity factor.

The crack tip configuration also impacts the formation of buckling cracks. Buckling cracks are not generated for armchair cracks with a sharp crack tip. Buckling cracks initiate only if the crack tip is blunt and the loading phase angle is larger than 75°. Therefore; the formation of buckling cracks is a more sever issue for sheets with in initial zigzag cracks in them.

3.5 Conclusion

The simulations show that the crack edge chirality, crack tip configuration and loading phase angle affect the critical stress intensity factor and crack propagation path of the boron nitride sheet. The initial cracks prefer to propagate in a direction, which can form a new zigzag crack surface. Besides the propagation of main crack, excessive out-of-plane deformation of BN sheet under mixed mode loading can lead to the formation of buckling cracks.

CHAPTER 4: MOLECULAR DYNAMICS STUDY OF THE THERMAL CONDUCTIVITY OF MOS_2

4.1 Introduction

Monolayer molybdenum disulfide (MoS_2) is a graphenelike two dimensional material. Monolayer MoS_2 displays remarkable features such as excellent electrostatic coupling [113], tunable bandgap [94], gate tunable superconductivity [159], and high mechanical strength [23, 148, 5] properties which bring it a wide spectrum of applications in polymer composites [163, 87], nanoelectronics [145], and optoelectronic10 devices. Monolayer MoS_2 posses a large value of Seebeck factor in the range of -4×10^2 to -$1\times10^5 \mu V/K$ [39, 22]. Such a high Seebeck coefficient makes monolayer MoS_2 desirable for thermoelectric applications such as on-chip thermopower generation and waste thermal energy harvesting. The ability of thermoelectric materials to produce thermoelectric power is inversely related to their thermal conductivity [43]. To improve the performance of MoS_2 based thermoelectric devices, it is necessary to develop techniques for tuning the thermal conductivity of MoS2 ribbons. This necessitates a fundamental understanding of the mechanism of thermal conductivity of MoS_2 ribbons.

The strain engineering of two and three dimensional materials has been studied in the past [111, 14, 117, 82, 134, 52] and the reported results show that the impact of tensile strain on the thermal conductivity of two and three dimensional materials

is not the same. While the application of normal tensile strain to three dimensional materials reduces their thermal conductivity, [111, 14, 117, 82] tensile strain increases the thermal conductivity of two-dimensional materials such as monolayer hexagonal boron nitride [134] or silicene [52]. The differences in the response of two-dimensional materials to strain necessitate a separate investigation of the strain effects on the thermal conductivity of monolayer MoS_2.

Due to the difficulties of conducting experiments at nanoscale, computational methods such as molecular dynamics (MD) and density functional theory have attracted intense attentions to study the behavior of two dimensional materials [133, 60, 38, 73, 59, 135]. In this dissertation, we use reverse nonequilibrium molecular dynamics method (RNEMD) to investigate the thermal conductivity of monolayer MoS_2 layers. We study how the geometry of ribbons including length and chirality affect the thermal conductivity of nanoribbons. Moreover, we investigate the impact of longitudinal uniaxial strain on the thermal conductivity of MoS_2 ribbons.

4.2 Stillinger-Weber interatomic potential

In this chapter, the molecular dynamics study using a Stillinger-Weber (SW) interatomic potential is conducted. Modified SW potential for single layer MoS_2 is used to model the interaction between atoms in single layer MoS_2 sheets [58]. SW potential considers two types of interactions between atoms: bond-stretching and angle-bending. The potential energy due to bond stretching and angle bending is,

$$V_{\text{bond}} = A \cdot \exp\left(\frac{\rho}{(r - r_{\max})}\right) \cdot \left(\frac{B}{r^4 - 1}\right) \tag{10a}$$

$$V_{\text{angle}} = K \cdot \exp\left(\frac{\rho_1}{r_{12} - r_{\text{max12}}} + \frac{\rho_2}{r_{13} - r_{\text{max13}}}\right) \cdot (\cos\theta - \cos\theta_0)^2, \tag{10b}$$

where V_{bond} and V_{angle} are the potential of bond-stretching and angle-bending; r is the bond length. r_{max}, r_{max12} and r_{max13} are cutoff distances beyond which the interaction disappears. A, B, K, ρ_1 and ρ_2 are five parameters, which are determined by considering both the phonon spectrum and stress-strain relation of single layer MoS_2. Thus, this potential can represent both thermal and mechanical properties of single layer MoS_2 nanoribbon with high precision, especially when the nano ribbon is under large strain and the material undergoes nonlinear deformation.

Before evaluating the thermal conductivity of nanoribbons, the thermal equilibrium is established in the system by conducting a 250 picosecond Nosé-Hoover thermal bath coupling at a temperature of 300 K. Atoms trajectories are obtained by integrating the equations of motion using a velocity-Verlet scheme at a fixed time step of 0.5 fs. The ribbon is periodic along its longitudinal axis and the spurious rotation of nanoribbons is prevented by fixing the first row of atoms at the top and bottom of the ribbons.

4.3 Nonequilibrim molecular dynamics method and Müller-Plathe's algorithm

The Müller−Plathe's algorithm is developed in 1997 [105]. It is a nonequilibrim molecular dynamics method to calculate the thermal conductivity of materials. The main idea is to generate a heat flux on the system and measure the resulting temperature gradient (see figure 27). Here are the steps of applying the Müller-Plathe's algorithm in this study:

1. In the longitudinal direction, periodic boundary is applied. It means that the

atoms on the left end can interact with the atoms on the right end of the boundary, and they can move across the left and right boundaries of the simulation box. The Top and bottom atoms are fixed to prevent the spurious rotation of the nanoribbons. The nanoribbon's energy is minimized at zero temperature. Then the temperature is increased to 300 K by generating random velocities of the atoms. The Nosé-Hoover thermostat is used to maintain the temperature of the ribbon at 300 K.

2. The nanoribbon is divided into 50 slabs in the longitudinal direction. As shown in figure 27(a), the center slab is the "hot" slab, and the slabs on the edge are the "cold slabs". During the simulation, in every 25 fs, the kinetic energy of the coldest atom in the hot slab and the kinetic energy of the hottest atom in the cold slab are exchanged. This procedure runs 750 ps to make sure the temperature profile and heat flux are stabled through the whole ribbon. An example of a stabilized temperature profile is shown in figure 27(b).

3. After the temperature profile is equilibrated, during the last 500 ps, the heat flux and the temperature profile are recorded each 50 ps for 10 times. These data is to be used to calculate the thermal conductivity. The 10 values of thermal conductivity are averaged as the thermal conductivity for the current example.

The thermal conductivity is calculated using:

$$\kappa = \frac{J}{2A\frac{\partial T}{\partial x}} \tag{11}$$

where A is the cross area through which the heat flux flows and T is the temperature profile throughout the x direction. Here the thickness of the nanoribbons is taken as the distance between the two atomic layers in bulk MoS_2. J is the heat flux between

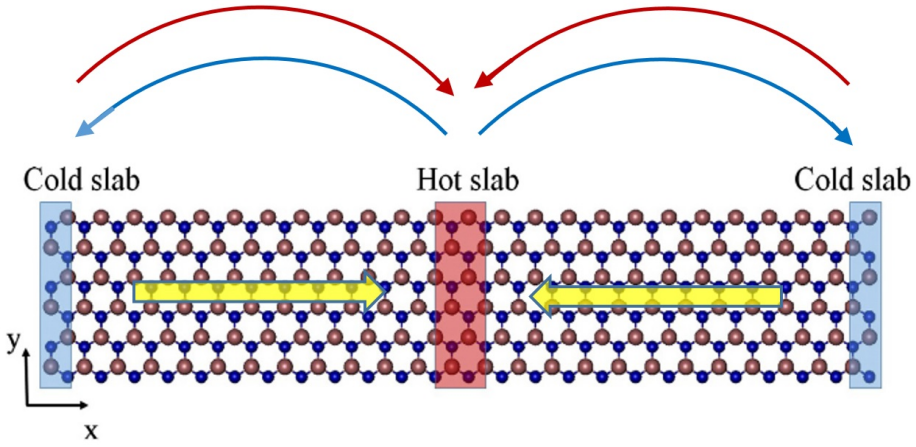

(a)

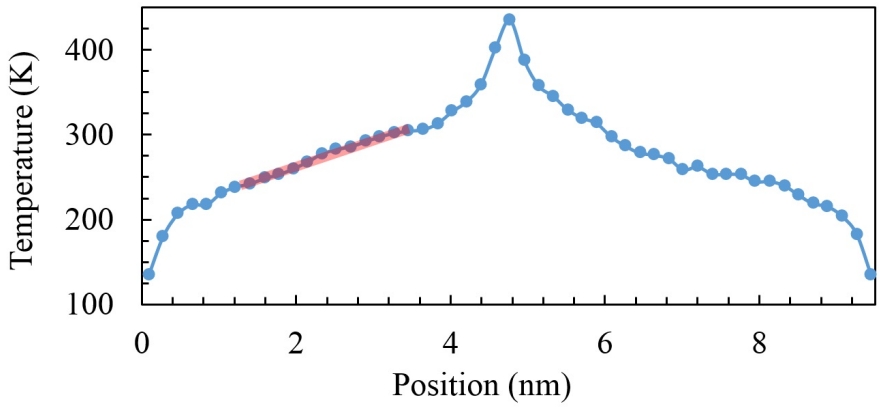

(b)

Figure 27: The simulation box of reversed nonequilibrim molecular dynamics method follows the Müller-Plathe's algorithm. The hot slab (shown in red) is placed at the middle of the ribbon, whereas the cold slabs (shown in blue) are located at the edges of the ribbons. The bottom figure shows a typical example of the temperature profile along the ribbon axis. The linear part shown in red is used to find the temperature gradient with respect of the x coordinate.

the first and middle slabs as shown in equation 12:

$$J = \frac{1}{t} \sum_{N_{\text{transfer}}} \frac{1}{2}(m v_{\text{hot}}^2 - m v_{\text{cold}}^2) \tag{12}$$

where N_{transfer} is the total number of moment exchanges occurred during the simulation time t. m is the mass of the atoms, v_{hot} and v_{cold} are the velocities of the hottest atom of the cold slab and the coldest atom of the hot slab, respectively.

4.4 Results and discussion

4.4.1 Impact of nanoribbon's length on thermal conductivity

The simulations are conducted on both armchair and zigzag nanoribbons. The nanoribbon is in the x–y plane with the ribbon axis being in the x direction. We first study the impact of ribbons length on their thermal conductivity. Thermal conductivity of armchair and zigzag ribbons of lengths between 9Å to 2700Å and a width of approximately 22Å is plotted in figure 28. As expected, by increasing the length of ribbons their thermal conductivity increases. The increase in thermal conductivity by increase in the length is attributed to the excitation of phonons with lower frequency (long wave length) phonon modes in larger ribbons. Since low frequency phonons play the dominant role in the thermal transfer process, excitation of more low frequency waves (which can not exist in short ribbons) will facilitate the thermal transfer process and increase the thermal conductivity of ribbons.

The thermal conductivity of ribbons of finite length is related to the thermal conductivity of infinitely long ribbons through [124],

$$\frac{1}{\kappa} = \frac{1}{\kappa_\infty} \left(\frac{l}{L} + 1 \right), \tag{13}$$

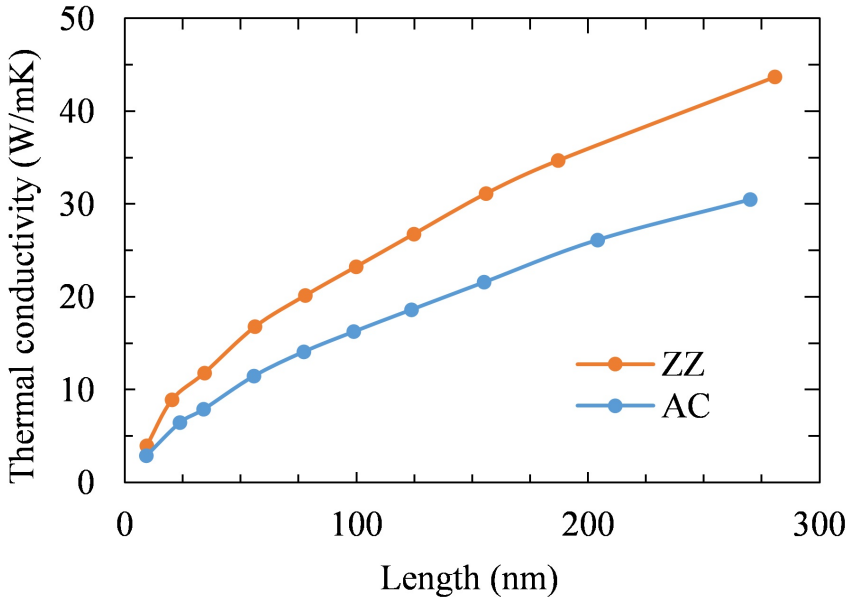

Figure 28: Thermal conductivity of ribbons versus their length.

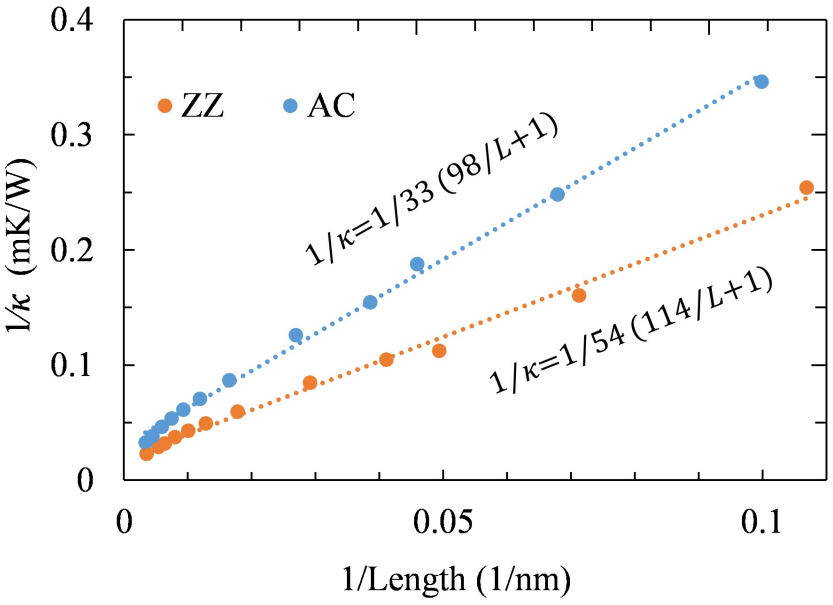

Figure 29: Inverse of thermal conductivity versus inverse of length.

Table 4: Thermal conductivity of infinity long MoS_2 ribbon from different studies.

current study	33∼54 W/mK
[123]	52 W/mK
[137]	62.2 W/mK
[158]	30.5∼38.5 W/mK

where κ is the thermal conductivity of a ribbon of length L, κ_∞ is the thermal conductivity of infinitely long ribbons and l is the phonon mean free path in the ribbons. Based on this equation the inverse of thermal conductivity of ribbons is linearly related to the inverse of their lengths. The inverse of thermal conductivity is plotted versus the inverse of the length of ribbons in figure 28. By comparing the equation of the fitted lines in figure 28 with figure 29, the thermal conductivity and phonon mean free path of infinitely long armchair ribbons are respectively 33 W/mK and 98 nm; whereas the corresponding values for the infinitely long zigzag ribbons are 54 W/mK and 114 nm. These are in close agreement with the experimental results [123, 158, 137] (see table 4). The curves in figure 28 indicates that zigzag ribbons have a higher thermal conductivity of armchair ribbons. This is in agreement with the reported results on the thermal conductivity of other grahene-like two-dimensional materials such as graphene [157] or hexagonal boron nitride [134, 4]. The difference in the thermal conductivity of armchair and zigzag ribbons can be attributed to different phonon scattering effects induced by armchair and zigzag edges.

4.4.2 Impact of nanoribbon's width on thermal conductivity

Next we investigate the influence of the nanoribbon's width on thermal conductivity. For this purpose, nanoribbons are fixed at the length of about 240 Å and the width changes from 11 Å to 180 Å. The thermal conductivity versus width for

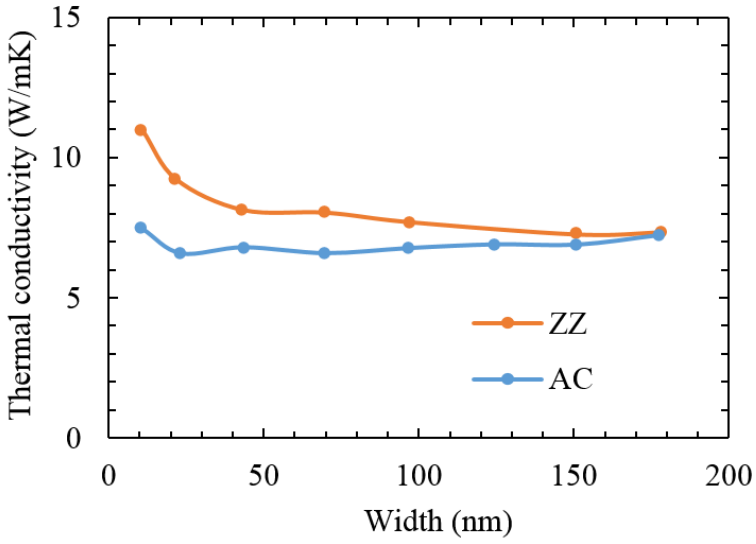

Figure 30: The thermal conductivity is stable when the strain changes from zero to the failure limit.

armchair and zigzag ribbons are shown in figure 30. The plots in this figure shows that κ is insensitive to width unless the width is smaller than 11 Å. When nanoribbons are narrower than 11 Å, κ increases slightly. It is probably because, when the width is very small, the mean free path is bigger since the number of phonons are limited, which reduces the phonon-phonon combinations and the three phonon scattering [167, 4].

4.4.3 Impact of atomic vacancy on thermal conductivity

In both mechanical exfoliation and chemical vapor deposition preparations, atomic vacancy as shown in figure 31 are generated, especially the sulfur vacancy [166, 51, 71]. Meanwhile, defect engineering provides a viable tool to tune the material behavior. To observe how the thermal conductivity varies based on different vacancy densities, we randomly delete S or Mo atoms on a 125×30 Å^2 MoS_2 nanoribbon (except the top

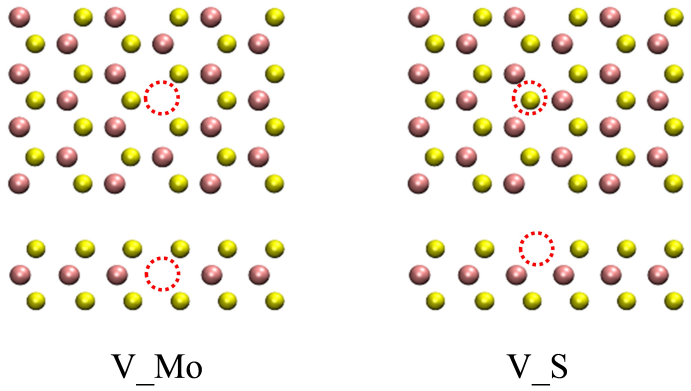

Figure 31: The thermal conductivity of MoS_2 naoribbon as a function of the nanoribbons width. It is insensitive to the change of the width, unless the width is extremely small.

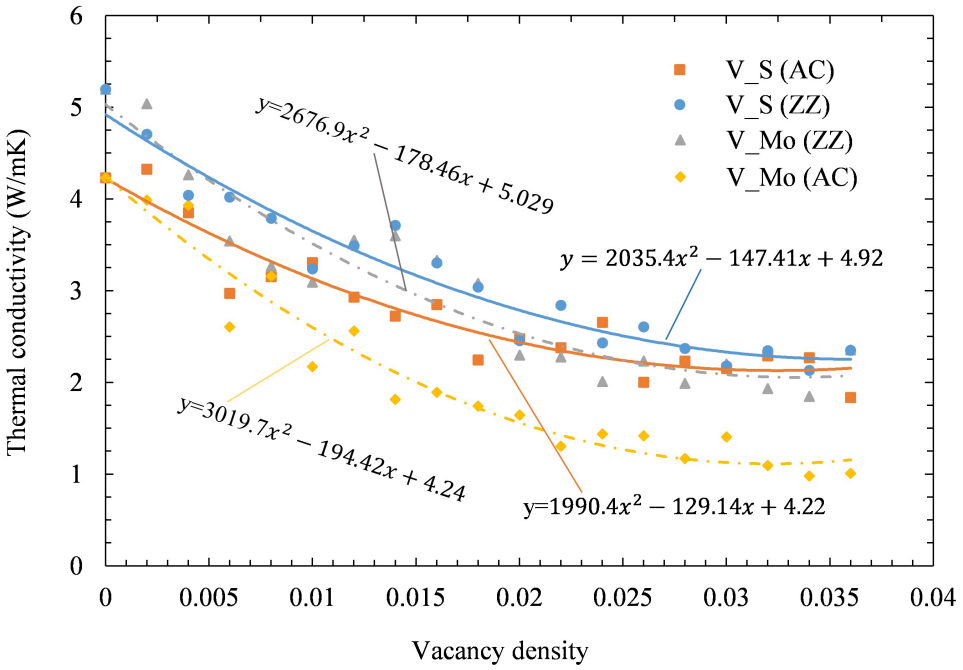

Figure 32: Thermal conductivity of armchair and zigzag MoS_2 ribbons with the atomic vacancy.

and bottom boundary atoms which are not accounted in the calculation). Figure 32 shows the trend of the thermal conductivity with the increase of the atomic vacancy density. The vacancy density is calculated by dividing the number of vacancies by total number of atoms. Each data point is the average of results of three examples. We also fitted the data into second order polynomials separately for zigzag and armchair nanoribbons.

These curves indicate that the thermal conductivity of both armchair and zigzag ribbons reduce in the presence of defects. Molybdenum vacancies have a more impact on the thermal conductivity than sulfur vacancies. Specially, the presence of molybdenum defects in armchair nanoribbons have a very deteriorating impact on the thermal conductivity.

Based on the kinetic theory, the contribution of each phonon mode to the thermal conductivity κ is $\kappa = Cvl$, where C is the heat capacity which is a function of phonon frequency ω, l is the phonon mean free path, $v = d\omega/dk$ is the phonon group velocity and k is the wave vector. The reduction in thermal conductivity can be attributed to a decrease in the phonon mean free path (PMFP) of ribbons. In the presence of defects the phonon mean free path l can be obtained from

$$\frac{1}{l} = \frac{1}{l_{\mathrm{pp}}} + \frac{1}{l_{pd}}, \tag{14}$$

where l_{pp} denotes phonon–phonon scattering length and l_{pd} is the phonon–defects scattering length. Defects can induce considerable phonon-defect scattering which reduces the phonon mean free path. The plots of figure 32 show that by increasing

defects concentration f the sensitivity of κ on f reduces, i.e, at high concentrations l is less sensitive to f which indicates a transition from propagation to diffusive in heat transfer mechanism.

4.4.4 Impact of longitudinal strain on thermal conductivity

Although the impact of strain on the thermal conductivity of three dimensional materials has been widely studied in the past [111, 116], recently, studies show that the strain effects on the thermal conductivity of two-dimensional materials is different than their counterpart 3D materials [134, 4]. This necessitate a separate investigation of the strain effects on the thermal conductivity of monolayer MoS_2.

We calculated the thermal conductivity of a 250×30 Å nanoribbon under longitudinal strains of 0∼0.08. Figure 33 shows that the thermal conductivity of MoS_2 nanoribbon does not change under strains. This trend is opposed to the impact of strain on thermal conductivity of three dimensional materials and other two-dimensional materials [83, 53, 149].

To further investigate the main cause of such trend of thermal conductivity of MoS_2 under tensile strain, we investigate how strain influences the phonon dispersion curves. The phonon dispersion curves of zigzag MoS_2 nanoribbon with 0.00, 0.03, 0.06 strain are plotted in figure 34. The phonon dispersion curves are constucted by using the method in [72], in which the dynamical matrices are constructed directly from MD analysis. This method can be called by using "fix phonon" command in LAMMPS.

The phonon dispersion curves indicate a softening of the in-plane longitudinal and

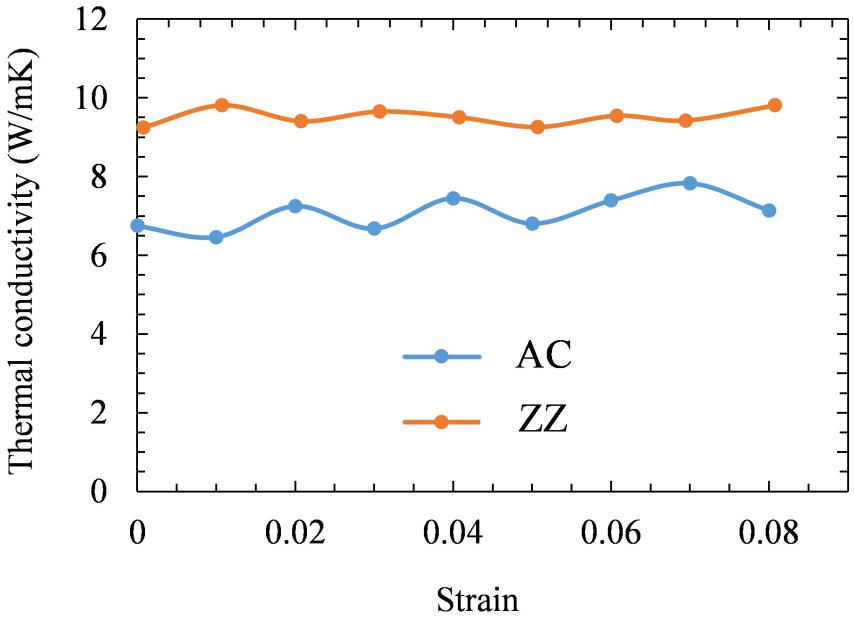

Figure 33: Thermal conductivity of armchair and zigzag ribbons as a function of longitudinal strain.

acoustic modes (LA and TA) and a slight stiffening of out-of-plane acoustic (ZA) mode. The phonon softening tends to decrease the thermal conductivity, and the phonon stiffening tends to enhance the thermal conductivity. Moreover, the group velocity of each phonon modes is shown in figure 35. It can be seen that by increasing the tensile strain, the group velocity of ZA mode increases whereas the group velocity of all the other modes reduces slightly.

Therefore, under the application of strain, the stiffening mechanism of acoustic flexural mode competes with the softening mechanism of in–plane LA and TA modes. The two mechanism counterbalance each other and the thermal conductivity of MoS_2 does not significantly change under tensile strain.

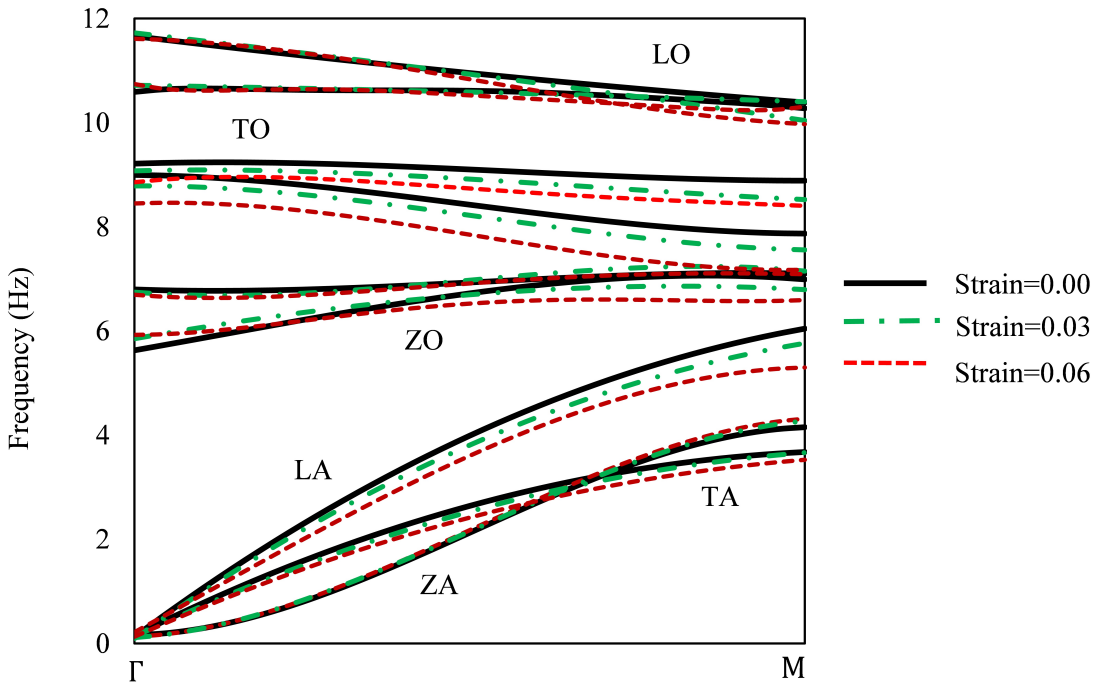

Figure 34: Phonon dispersion curves of armchair MoS_2 ribbons at three strain levels.

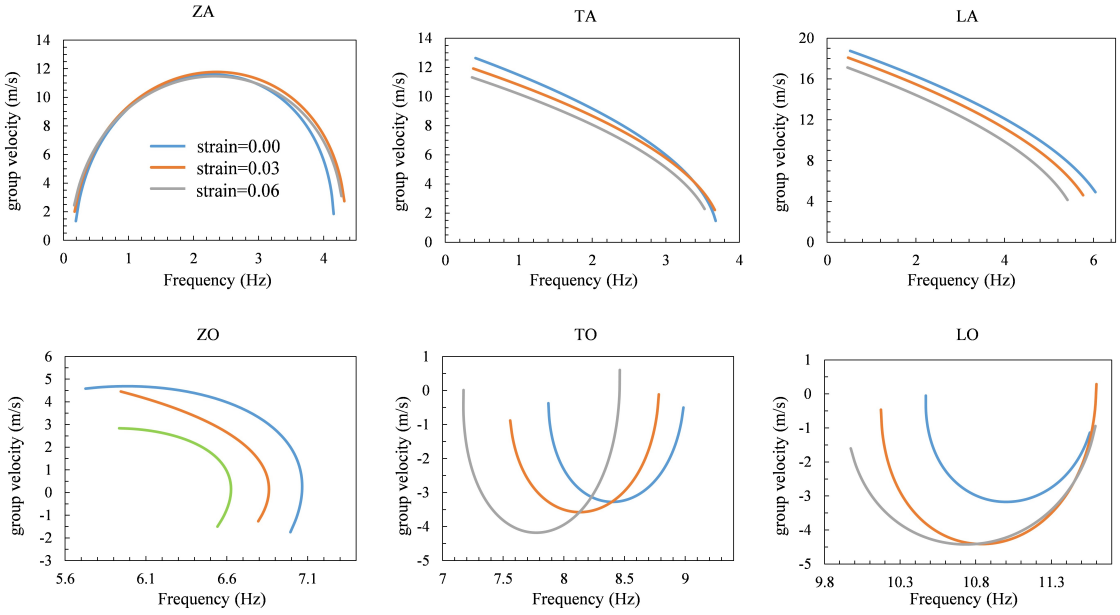

Figure 35: Group velocities of armchair MoS_2 ribbons at three strain levels.

4.5 Conclusion

The thermal conductivity for an infinity long MoS_2 nanoribbon is about 33˜54 W/mK. The zigzag nanoribbon is more thermal conductive than armchair ribbon. The thermal conductivity of MoS_2 nanoribbon is insensitive to width and strain. At 3% vacancy density, the thermal conductivity is reduced by about 50% (knowing that hexagonal BN can be reduced by 80% at 3% vacancy density).

CHAPTER 5: THE COUPLING OF MOLECULAR DYNAMICS AND FINITE ELEMENT METHODS

5.1 Introduction

Molecular dynamics simulations provide vast amount of information about material behavior at nanoscale. They have been particularly used to study how defects such as cracks, grain boundaries or dislocations affect macroscale processes such as elasticity or plasticity. However, the high computational costs associated with atomistic simulations limit their applicability to systems made of limited number of atoms. Coupled atomistic continuum methods have been introduced as a remedy to this limitation. In the coupled methods, full atomistic resolution is maintained where deformations are highly inhomogeneous (e.g., at the vicinity of defects) and continuum models are used elsewhere [136, 96, 70, 118, 119, 2, 21, 144, 12, 153, 40, 122, 84, 121, 155, 15]. The challenge lies in appropriate gluing of atomistic and continuum zones such that the atomistic region behaves as if the entire domain is atomistic. To achieve this objective, the effects of the atomistic-continuum interface should be minimized. In static problems ghost forces can be generated at the coupling interface [91] and a number of techniques have been developed to overcome this issue [12, 40]. In dynamic problems an additional difficulty related to the passage of the propagating wave from atomistic to continuum across the interface is encountered; the change of the constitutive equations from inherently nonlocal atomistic to local continuum

along with the change of the resolution from atomistic to continuum lead to spurious wave reflection at the interface. Since in the coupling methods atomistic zone usually has a small size, the spuriously reflected wave can quickly increase the temperature of atomistic zone, whereby destroys the simulation.

To avoid the spurious wave reflections, the interface between the atomistic and continuum should be such that coarse scale information (low frequency waves) can be accurately transmitted in both directions, whereas the fine scale oscillations which cannot be transmitted into the continuum zone should be eliminated at the interface. Several such interfaces have been developed in the past, among those are coarse-grained molecular dynamics (CGMD) method [118, 119], macroscopic-atomistic-ab initio dynamics (MAAD) method [2, 21], bridging scale method (BSM) [144, 143], bridging domain method (BDM) [12, 153], concurrent AtC coupling method [40, 8], embedded statistical coupling method (ESCM) [122] and heterogeneous multiscale method (HMM) [33, 34]. Reviews on concurrent atomistic-continuum multiscale methods can be found in [27, 35, 97, 98].

Belytschko et al. [12, 153] developed a bridging domain method (BDM) to couple continuum mechanics with molecular models. Bridging domain method lies in the category of overlapping domain decomposition coupling methods, or Arlequin method, which has been developed earlier by Ben Dhia [2628]. This method has been used for modeling cracks and defects in graphene and carbon nanotubes [12, 153, 165, 164] and has been combined with extended finite element method (XFEM) [101] to study crack propagation and dislocation emission in nanomaterials [44, 103]. More recently, BDM applications are extended to multiscale analysis at finite temperature [6, 120].

In the bridging domain method, continuum and atomistic domains overlap in a bridging (handshaking) domain where a weight function is used to partition the atomistic and continuum energy. In the overlapping domain, the positions of atoms and nodes are not necessarily coincident and the compatibility between atomistic and continuum domain is imposed by Lagrange multipliers. This allows to use a uniform mesh in the entire domain and removes the need for mesh refinement in the overlapping region.

In this chapter, we first numerically show that the type of the discretization of Lagrange multipliers and the time integration step size significantly impact the success of BDM method in suppressing spurious reflections. Then, we present a new technique to enhance the performance of BDM and to alleviate the effects of the two aforementioned factors. In this method, the total displacement field of atoms located in the overlapping zone is decomposed into a fine and a coarse scale displacement field. The fine scale displacements corresponds to the oscillations which cannot be resolved by the finite element mesh and need to be damped. The elimination of fine scale oscillations is accomplished by deriving their equations of motion and inserting a damping term into their equations of motion.

The outline of this chapter is as follows. In section 5.2, we review the bridging domain method. In section 5.3, we numerically study the performance of the BDM method and will provide the motivation of the proposed enhancement. The formulation of the new enhancement is presented in section 5.4. The effectiveness of the method in removing spurious reflections and in modeling crack propagations will be investigated using numerical examples in section 5.5. Some conclusions are made in

section 5.6.

5.2 Brief review of bridging domain method

5.2.1 Reference model and notations

In the bridging domain method (BDM), the domain Ω is composed of an atomistic subdomain, Ω^A, and a continuum subdomain, Ω^C, which overlap in a bridging or handshaking subdomain, $\Omega^B = \Omega^A \bigcap \Omega^C$, as shown in figure 36. The edges of the atomistic and continuum subdomains in the bridging subdomain are denoted by Γ^A and Γ^C, respectively. In this paper, the superscripts "A", "C", and "B" identify the variables associated with the atomistic, continuum, and bridging subdomains respectively. Accordingly, Ω_0^A, Ω_0^C, and Ω_0^B denote the atomistic, continuum, and bridging subdomains in the initial configuration, respectively, where the subscript 0 refers to quantities defined at $t = 0$. We denote the material coordinates by $\mathbf{X}$ or $\mathbf{X_i}$, $i = 1, ..., n_d$ in component notation, where n_d is the number of spatial dimensions, and the current coordinates by $\mathbf{x}$. We use subscripts I and J to refer to FE-nodes, and α and β to refer to atoms. The displacement of atom α is denoted by d_α (or $d_{i\alpha}$ in component form). The continuum subdomain is spatially discretized by a finite element (FE) mesh and its displacement field is approximated by

$$u_i(\mathbf{X}, t) = \sum_{J \in \mathcal{S}} N_j(\mathbf{X}) u_{iJ}(t), \tag{15}$$

where $\mathcal{S}$ is a set of finite element nodes, N_J is the FE shape function of node J and u_{iJ} is the i th displacement component of node J.

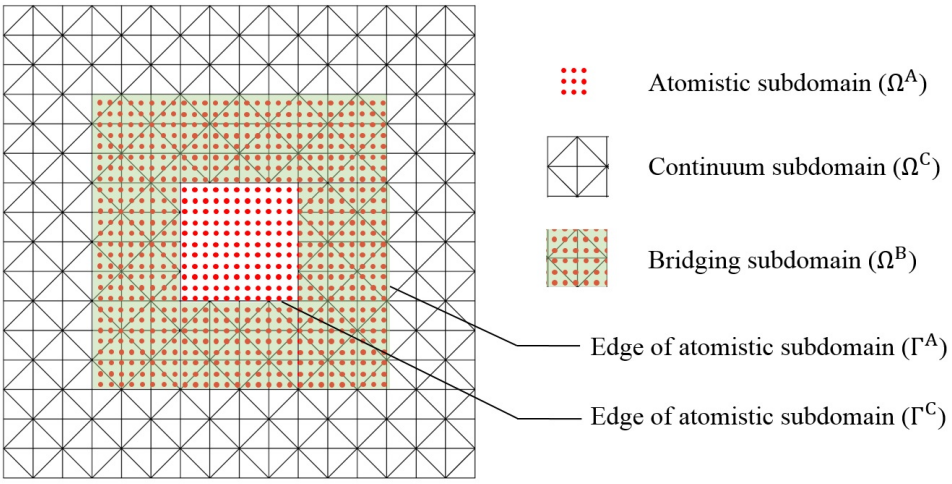

Figure 36: Three subdomains in a BDM simulation: atomistic, continuum, and bridging subdomains.

5.2.2 Governing equations

In the bridging domain method, the total Hamiltonian of the entire domain is obtained by adding up the Hamiltonian of the continuum and atomistic domains. To avoid double counting in the overlapping domain, the Hamiltonian of continuum and atomistic domains are weighted by a scaling factor $\vartheta(\mathbf{X})$ defined as

$$\vartheta = \begin{cases} 0 & \text{in } (\Omega_0^C - \Omega_0^B) \\ [0,1] & \text{in } \Omega_0^B \\ 1 & \text{in } (\Omega_0^A - \Omega_0^B) \end{cases} \tag{16}$$

In our numerical calculations, we use a linear scaling factor defined as [153]

$$\vartheta = \frac{\| X - X_p \|}{\| X_q - X_p \|} \tag{17}$$

where X_p is the orthogonal projection of X onto Γ^A and X_q is the intersection point of line X_pX and Γ^C. The total Hamiltonian of the domain is given by

$$H(\mathbf{u}, \mathbf{d}, \lambda) = H^C(\mathbf{u}) + H^A(\mathbf{d}) + G^B(\mathbf{u}, \mathbf{d}, \lambda) \tag{18}$$

where H^C is the continuum domain Hamiltonian, H^A is Hamiltonian from the atomistic domain, and G^B is the Hamiltonian associated with the Lagrange multiplier constraint that imposes displacement compatibility of the atomistic and continuum domain at the overlapping domain.

The contribution of the continuum domain in the total Hamiltonian is given by

$$H^C = \sum_{I,J \in \mathcal{S}} \int_{\Omega_0^C} (1 - \vartheta) \frac{p_{iI}^C p_{iJ}^C N_I N_J}{2\rho_0} d\Omega + \int_{\Omega_0^C} (1 - \vartheta) W^C(F) d\Omega, \tag{19}$$

where p_{iI}^C is the ith component of the linear momentum of node I, ρ_0 is the initial density of the continuum domain, W^C is the internal energy (strain energy) density and $F_{ij} = \partial \mathbf{x}_i / \partial \mathbf{X}_j$ is the deformation gradient. The Hamiltonian of the atomistic domain is

$$H^A = \sum_{\alpha \in \mathcal{M}} (\vartheta \frac{p_{i\alpha}^A p_{i\alpha}^A}{2m_\alpha^A} + \sum_{\beta \in \mathcal{M} > \alpha} \vartheta_{\alpha\beta} V_{\alpha\beta}) \tag{20}$$

where $\mathcal{M}$ is the set of all atoms, $p_{i\alpha}^A$ is the ith component of the linear momentum of atom α, m_α^A is the mass of atom α, $V_{\alpha\beta} = V(r_{\alpha\beta})$ is the potential of the bond between atoms α and β which is a function of the bond length of two atoms (i.e. $r_{\alpha\beta}$), $\vartheta_\alpha = \vartheta(\mathbf{X}_\alpha)$ and $\vartheta_{\alpha\beta} = (\vartheta(\mathbf{X}_\alpha) + \vartheta(\mathbf{X}_\beta))/2$.

The compatibility of deformation between atomistic and continuum domain in the overlapping zone can be imposed in different ways [12, 153, 46, 45]. For example, the compatibility of deformations can be obtained by requiring displacement of the atoms

conform to the continuum subdomain displacement field at the location of atoms [153]

$$\sum_{I\in\mathcal{S}} N_{I\alpha}u_{iI} - d_{i\alpha}, \quad \forall\alpha \in \mathcal{M} \tag{21}$$

The compatibility of deformation can also be obtained by requiring the atoms velocities match with the continuum velocity at the atoms location. In this case, the constraint on velocity is given by

$$\sum_{I\in\mathcal{S}} N_{I\alpha}\dot{u}_{iI} - \dot{d}_{i\alpha}, \quad \forall\alpha \in \mathcal{M} \tag{22}$$

where $\dot{d}_{i\alpha}$ and $\dot{u}_{iI}$ are the ith component of the velocity of atom α and finite element node I, respectively. The Lagrange multiplier constraints corresponding to equations 21 and 22 are given by

$$G^B = \sum_{\alpha\in\mathcal{M}} \lambda_{i\alpha}(\sum_{i\in\mathcal{S}} N_{I\alpha}u_{iI} - d_{i\alpha}), \tag{23a}$$

$$G^B = \sum_{\alpha\in\mathcal{M}} \lambda_{i\alpha}(\sum_{i\in\mathcal{S}} N_{I\alpha}\dot{u}_{iI} - \dot{d}_{i\alpha}), \tag{23b}$$

where $\lambda_{i\alpha}$ is the Lagrange multiplier associated with the constraint in the ith degree of freedom of atom α. Lagrange multipliers can be approximated using any λ-mesh which satisfies the LBB condition

$$\lambda(X,t) = \sum_{K\in\mathcal{S}^\lambda} N_K^\lambda(X)\lambda_K(t) \tag{24}$$

where $\mathcal{S}^\lambda$ is the set of λ-mesh nodes, N_K^λ denotes the shape functions associating with the λ-mesh and λ_K are the λ-mesh nodal value.

Total Lagrangian of the system can be obtained from Legendre transformation of Hamiltonian, from which the equations of motion (EOM) of the system can be

obtained as

$$M_\alpha^{\mathrm{A}} \ddot{d}_{i\alpha} = -(f_{i\alpha}^{\mathrm{int}})^{\mathrm{A}} + (f_{i\alpha}^{\mathrm{G}})^{\mathrm{A}}, \quad \forall \alpha \in \mathcal{M} \tag{25}$$

$$M_I^{\mathrm{C}} \ddot{u}_{iI} = -(f_{iI}^{\mathrm{int}})^{\mathrm{C}} + (f_{iI}^{\mathrm{G}})^{\mathrm{C}}, \quad \forall I \in \mathcal{S} \tag{26}$$

where $\ddot{d}_{i\alpha}$ and $\ddot{u}_{iI}$ are the ith components of the accelerations of atom α and FE-node I respectively, and

$$M_\alpha^{\mathrm{A}} = \vartheta_\alpha m_\alpha^{\mathrm{A}}, \tag{27}$$

$$(f_{i\alpha}^{\mathrm{int}})^{\mathrm{A}} = \vartheta_{\alpha\beta} \sum_{\beta \in \mathcal{M}} \frac{\partial V_{\alpha\beta}}{\partial d_{i\alpha}}, \tag{28}$$

$$(f_{i\alpha}^{\mathrm{G}})^{\mathrm{A}} = \sum_{K \in \mathcal{S}^\lambda} N_{K\alpha}^\lambda \lambda_{iK} \tag{29}$$

$$M_I^{\mathrm{C}} = \sum_{J \in \mathcal{S}} \int_{\Omega_0^{\mathrm{C}}} (1-\vartheta) \rho_0 N_I N_J d\Omega, \tag{30}$$

$$(f_{iI}^{\mathrm{int}})^{\mathrm{C}} = \int_{\Omega_0^{\mathrm{C}}} (1-\vartheta) \frac{\partial N_I}{\partial X_j} \mathbf{P}_{ij} d\Omega, \tag{31}$$

$$(f_{iI}^{\mathrm{G}})^{\mathrm{C}} = -\sum_{\alpha \in \mathcal{M}} \sum_{K \in \mathcal{S}^\lambda} N_{K\alpha}^\lambda N_{I\alpha} \lambda_{iK}, \tag{32}$$

where $\mathbf{P}$ is the nominal stress tensor, and M_I^{C} is a row-sum lumped mass matrix.

The Lagrange multipliers are obtained by enforcing

$$\frac{\partial H}{\partial \lambda_{iK}} = 0, \quad \forall K \in \mathcal{S}^\lambda, \tag{33}$$

which leads to

$$\sum_{\alpha \in \mathcal{M}} \sum_{I \in \mathcal{S}} N_{K\alpha}^\lambda N_{I\alpha} u_{iI} - \sum_{\alpha \in \mathcal{M}} N_{K\alpha}^\lambda d_{i\alpha} = 0, \quad \forall K \in \mathcal{S}^\lambda. \tag{34}$$

5.2.3 Time integration scheme

Since equations 25 and 26 are coupled with equation 34, it is not possible to simultaneously update both the displacements and Lagrange multipliers. Therefore, we employ a predictor-corrector velocity Verlet algorithm to update the atomistic and continuum displacement and velocity fields. In the velocity Verlet algorithm, the acceleration field is obtained using central difference method

$$\ddot{d}_{i\alpha}^{n} = \frac{1}{(\Delta t)^2}(d_{i\alpha}^{n+1} - 2d_{i\alpha}^{n} + d_{i\alpha}^{n-1}) \tag{35}$$

$$\ddot{u}_{iI}^{n} = \frac{1}{(\Delta t)^2}(u_{iI}^{n+1} - 2u_{iI}^{n} + u_{iI}^{n-1}) \tag{36}$$

in which Δt is the time-step size. By substituting equations 35 and 36 into equations 25 and 26, respectively, the displacement fields at step $n+1$ can be calculated as

$$d_{i\alpha}^{n+1} = (d_{i\alpha}^{n+1})^{\text{pre}} - \frac{(\Delta t)^2}{M_{\alpha}^{\text{A}}} \sum_{K \in \mathcal{S}^{\lambda}} N_{K\alpha}^{\lambda} \lambda_{iK} \tag{37}$$

$$u_{iI}^{n+1} = (u_{iI}^{n+1})^{\text{pre}} - \frac{(\Delta t)^2}{M_{I}^{\text{C}}} \sum_{\alpha \in \mathcal{M}} \sum_{K \in \mathcal{S}^{\lambda}} N_{K\alpha}^{\lambda} N_{I\alpha} \lambda_{iK} \tag{38}$$

in which the predicted displacements are

$$(d_{i\alpha}^{n+1})^{\text{pre}} = -\frac{(\Delta t)^2}{M_{\alpha}^{\text{A}}}(f_{i\alpha}^{\text{int}})^{\text{A}} + 2d_{i\alpha}^{n} - d_{i\alpha}^{n-1}, \tag{39}$$

$$(u_{iI}^{n+1})^{\text{pre}} = -\frac{(\Delta t)^2}{M_{I}^{\text{C}}}(f_{iI}^{\text{int}})^{\text{C}} + 2u_{iI}^{n} - u_{iI}^{n-1}, \tag{40}$$

Therefore; predicted displacements are obtained by ignoring Lagrange multipliers. The predicted displacements are used to find the Lagrange multipliers. To find Lagrange multipliers we use predicted displacements from equations 37 and 38 into

equation 34

$$\sum_{L\in\mathcal{S}^\lambda} A_{KL}\lambda_{iL} = \sum_{\alpha\in\mathcal{M}}\sum_{I\in\mathcal{S}} N^\lambda_{K\alpha}N_{I\alpha}(u^{n+1}_{iI})^{\text{pre}} - \sum_{\alpha\in\mathcal{M}} N^\lambda_{K\alpha}(d^{n+1}_{i\alpha})^{\text{pre}} \tag{41}$$

where A_{KL} is called consistent constraint matrix and is defined as

$$\begin{aligned} A_{KL} = &\sum_{\alpha\in\mathcal{M}}\sum_{I\in\mathcal{S}}\sum_{\beta\in\mathcal{M}} \frac{(\Delta t)^2}{M^{\text{C}}_I} N^\lambda_{K\alpha}N^\lambda_{L\beta}N_{I\alpha}N_{i\beta}u_{iI} \\ &- \sum_{\alpha\in\mathcal{M}} \frac{(\Delta t)^2}{M^{\text{A}}_\alpha} N^\lambda_{K\alpha}N^\lambda_{L\alpha}, \quad \forall K, L \in \mathcal{S}^\lambda \end{aligned} \tag{42}$$

An essential step in the bridging domain method is to use diagonalized constraint matrix AK instead of consistent constraint matrix [154]. The diagonalized constraint matrix is obtained from the consistent matrix as

$$A_K = \sum_{L\in\mathcal{S}^\lambda} A_{K_L} \tag{43}$$

Although the diagonalization step might seem arbitrary at first, however it is shown in Ref. [154], and will be shown in section 5.3, this step is quite essential in eliminating spurious wave reflections, and a consistent constraint matrix cannot remove the spurious reflections.

Our predictor-corrector algorithm can be summarized as follows: (1) we update the MD and FE displacement and velocity fields without considering the Lagrange multipliers, i.e. by ignoring $(f^G_{i\alpha})^{\text{A}}$ and $(f^G_{i\alpha})^{\text{C}}$ in equations 25 and 26. The displacement field obtained at this stage is called"predicted displacement field". (2) The predicted displacements will be used in equation 34 to find the Lagrange multipliers. (3) After finding the Lagrange multipliers, the predicted atomistic and finite element fields will be corrected by considering the Lagrange multiplier forces in equations 25 and 26.

These steps can be repeated until the displacement fields and Lagrange multipliers ($\mathbf{d}$; $\mathbf{u}$ and λ) converge.

5.3 Motivations

In this section, we discuss two issues associated with standard bridging domain method which motivated its enhancement with the proposed technique.

5.3.1 Discretization of lagrange multipliers

In the bridging domain method the compatibility of displacements between atomistic and continuum domains in the overlapping domain is enforced using Lagrange multipliers, as described in section 5.2. Lagrange multipliers can be discretized using any λ-mesh which satisfies the LBB condition. However, two forms of discretization are more common: (1) the Lagrange multiplier field is discretized to the atomistic spacing i.e. each atom in the bridging subdomain coincides with a λ-node. In this form the Lagrange multipliers are approximated as

$$\lambda(\mathbf{X}, t) = \sum_{\alpha \in \mathcal{B}} \lambda_\alpha \delta(\mathbf{X} - \mathbf{X}_\alpha), \tag{44}$$

where $\mathcal{B}$ is the set of atoms in the overlapping domain, and $\delta(\bullet)$ is the Dirac delta function. This form of approximation imposes a strict displacement compatibility between atomistic and continuum and is the form we will refer to as "BDM-strict" throughout this paper, (2) Lagrange multipliers are discretized by the same mesh as the FE-mesh i.e. each FE-node in the bridging subdomain coincides a λ-node. This form imposes a weaker compatibility between atomistic and continuum and is the form we will refer to as "BDM-weak". In the BDM-weak the λ-shape function of

each λ-node is the same as the corresponding FE-node shape function

$$N_K^{\lambda}(\mathbf{X}) = N_{IK}(\mathbf{X}), \quad \forall K \in \mathcal{S}^{\lambda} \tag{45}$$

where IK is the FE-node which coincides with the K-th node in the λ-mesh.

BDM-strict is more efficient in removing spurious wave reflections [153] and is the form which is often preferable. However, to enforce strict compatibility λ-mesh should be as fine as the atomistic distance. This can significantly increase the degrees of freedom associated with Lagrange multipliers which in turn can lead to a higher computational cost. Furthermore, when discontinuities are available in the overlapping zone, the displacement compatibility should be enforced weakly to allow crack surface relaxation [44]. Since the weak compatibility is not as efficient as strict compatibility in removing the spurious wave reflections, in this paper, we propose a method to enhance the performance of weak compatibility to match or supersede the performance of strict compatibility.

5.3.2 Impact of the integration time step size on the performance of BDM

In this section, we investigate how integration time step affects the performance of consistent and diagonalized constraint matrix in eliminating spurious wave reflections in a one-dimensional problem. For this purpose we study a 1D domain consisting of 292 atoms in the pure molecular dynamics zone and 60 finite elements of length h $= 8r_0$ in the continuum domain. The length of overlapping subdomain is 4h. The Lennard−Jones interatomic potential is used to describe the nearest neighbor atoms

interaction

$$V(r_{\alpha\beta}) = 4\epsilon[(\frac{\sigma}{r_{\alpha\beta}})^{12} - (\frac{\sigma}{r_{\alpha\beta}})^{6}] \tag{46}$$

in which $r_{\alpha\beta}$ is the distance between atoms α and β, and ϵ and σ are material specific input parameters. Here, we use atom mass $m_a = 1$ amu, $\epsilon = 0.2$ eV and $\sigma = 0.11$ nm. This set of Lennard−Jones parameter leads to an equilibrium bond length of r_0=0.135 nm. The constitutive equations of the continuum domain are obtained via the Cauchy−Born rule using the quasicontinuum approach [136].

The following initial displacements and velocities are applied to the atoms in the MD zone [154]:

$$u(X,0) = a_1(1+\cos(\frac{2\pi}{N_c r_0}(X)+\pi))(1+a_2\cos(\frac{\pi}{2r_0}X)), X \leq N_c r_0 \tag{47a}$$

$$v(X,0) = \frac{2\pi a_1 c}{N_c r_0}\sin(\frac{2\pi}{N_c r_0}(X)+\pi)(1+a_2\cos(\frac{\pi}{2r_0}X)), X \leq N_c r_0 \tag{47b}$$

$$u(X,0) = v(X,0) = 0, X > N_c r_0 \tag{47c}$$

in which $a_1 = 3 \times 10^{-4}$ nm, $a_2 = 0.3$, $N_c = 120$, and $c = 37.28$ nm/ps is the wave speed of a wave with infinite wavelength. The initial displacement field of the domain is shown in figure 37. The problem is solved using both diagonalized and consistent constraint matrix employing a small ($\Delta t = 0.00025$ ps) and a large ($\Delta t = 0.002$ ps) integration time step. Since the time it takes for a wave to propagate one atomic spacing is $\Delta t_0 = r/c = 0.0036$ ps, the large integration time step used in this example is in the same order as Δt_0, while the small integration time step is two order of magnitude less than Δt_0. To obtain the reference solution, and for the sake of comparison, the problem is also solved using full MD description for the

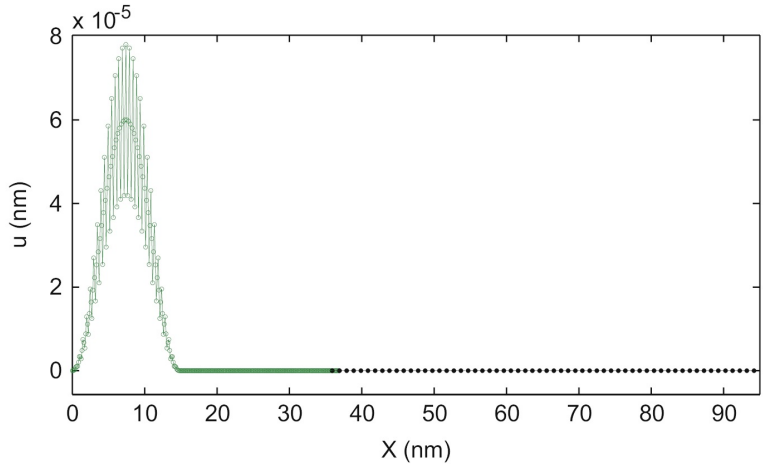

Figure 37: The initial displacements in the one-dimensional example (MD and continuum domains are shown respectively in green and black).

entire domain. The snapshots of the simulation results at $t = 2$ ps are depicted in figure 38. The snapshots of figure 38(a) and (b) show that consistent constraint matrix is not very successful in eliminating spurious reflections of high frequency waves into the MD domain using either large or small integration time steps. These results are in agreement with those reported by [154]. In contrast, the efficiency of diagonalized constraint matrix in damping out the high frequency components of the wave depends on the integration time step. Snapshot of figure 38(c) and (d) indicates that when larger integration time step is used, the diagonalized constraint matrix can suppress the wave reflections, however when smaller integration time step is used, the diagonalized constraint matrix is not capable of eliminating spurious wave reflections. Hence, reducing the size of the integration time steps deteriorates the performance of the method. This is in contrast with our expectation of obtaining a higher accuracy when a smaller integration time step is used.

The problem is more studied by investigating the variation of the Hamiltonian of the

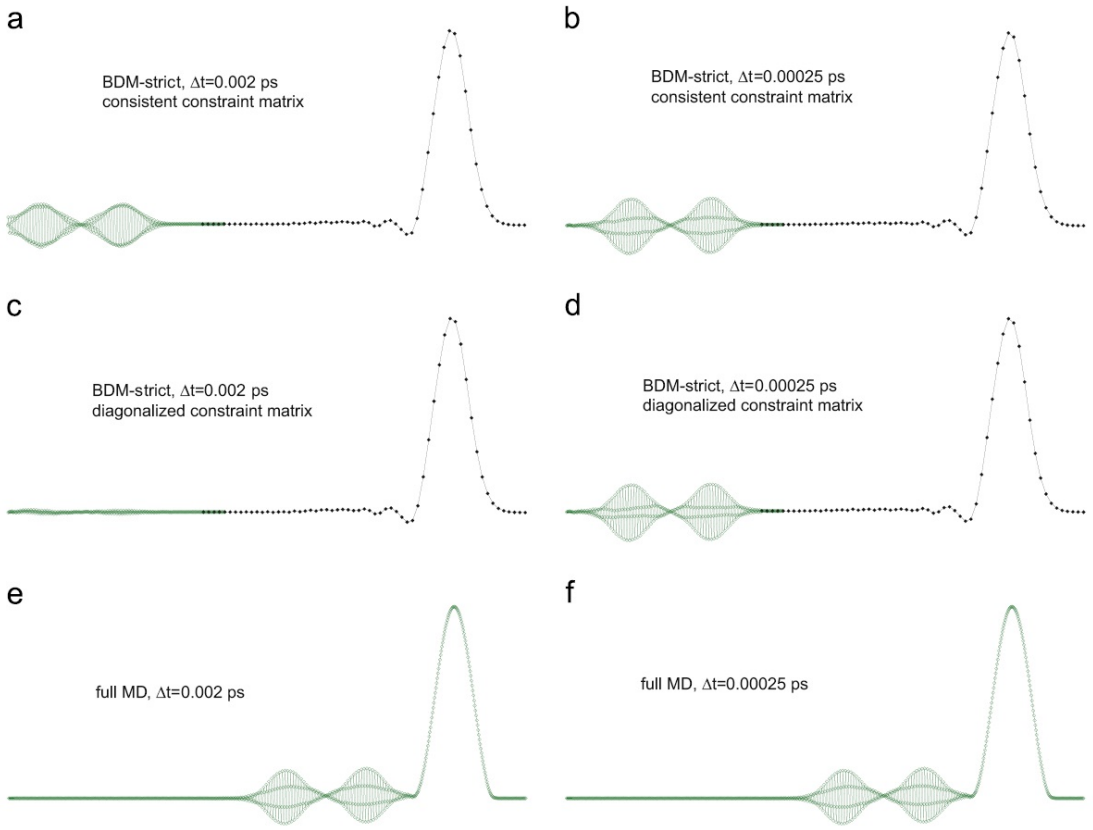

Figure 38: Snapshots of the 1D problem using consistent and diagonalized constraint matrix.

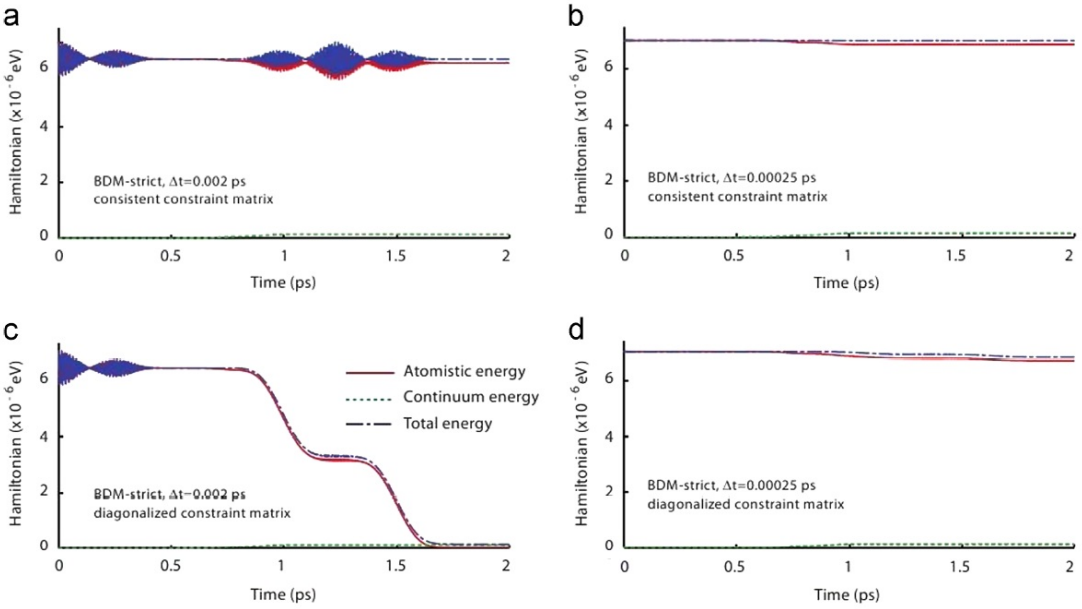

Figure 39: Total Hamiltonian ($\times 10^{-6}$ eV) of the entire system, pure MD zone and continuum subdomain of the one-dimensional simulation using consistent and diagonalized constraint matrix.

system over time. The Hamiltonian of the entire domain along with the Hamiltonian of the atomistic and continuum subdomains are shown in figure 39. If the waves travel out of the atomistic zone, i.e. spurious reflections do not occur, the Hamiltonian of the atomistic zone should go to zero. The plots of figure 39(a) and (b) show that when consistent constraint matrix is employed, the Hamiltonian of the entire system remains constant and the Hamiltonian of atomistic zone does not go to zero. These indicate that no component of the wave is damped, hence spurious reflection is not eliminated and high frequency components of the wave are trapped in the atomistic zone. These are in agreement with the snapshots presented in figure 38(a) and (b).

The Hamiltonians obtained using diagonalized constraint matrix are shown in figure 39(c) and (d). Plots of figure 39(c) show that when diagonalized constraint matrix with larger integration time step is used, the Hamiltonian of the atomistic zone goes to zero after about 1.6 ps. Therefore, no wave component is trapped in the atomistic zone. The wave coarse components have traveled into the continuum domain and the high frequency components are eliminated, as is shown in figure 38(c). The plots of figure 39(b) show that when the integration time step size is reduced, the initial oscillations of Hamiltonian seen in figure 39(b) are removed. However, the Hamiltonian of atomistic zone does not go to zero, indicating that spurious wave reflection of high frequency waves is not prevented.

The plots of figure 39(c) and (d) show that by reducing the integration time step the performance of the diagonalized constraint matrix becomes similar to the performance of the consistent constraint matrix, i.e. high frequency waves which cannot travel into continuum subdomain spuriously reflect back into the atomistic zone,

hence the Hamiltonian of atomistic zone never goes to zero. The deterioration of the performance by reduction of integration time step size is not desirable because large integration time steps can lead to large oscillations in system energy which can significantly reduce the computational accuracy.

To resolve the two above-mentioned issues, we propose an enhanced bridging domain method (EBDM). Although the proposed enhancement can be applied to both weak and strict compatibility, in this study we apply the enhancement to the weak compatibility form. Using numerical examples we show the effectiveness of the proposed method.

5.4 Proposed enhancement of the bridging domain method

The basic idea of our proposed method is to decompose the total displacement of the atoms located in the overlapping zone into fine and coarse scale components. The fine scale oscillations corresponds to high frequency oscillations which cannot pass into the finite element zone, and will spuriously reflect back if they are not damped out. To remove spurious reflections, the fine scale oscillations need to be removed. For this purpose, we obtain the equations of motion of fine scale oscillations and modify it to include a damping term.

The decomposition of atomistic displacement field into coarse and fine scales was first proposed by Liu et al. [144, 89] in developing bridging scale method. This idea was later used to develop other multiscalemethods such as perfectly matchedmultiscale method [141]. More recently, Sadeghirad and Tabarraei [121] used this idea to develop a multiscale technique which can effectively remove spurious reflections. In

this section, we apply the technique developed in Ref. [121] to BDM. We first derive the equations off motion of fine scale oscillations in the BDMformulation and present a numerical algorithm for the implementation of the proposed enhancement in the BDM framework.

5.4.1 Formulation of the enhanced bridging domain method

In the enhanced bridging domain method (EBDM), the total displacement field of atoms located in the overlapping zone is decomposed into a fine and a coarse scale displacement field

$$d_{i\alpha} = (d_{i\alpha})^{\text{coarse}} + (d_{i\alpha})^{\text{fine}}, \quad \forall \alpha \in \mathcal{M}, \tag{48}$$

where $d_{i\alpha}$ is the total displacement of atom α in the ith direction, and $(d_{i\alpha})^{\text{coarse}}$ and $(d_{i\alpha})^{\text{fine}}$ are its coarse and fine components, respectively. We correspond the coarse scale field to the oscillations which can be resolved by the continuum mesh and smoothly pass into the continuum zone without difficulty. Therefore, the continuum displacement field can be used to constitute the coarse scale part of the displacement field. Using standard finite element interpolation, the coarse scale displacement field of atoms can then be approximated as

$$(d_{i\alpha})^{\text{coarse}} = u_i(X_\alpha) = \sum_{I \in \mathcal{S}^B} N_{I\alpha} u_{iI}, \quad \forall \alpha \in \mathcal{M}^B \tag{49}$$

By substituting equation 49 in equation 48, the fine scale component of the displacement field is obtained

$$(d_{i\alpha})^{\text{fine}} = d_{i\alpha} - \sum_{I \in \mathcal{S}^B} N_{I\alpha} u_{iI}, \quad \forall \alpha \in \mathcal{M}^B. \tag{50}$$

The fine scale accelerations are obtained by taking the time derivatives of equation 50 twice

$$(\ddot{d}_{i\alpha})^{\text{fine}} = \ddot{d}_{i\alpha} - \sum_{I \in \mathcal{S}^B} N_{I\alpha} \ddot{u}_{iI}, \quad \forall \alpha \in \mathcal{M}^B. \tag{51}$$

Multiplying equation 51 with atoms mass yields

$$M_\alpha (\ddot{d}_{i\alpha})^{\text{fine}} = M_\alpha \ddot{d}_{i\alpha} - \sum_{I \in \mathcal{S}^B} N_{I\alpha} M_\alpha \ddot{u}_{iI} \tag{52}$$

Using equations 25 and 26 in 52 gives

$$M_\alpha^{\text{A}} (\ddot{d}_{i\alpha})^{\text{fine}} = (f_{i\alpha}^{\text{A}})^{\text{fine}}, \quad \forall \alpha \in \mathcal{M}^B \tag{53}$$

where

$$(f_{i\alpha}^{\text{A}})^{\text{fine}} = M_\alpha^{\text{A}} \left[\frac{(f_{i\alpha}^{\text{int}})^{\text{A}} + (f_{i\alpha}^{\text{G}})^{\text{A}}}{M_\alpha^{\text{A}}} - \sum_{I \in \mathcal{S}^B} N_{I\alpha} \frac{(f_{iI}^{\text{int}})^{\text{C}} + (f_{iI}^{\text{G}})^{\text{C}}}{M_I^{\text{C}}} \right]. \tag{54}$$

This is the equation of motion of fine scale oscillations. The fine scale displacements cannot be resolved by the continuum mesh and should be eliminated. This is accomplished by adding a viscous damping term to 52

$$M_\alpha^{\text{A}} (\ddot{d}_{i\alpha})^{\text{fine}} = (\bar{f}_{i\alpha}^{\text{A}})^{\text{fine}} - M_\alpha^{\text{A}} C_\alpha^{\text{A}} (\dot{d}_{i\alpha})^{\text{fine}}, \tag{55}$$

where C_α^{A} is the damping coefficient. Using viscous damping, a damping force proportional to fine velocity of the atom is applied to the fine motion of each atom. The selection of an appropriate damping coefficient is described in section 5.4.3.

5.4.2 Implementation of the enhanced bridging domain method

Assume that displacements are known at time step n and we intend to proceed to time step $n+1$. For this purpose, first the equations of section 5.2.3 are used

to find the total atomic and finite element displacements at step $n+1$. After the total displacement fields are found, the technique proposed in this paper is applied only to the atoms located in the overlapping zone. Since, these atoms compose a small fraction of the total atoms of the domain, the additional computational cost introduced by this extra step is negligible.

The velocity Verlet algorithm can be used to integrate equation 55 in time

$$(d_{i\alpha}^{n+1})^{\text{fine}} = (d_{i\alpha}^{n})^{\text{fine}} + \Delta t(\dot{d}_{i\alpha}^{n})^{\text{fine}} + \frac{1}{2}\Delta t^2(\ddot{d}_{i\alpha}^{n})^{\text{fine}} \tag{56a}$$

$$(\dot{d}_{i\alpha}^{n+1/2})^{\text{fine}} = (\dot{d}_{i\alpha}^{n})^{\text{fine}} + \frac{1}{2}\Delta t(\ddot{d}_{i\alpha}^{n})^{\text{fine}} \tag{56b}$$

$$(\ddot{d}_{i\alpha}^{n+1})^{\text{fine}} = \frac{1}{M_\alpha}(f_{i\alpha}^{n+1})^{\text{fine}} - C_\alpha(\dot{d}_{i\alpha}^{n+1/2})^{\text{fine}} \tag{56c}$$

$$(\dot{d}_{i\alpha}^{n+1})^{\text{fine}} = (\dot{d}_{i\alpha}^{n+1/2})^{\text{fine}} + \frac{1}{2}\Delta t(\ddot{d}_{i\alpha}^{n+1})^{\text{fine}} \tag{56d}$$

After calculating the fine scale displacements, the total atomic displacements are obtained by adding the coarse and fine scale components together

$$d_{i\alpha}^{n+1} = (d_{i\alpha}^{n+1})^{\text{fine}} + \sum_{I\in\mathcal{S}^B} N_{I\alpha}u_{iI}^{n+1}, \quad \forall\alpha\in\mathcal{M}. \tag{57}$$

This gives the total atomic displacement after the elimination of fine scale oscillations.

5.4.3 Conditions for damping coefficient

The choice of the damping coefficient plays an important role in the success of the method in reducing spurious wave reflections. This necessitates some considerations to be taken into account when the damping coefficient is chosen. Application of the damping term can change the band structure of the overlapping subdomain which in turn can increase the spurious wave reflections. More specifically, the damping

can increase the spurious reflections at the interface of bridging domain and pure atomistic zone (i.e. $\Omega_{\mathrm{A}} - \Omega_{\mathrm{B}}$). To overcome this issue, the damping should not be applied suddenly, instead the damping should gradually increases from zero at Γ_{C} to a maximum value at Γ_{A} (see figure 36). Although different forms of damping function can be constructed which satisfy this condition, however in this paper, by getting insights from the semi-empirical damping function proposed by Collino and Tsogka [25] we approximate the damping coefficients using a parabolic equation in this form

$$C_{\alpha}^{\mathrm{A}} = \bar{C}\frac{c}{L^{\mathrm{B}}}(1 - \vartheta(\mathbf{X}))^2, \quad \forall \alpha \in \mathcal{M}^{B}. \tag{58}$$

In equation 58 c is the wave speed, L^{B} is the width of the bridging subdomain, $\vartheta(\mathbf{X})$ is the linear weight function of equation 16, and C is a user-defined parameter. Using this approximation, very little spurious reflections are developed near Γ^{C}, and the fine scale displacements are effectively eliminated. A small value of $C = 30$ will lead to inefficient damping, whereas if $C = 30$ is too large, numerical instability will occur. In this paper, based on our experience in solving an extended number of numerical examples, we adopt a value of $C = 30$ in the numerical simulations presented in the next section.

5.5 Numerical simulations

We solve one and two dimensional examples to investigate the performance of the proposed enhancements. The problems are solved numerically using BDM-strict, BDM-weak and the proposed enhance bridging domain method (EBDM). Diagonalized constraint matrix is used to solve all the problems. All the numerical simulations

are conducted at an absolute zero temperature and the reference solution of all the problems are obtained by using a fully atomistic description of the entire domain.

5.5.1 One-dimensional example

The first problem solved in this section is the one-dimensional problem presented in section 5.3.2. The initial boundary conditions presented in equation 47 are applied to the atomistic zone. A Lennard-Jones potential with the same material parameters of section 5.3.2 is used to consider the interaction between atoms. To study the effect of time integration step size on the performance of the method, this problem is solved using three different time steps. The effect of overlapping length on eliminating spurious reflections is studied by solving the problem using three different overlapping lengths of size $n_b h$, with n_b =1,2,4. Also, we solve the problem using both displacement constraint and the velocity constraint.

The snapshots of the wave propagation obtained using a time step size of ΔT =0.002 ps at $t = 2$ ps are shown in figure 40. These snapshots show that BDM-weak is not capable in removing spurious reflections, whereas both BDM-strict and EBDM are able to remove spurious reflections.

The total Hamiltonian of the atomistic zone versus time obtained using displacement and velocity constraints are shown in figures 41 and 42, respectively. For the sake of comparison, the results obtained from a full MD simulation are also presented. Since the initial waves are traveling out of the atomistic zone, the Hamiltonian of the pure atomistic zone should go to zero. This can be seen in the plots of figure 41a obtained using full MD simulations.

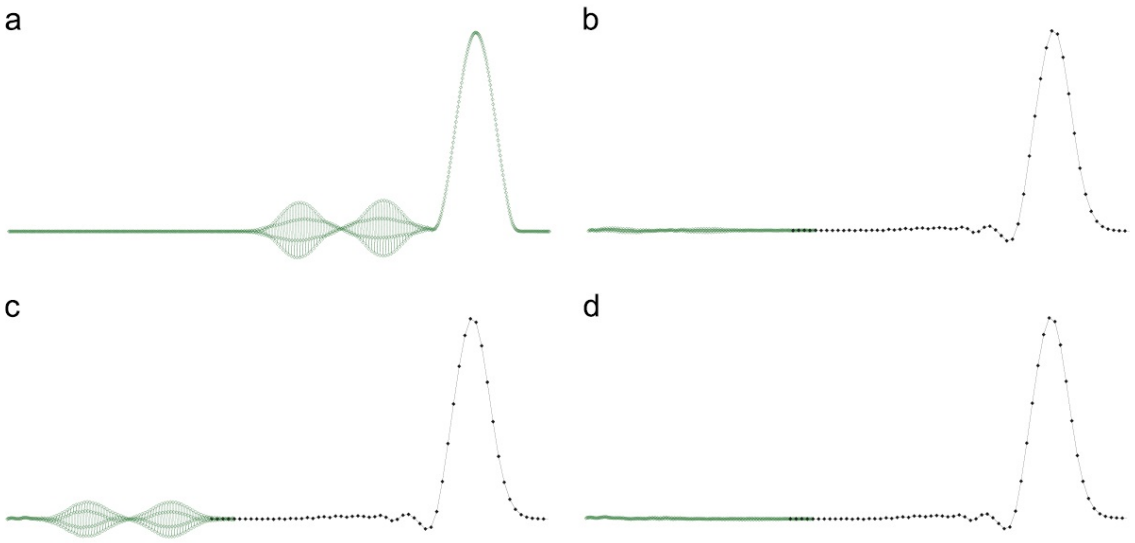

Figure 40: Four snapshots of the one-dimensional model at $t = 2$ ps obtained using a time step of 0.002 ps. (a) Full MD, (b) BDM-strict, (c) BDM-weak, (d) and BDM-weak with damping.

The results obtained from strict and weak BDM are shown in figure 41(b)∼(g) and figure 42(b)∼(g). These plots show that, as expected, strict compatibility is more successful in eliminating spurious wave reflections than weak compatibility. These plots also confirm that regardless of the size of the overlapping domain, standard BDM methods are more successful in removing spurious reflections when the integration time step is large. An important observation can be made by comparing results presented in figure 41(b)∼(d) with those presented in figure 42(b)∼(d). These plots indicate that when velocity constraint is used, the size of integration time step does not influence the performance of standard BDM methods as severely and adversely as when displacement constraint is used.

The results obtained using the proposed enhanced bridging domain method are presented in figure 41(h)∼(j) and figure 42(h)∼(j). These plots show that EBDM is more efficient than both strict and weak-BDM method in eliminating spurious reflec-

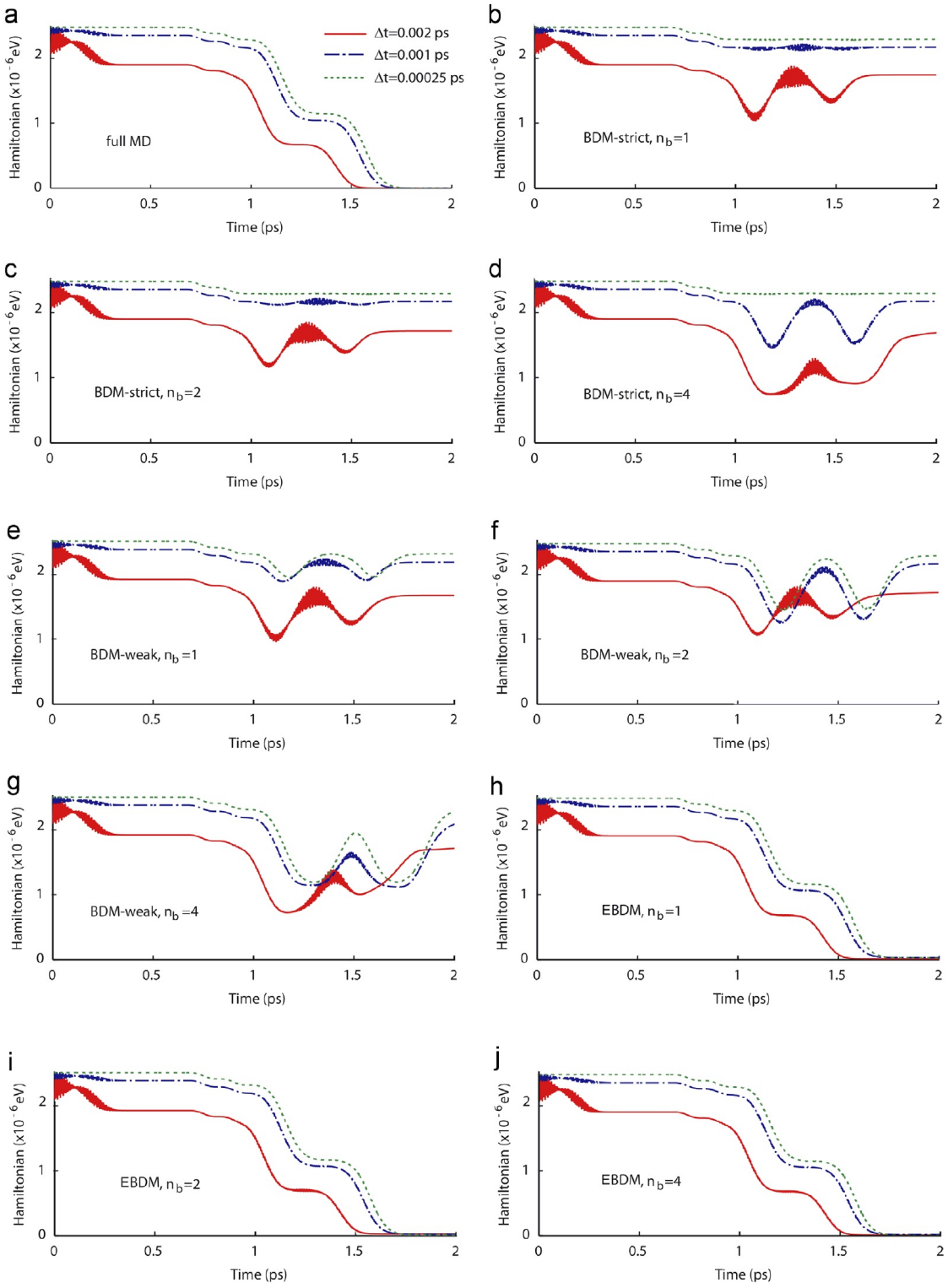

Figure 41: Total Hamiltonian ($\times 10^{-6}$ eV) of the molecular dynamics zone versus time (ps) of the one-dimensional simulation obtained using displacement constraint. (a) Full MD, (b) BDM-strict and $n_b = 1$, (c) BDM-strict and $n_b = 2$, (d) BDM-strict and $n_b = 4$, (e) BDM-weak and $n_b = 1$, (f) BDM-weak and $n_b = 2$, (g) BDM-weak and $n_b = 4$, (h) EBDM and $n_b = 1$, (i) EBDM and $n_b = 2$, and (j) EBDM and $n_b = 4$.

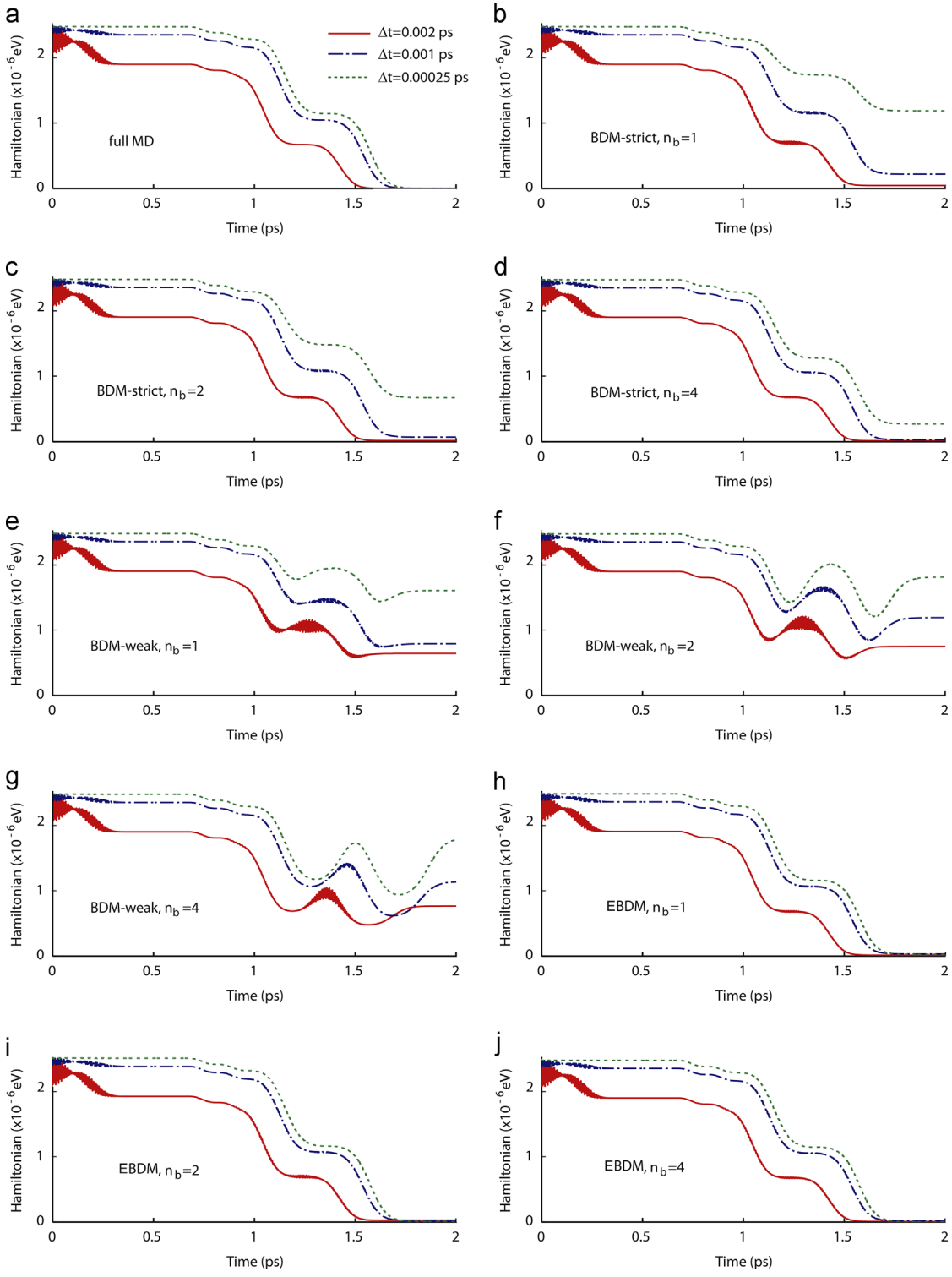

Figure 42: Total Hamiltonian ($\times 10^{-6}$ eV) of the molecular dynamics zone versus time (ps) of the one-dimensional simulation obtained using velocity constraint. (a) Full MD, (b) BDM-strict and $n_b = 1$, (c) BDM-strict and $n_b = 2$, (d) BDM-strict and $n_b = 4$, (e) BDM-weak and $n_b = 1$, (f) BDM-weak and $n_b = 2$, (g) BDM-weak and $n_b = 4$, (h) EBDM and $n_b = 1$, (i) EBDM and $n_b = 2$, and (j) EBDM and $n_b = 4$.

tions. The enhancement in the performance is more significant when the overlapping length size is small ($n_b = 1$). Furthermore, these plots indicate that our enhancement removes the adverse effect of reduction in the size of time step; by reducing the time step size the performance of EBDM improves, showing the same exact trend as is observed in the results obtained from full MD simulations.

5.5.2 Propagation of a centeral crack under dynamic tensile loading

The effectiveness of the proposed method in modeling crack propagation is investigated by simulating growth of a crack located at the middle of a two-dimensional domain which is under uniaxial tensile loading. The atomistic subdomain is made of a triangular lattice which corresponds to the [111] plane of an FCC crystal. The interatomic interactions are modeled using the Lennard- Jones interatomic potential presented in equation 46. Only nearest neighbor atoms are used in the evaluation of interatomic potentials. For this problem, we use ϵ =0.467 eV and σ =0.2296 nm which leads to an equilibrium bond length of $r_0 = 0.2577$ nm of the triangular lattice. An atom mass of m_a=64 amu is used in the simulations. The initial geometry and boundary conditions of the domain are shown in figure 44. The entire domain dimensions are 63.02 nm$\times$60.49 nm and the initial crack length is 10 nm. A linearly rising velocity ramp followed by a plateau (figure 43) is applied to the upper and lower edges of the continuum domain. The two side edges of the domain are traction free. The effect of overlapping width on the performance of the method is studied by solving the problem using two overlapping size of length L^B =1.78 nm and L^B =7.06 nm as are shown in figure 44.

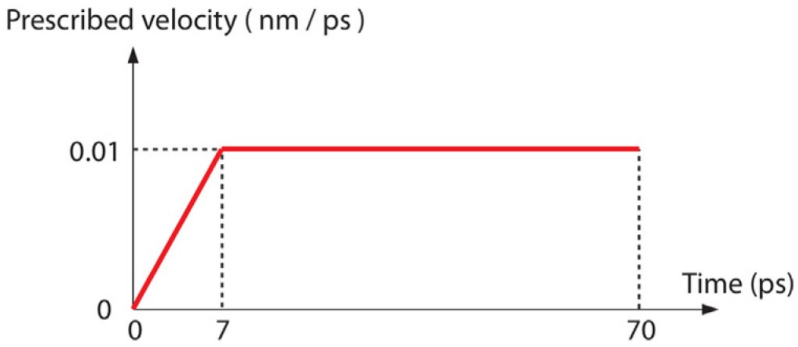

Figure 43: The velocity boundary condition applied to the top and bottom edges of the continuum domain.

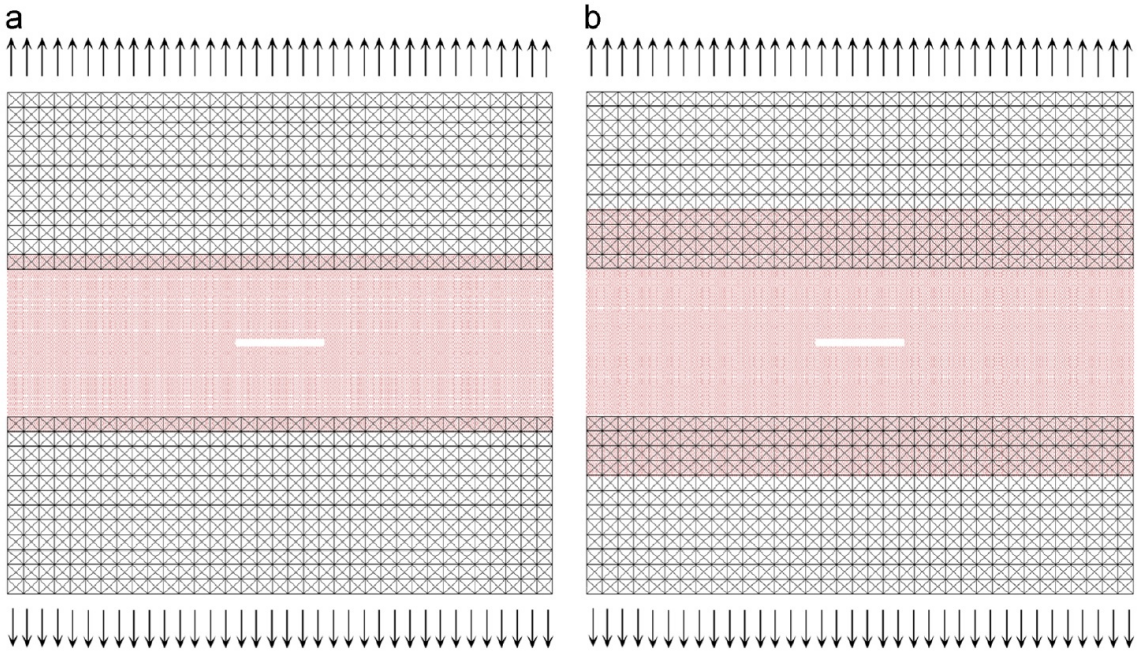

Figure 44: Schematic of the initial geometry and boundary conditions of a square domain containing a central crack. The MD zones are shown in pink color. The overlapping width L^B is (a) 1.78 nm and (b) 7.06 nm. (For interpretation of the references to color in this figure caption, the reader is referred to the web version of this article.)

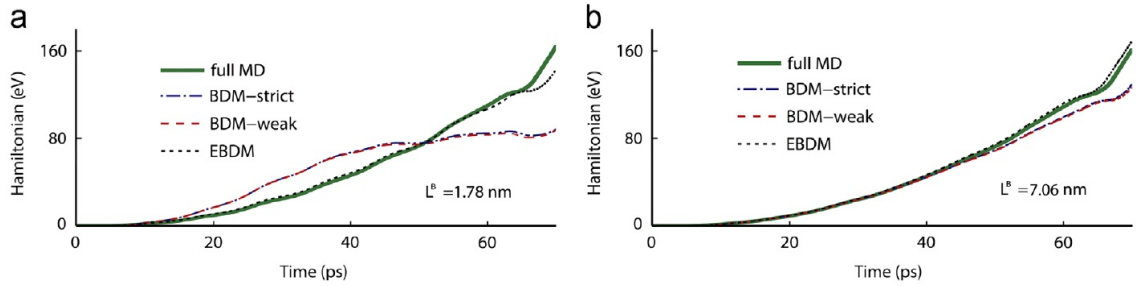

Figure 45: Total Hamiltonian of the two-dimensional domain with a central crack under tensile loading. (a) L^B =1.78 nm and (b) L^B =7.06 nm.

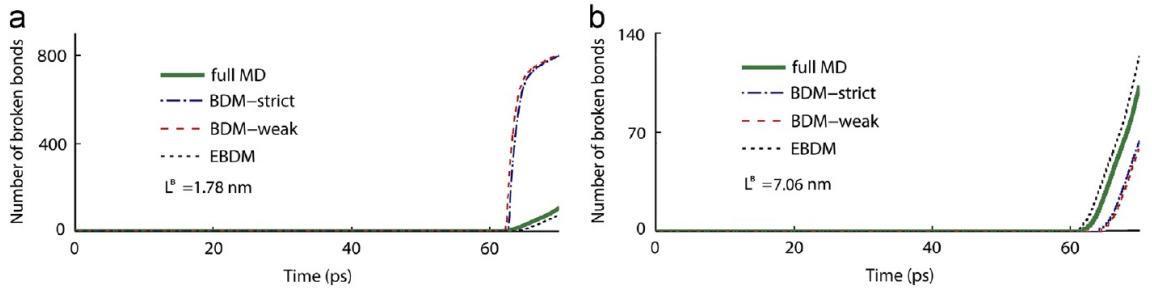

Figure 46: Number of broken bonds of the two-dimensional domain with a central crack under tensile loading. (a) L^B =1.78 nm and (b) L^B =7.06 nm.

The variation in total Hamiltonian of the domain versus time is shown in figure 45. The graphs of figure 45 show that the Hamiltonian of the system obtained from EBDM is in close agreement with the full MD simulations using both small or large overlapping subdomain. However, when standard weak or strict bridging domain methods are used, the Hamiltonian of the system will approach the full MD results only when the size of the overlapping domain is large.

The number of broken bonds of the pure MD zone versus time is shown in figure 46. It can be observed that when the overlapping width is small, standard BDM methods vastly overestimate the number of broken bonds. However, the number of broken bonds obtained from EBDM is in agreement with full MD results using both small and large overlapping size.

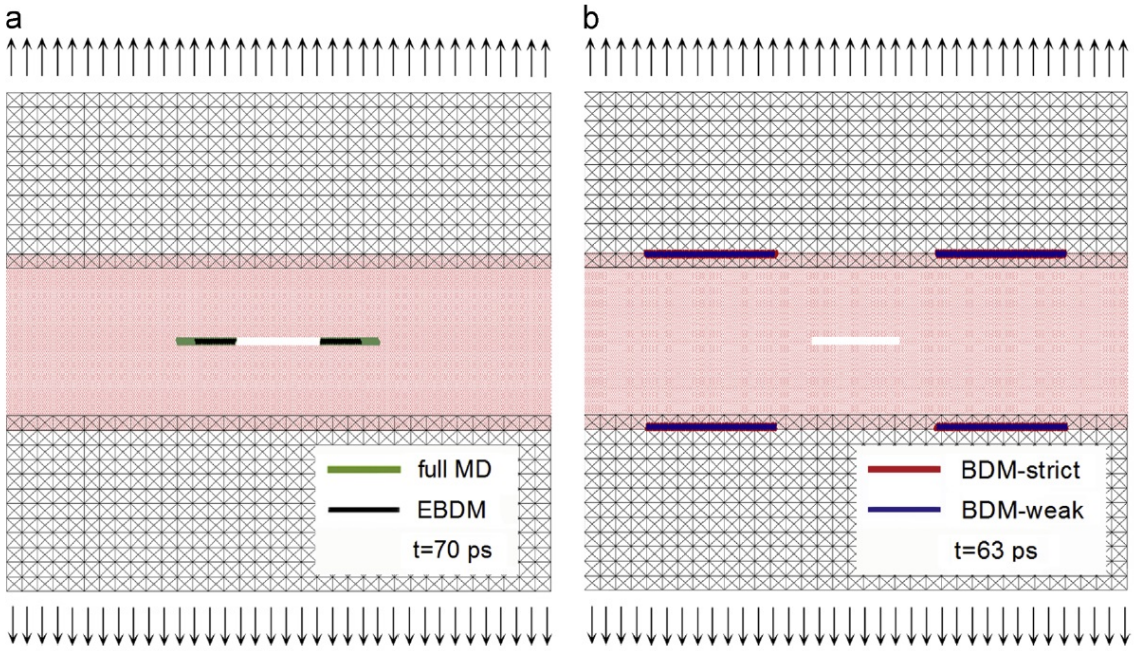

Figure 47: Crack path of the full MD and the BDM simulations for L^B =1.78 nm. (a). Crack path from the full MD and enhanced BDM simulation at t = 70 ps. (b). Crack path from the strict BDM and weak BDM at t=63 ps.

We further compare the performance of the techniques by investigating the crack path obtained from each method. The crack growth paths obtained using small overlapping length are schematically shown in figure 47. This figure clearly shows that when full MD or EBDM method are used, the initial crack grows self-similar (coplanar) from the initial crack. However, when standard BMD methods are employed to model crack growth, the initial crack does not grow, instead atomic bonds break at the interface of continuum and overlapping zone, leading to the generation of new cracks along ΓA. The new cracks then grow along ΓA to the side edges of the domain. By increasing the size of overlapping zone, the crack growth path obtained from standard BDM approaches that of pure MD, however this example clearly shows that EBDM is more efficient in modeling problems involving discontinuities.

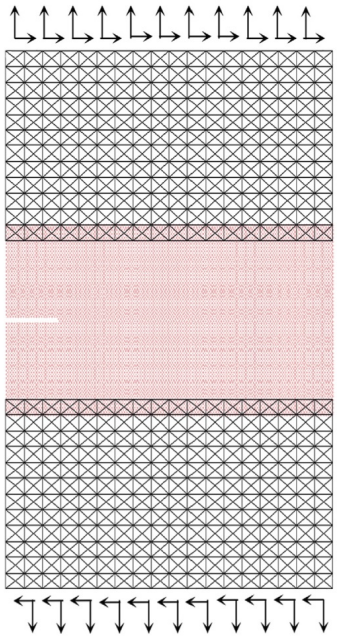

Figure 48: Initial geometry and boundary conditions of a domain with an edge crack under tensile and shear loading.

5.5.3 Edge crack propagation under mixed mode loading

In the previous example, crack growth under uniaxial tensile test was studied. In this example we examine the capability of the method in modeling crack propagation under mixed mode loading. For this purpose we consider a cracked domain under mixed tensile-shear loading.

The initial geometry and boundary conditions of the problem are shown in figure 48. The domain dimensions are 32.41 nm $\times$ 60.50 nm and the initial crack length is 5.0 nm. A tensile and shear loading act simultaneously at the top and bottom edges of the domain. The velocity function shown in figure 43 is used to prescribe both tensile and shear components of the external loading. The side edges of the domain remain traction free. The same lattice structure and interatomic potential used for the example of section 5.5.2 are used to solve this problem.

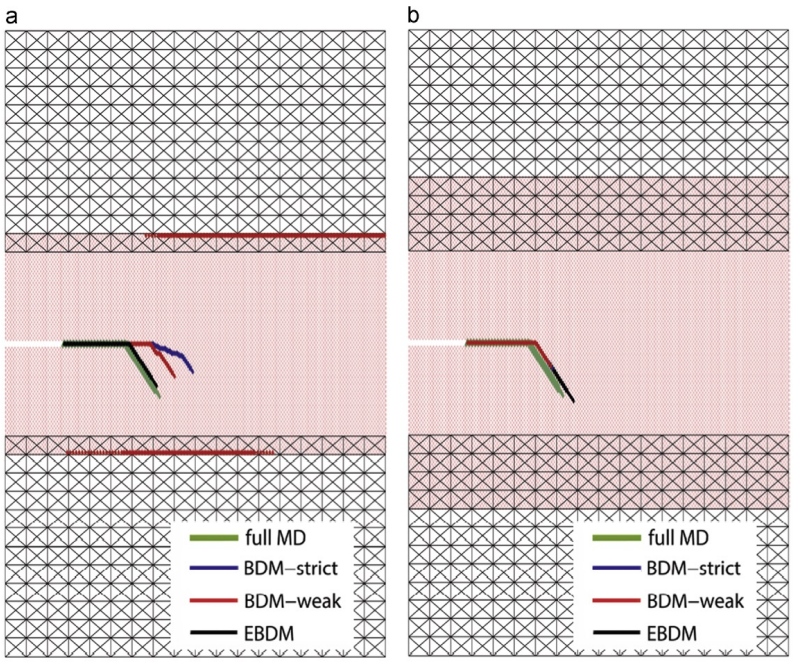

Figure 49: Crack path of an edge crack under combined shear and tensile loading. (a) Short overlapping width, L^B=1.78 nm and (b) large overlapping width, L^B=7.06 nm.

The crack propagation path obtained from all the simulations are shown in figure 49(a) and (b). These figures clearly show that if the overlapping width L^B is small, only EBDM is able to predict the crack path correctly. On the other hand, when overlapping width is small, not only the crack paths obtained from BDM-strict and BDM-weak do not coincide with the MD result, but also atom bonds along the top and bottom of the MD zone are also breaking. Therefore, standard BDM methods are capable of predicting the correct crack path only when the overlapping length is large. These results clearly demonstrate the superior efficiency of the enhanced bridging domain method (EBDM) proposed in this paper with respect to the standard bridging domain method.

5.6 Conclusion

In this paper, we investigated the performance of standard bridging domain method as a function of overlapping length size, the form of Lagrange multipliers discretization (strict versus weak compatibility), the type of constraint matrix (consistent versus diagonalized), the integration time step size, and the type of constraint between atomistic and continuum domain in the overlapping zone (displacement versus velocity constraint). Our numerical simulations indicate that:

(1) by increasing the width of overlapping zone, the performance of bridging domain method improves.

(2) Strict compatibility is more efficient than weak compatibility in removing spurious reflections.

(3) Performance of diagonalized constraint matrix in removing the spurious reflections is significantly better than consistent constraint matrix.

(4) By reducing the size of time step the capability of standard BDM in eliminating spurious reflections reduces.

(5) Velocity constraint is less sensitive to time integration step size and is the form of constraint which should be used.

The key contribution of the chapter is to testify the new technique to enhance the performance of bridging domain method in eliminating the spurious wave reflections at the interface of atomistic and continuum domain. In our proposed enhancement the overlapping zone plays two important roles: (a) it glues the continuum domain to atomistic domain, and (b) it is used as a damping zone which damps the high

frequency waves that cannot travel into the continuum domain. To damp the high frequency waves, we decomposed the total displacement field of atoms located within the overlapping zone into a fine and coarse scale. The fine scale oscillations correspond to the small wavelength (high frequency) components of the wave and need to be eliminated. To damp the fine scale oscillations, we included a viscous damping term in their equations of motion.

Our numerical results showed that the proposed enhancement significantly improves the capability of the bridging domain method in removing the spurious reflections. In contrast to the standard bridging domain methods, by reducing the time step size, the performance of enhanced bridging domain method improves. Also, the numerical results obtained from one and two-dimensional problems indicate that the proposed technique is capable in eliminating spurious reflections using a much smaller overlapping length than those required by the standard BDM.

CHAPTER 6: PERIDYNAMICS STUDY OF THE FRACTURE BEHAVIOR OF MOS_2 AND H-BN

6.1 Introduction

Recently, fracture modeling techniques based on peridynamics nonlocal continuum theory have been developed. In peridynamics, the forces acting at a particle are obtained by an integral operator that sums pairwise internal forces exerted on the particle by all the particles located at a finite distance from the particle of interest. In contrast to classical continuum theory, peridynamics theory does not make any assumption on the differentiability of displacement field for obtaining the forces. The main advantage of peridynamics is that no assumption is made on the continuity of the displacement field hence discontinuity in the displacement field due to the presence of cracks does not necessitate special treatments. Peridynamics performance has been validated by applying it to several sophisticated applications including polycrystals fracture [7], fracture of composite materials [66, 150, 151, 61, 36], structure stability and failure analysis [68], modeling of structure response under extreme loading [30], material fragmentation under impact [129] dynamic fracture analysis [1, 131, 67, 48, 47], simulation of the kinetic of phase transformation [28] and modeling heat transition in bodies with evolving cracks [16]. In addition to the numerical verifications, rigorous mathematical analysis have been used to examine the properties of peridynamics. Silling and Lehoucq [130] showed that in the limit when nonlocal region around a point

goes to zero, peridynamics converges to classical elasticity theory. Du and Zhou [75] developed a functional analytical framework for peridynamics and demonstrated the connections between peridynamics and classical elastic theory, and Alali and Lipton [3] analytically investigated the multiscale dynamics of heterogeneous media using peridyanmic formulation.

In this chapter, 2D peridynamics is used to simulate the crack's propagation process in single layer MoS_2 and h-BN sheets under mix-mode loadings.

6.2 Basic formulation of peridynamics

Peridynamic is a nonlocal continuum theory in which a point $\mathbf{x}$ interacts with other points in its vicinity. The interaction zone of a node is called horizon and is denoted by δ. The vector from a point $\mathbf{x}$ to point $\mathbf{x}'$ is called a bond defined by $\boldsymbol{\xi} = \mathbf{x}' - \mathbf{x}$ and the bond length is denoted by $\xi = |\boldsymbol{\xi}|$. The deformation state of a bond $\boldsymbol{\xi}$ at time t is defined as

$$\mathbf{Y}[\mathbf{x}, t] \langle \boldsymbol{\xi} \rangle = \mathbf{y}(\mathbf{x} + \boldsymbol{\xi}, t) - \mathbf{y}(\mathbf{x}, t) \tag{59}$$

where

$$\mathbf{y}(\mathbf{x}, t) = \mathbf{x} + \mathbf{u}(\mathbf{x}, t), \tag{60}$$

and $\mathbf{u}$ is the displacement vector field. $\mathbf{Y}[\mathbf{x}, t]$ acts on bond $\boldsymbol{\xi}$ and produces the image of the bond under deformation.

The peridynamic equation of motion of point $\mathbf{x}$ is

$$\rho(\mathbf{x})\ddot{\mathbf{u}}(\mathbf{x}, t) = \int_H (\underline{\mathbf{T}}[\mathbf{x}, t] \langle \mathbf{x}' - \mathbf{x} \rangle - \underline{\mathbf{T}}[\mathbf{x}', t] \langle \mathbf{x} - \mathbf{x}' \rangle) dV_{\mathbf{x}'} + \mathbf{b}(\mathbf{x}, t), \tag{61}$$

where $\underline{\mathbf{T}}$ is the force state and H is the set of all the bonds connected to $\mathbf{x}$. The force

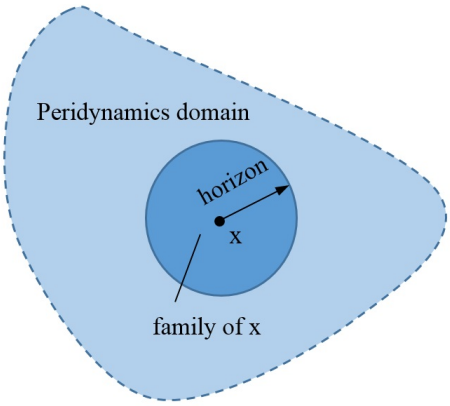

Figure 50: The motion of a point $\mathbf{x}$ is based on an integration over its family. The radius of the family domain is called the horizon.

state $\underline{\mathbf{T}}[(\mathbf{x}, t)]$ takes the bonds connected to point $\mathbf{x}$ as input and produces a force density vector as the output. Since $\underline{\mathbf{T}}$ acts on a vector and produce a vector, $\underline{\mathbf{T}}$ is similar to a tensor with the difference that $\underline{\mathbf{T}}$ is not necessarily linear or continuous. For an elastic material $\underline{\mathbf{T}}$ only depends on $\mathbf{Y}([\mathbf{x}, t])$ and can be obtained from the strain energy function W by

$$\underline{\mathbf{T}}(\mathbf{Y}) = \nabla \psi^{PD}(\mathbf{Y}), \tag{62}$$

where ∇ denotes the Fréchet derivative with respect to $\mathbf{Y}$. The strain energy function of a linear elastic material is

$$\psi^{PD}(\theta, \underline{e}^d) = \frac{K\theta^2}{2} + \frac{15\mu}{2q}(\underline{\omega e}^d) \bullet \underline{e}^d \tag{63}$$

where K and μ are respectively the bulk modulus and shear modulus of material, θ is the volume dilatation obtained from

$$\theta(\underline{e}) = \frac{3}{q}(\underline{\omega x}) \bullet \underline{e}, \tag{64}$$

where $\underline{x}$ is the bond length before deformation, m is the weighted volume defined by

$$q = (\underline{\omega x}) \bullet \underline{x}, \tag{65}$$

and $\underline{\omega}$ is the influence function which depends only on $|\boldsymbol{\xi}|$, $\underline{\omega} = 1$ for an unbroken bond and $\underline{\omega} = 0$ for a broken bond. The extension scalar state $\underline{e}$ measures the change in the bond length due to deformation

$$\underline{e} = \underline{y} - \underline{x}, \qquad \underline{y} = |\mathbf{y}|, \qquad \underline{x} = |\boldsymbol{\xi}|, \tag{66}$$

and $\underline{e}^d$ is the deviatoric part of $\underline{e}$

$$\underline{e}^d = \underline{e} - \frac{\theta \underline{x}}{3}, \tag{67}$$

Using equation 63 in equation 62 the magnitude of the force state vector acting along the deformed bond direction is

$$t = \frac{3K\theta}{q}\underline{\omega x} + \frac{15\mu}{q}\underline{\omega e}^d. \tag{68}$$

The "$\bullet$" acts on two scalar states is the integration of their regular product over the neighbor region. For example, for a point $\mathbf{x}$,

$$(\underline{\omega e}^d) \bullet \underline{e}^d = \int_H [\underline{\omega}(\mathbf{x}, \mathbf{x}') \cdot \underline{e}^d(\mathbf{x}, \mathbf{x}')] \cdot \underline{e}^d(\mathbf{x}, \mathbf{x}'). \tag{69}$$

6.2.1 Plane stress peridynamic

The volumn dilatation in a plane stress state is

$$\theta = \frac{2(2v-1)}{(v-1)} \frac{\underline{\omega r} \bullet \underline{e}}{q}, \tag{70}$$

and the force state is

$$\underline{t} = \frac{2(2\nu-1)}{(\nu-1)}\left(k'\theta - \frac{\beta}{3}(\underline{\omega e^d}) \bullet \underline{r}\right)\frac{\omega r}{q} + \beta\underline{\omega e^d}, \tag{71}$$

where

$$\beta = \frac{8\mu}{q}, \tag{72a}$$

$$k^{'} = k + \frac{\mu}{9}\frac{(v+1)^2}{(2v-1)^2} \tag{72b}$$

6.2.2 Numerical discretization

Numerical implementation of peridynamic continuum model requires the discretization of the domain. The most common discretization scheme employed in peridynamics is the meshfree method. Opposed to the finite element discretization, in meshefree method the domain is discretized by nodes instead of elements. In a meshfree discretization, nodes are not connected to each other by elements or any other geometrical constraints. The discretized form of the peridynamic equation of motion is

$$\rho(\mathbf{x}_I)\ddot{\mathbf{u}}(\mathbf{x}_I,t) = \sum_{J=1}^{K}(\underline{\mathbf{T}}[\mathbf{x}_I,t]\langle\mathbf{x}_J-\mathbf{x}_J\rangle - \underline{\mathbf{T}}[\mathbf{x}_J,t]\langle\mathbf{x}_I-\mathbf{x}_J\rangle)V_J + \mathbf{b}(\mathbf{x}_I,t), \quad \forall I = 1,2,...,N \tag{73}$$

where $\mathbf{x}_I$ denotes a peridynamic discrete node, $\mathbf{x}_J$ is a node within the horizon of $\mathbf{x}_I$, K is the total number of nodes within the horizon $\mathcal{H}$ of $\mathbf{x}_I$, V_J is the volume of $\mathbf{x}_J$ in the initial configuration and N is the total number of nodes in the peridynamic domain. The discretized equation of motion can be integrated in time using an explicit time integration scheme such as the velocity Verlet method.

Table 5: Material coefficients of MoS_2 for the peridynamics simulation.

Young's modulus	200 GPa
ν	0.29
ρ	5.06 g/cm^3
K_o	1.482 $MPa\sqrt{m}$

Table 6: Material coefficients of h-BN for the peridynamics simulation.

Young's modulus	925 GPa
ν	0.23
ρ	2.3 g/cm^3
K_o	5.4 $MPa\sqrt{m}$

6.2.3 Hamiltonian of peridynamics

The Hamiltonian of peridynamics is

$$H_p = W_p^{\text{kin}} + W_p^{\text{int}} - W_p^{\text{ext}}. \tag{74}$$

where the kinetic energy is given by

$$W_p^{\text{kin}} = \sum_I^N \frac{1}{2}\dot{\mathbf{d}}_I^T \rho \dot{\mathbf{d}}_I V_I = \sum_I^N \frac{\mathbf{P}_I^p \cdot \mathbf{P}_I^p}{2M_I^p} \tag{75}$$

The internal strain energy is given by

$$W_p^{\text{int}} = \sum_{I\in\mathcal{N}} V_I \psi_I^{PD} = \sum_{I\in\mathcal{N}} \mathbf{d}_I \cdot \left(\sum_{J=1}^K (\underline{\mathbf{T}}[\mathbf{x}_I, t]\langle \mathbf{x}_J - \mathbf{x}_J \rangle - \underline{\mathbf{T}}[\mathbf{x}_J, t]\langle \mathbf{x}_I - \mathbf{x}_J \rangle) V_J \right) V_I, \tag{76}$$

and the potential energy of the external forces is

$$W_p^{\text{ext}} = \sum_{I\in\mathcal{N}} \mathbf{d}_I \cdot \mathbf{b} V_I, \tag{77}$$

where $\dot{\mathbf{d}}_I$ is the velocity of node I.

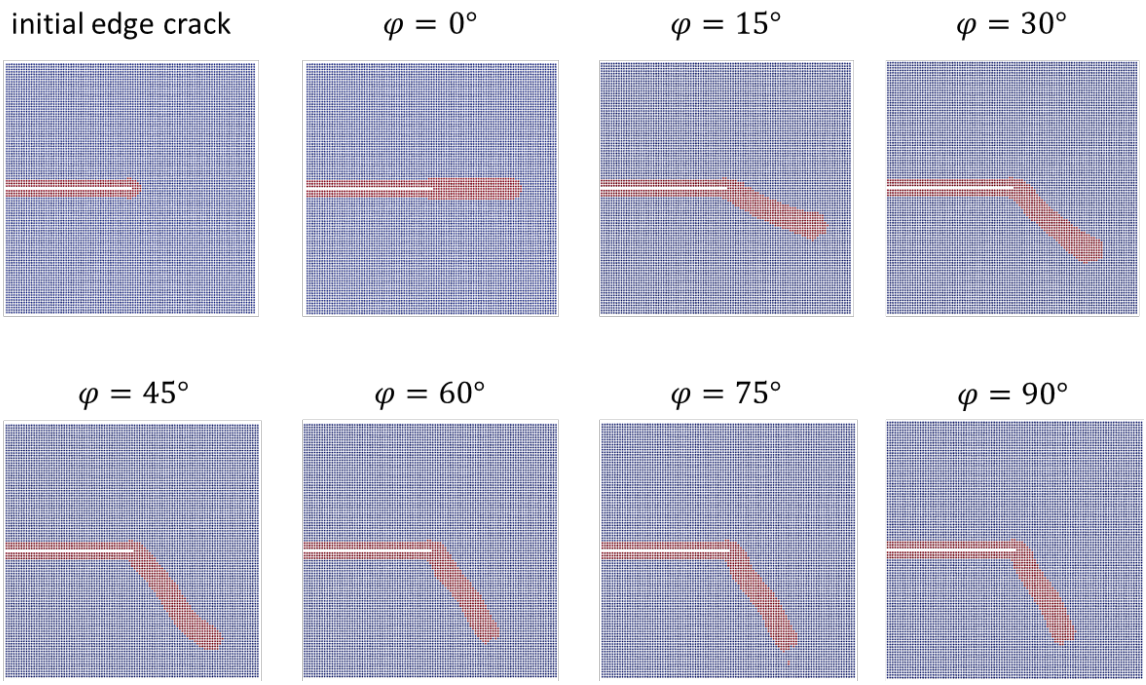

Figure 51: Crack path of MoS_2 under the mix-mode loadings.

6.3 The numerical simulations and results

We use peridynamics to model the fracture of 2D panels of MoS_2 and h-BN. Table 5 and 6 shows the materials coefficients which are used for the simulations. The configuration of the subject is shown as the figure 51. It is a 2D panel whose size is equaled to 50 cm×50 cm. An mix-mode loading follows the equation 3a in chapter 1 (with a loading rate of 0.5 cm/s), is applied on the boundary. The initial edge crack is on the left side of the panel and the crack tips are at the center of the panel. Initially, the edge crack is developed by deleting a row of points and cutting through all the interactions across the edge crack. To show the settling of the initial crack and the propagation progress of the crack, any point with a broken bond is marked in the red.

From figure 51 and figure 52, we can see that the crack propagates in the different

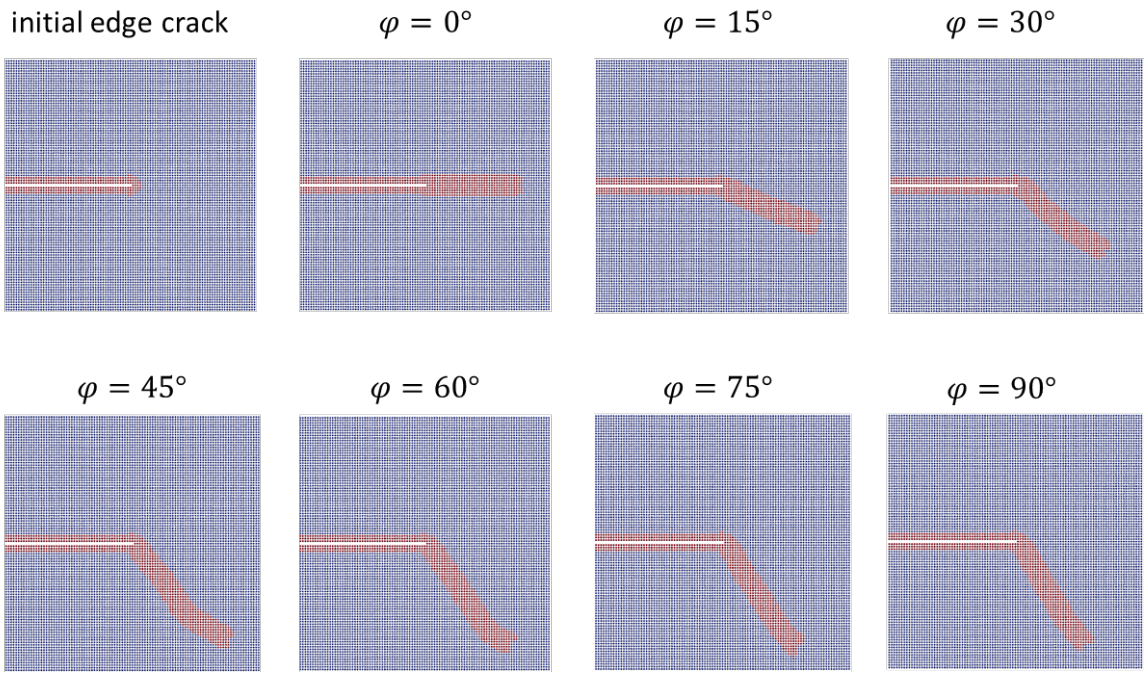

Figure 52: Crack path of h-BN under the mix-mode loadings.

directions according to the loading phase angles. Figure 53 shows a zoom in of a zone near the center of the panel. Even though the mesh is very regular, the cracks paths are not just straight lines, which means that the cracks propagation is not constraint by the mesh. Figure 54 shows the cracks kinking angle as a function of the loading phase angle. The curve based on the peridynamics simulation and the curve based on the maximum circumferential stress criterion match very well, especially when the loading phase angle is smaller than 50°. The results of MoS_2 and h-BN are very similar. Figure 54 represents the results for both MoS_2 and h-BN.

Note that in the previous molecular dynamics simulation, the kinking angle can only be multiples of the 30°. However here in the continuum level simulation, the kinking angle is changing smoothly according to the change of the loading phase angle.

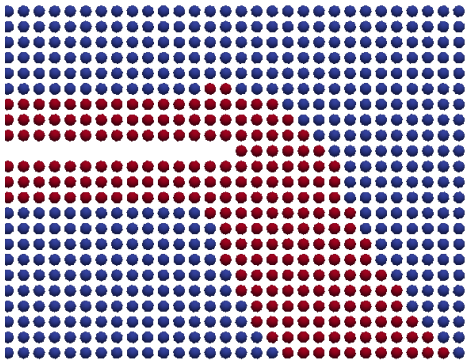

Figure 53: Zoom in of the domain near the kinking angle. Any point who has a broken bond is marked by the red color.

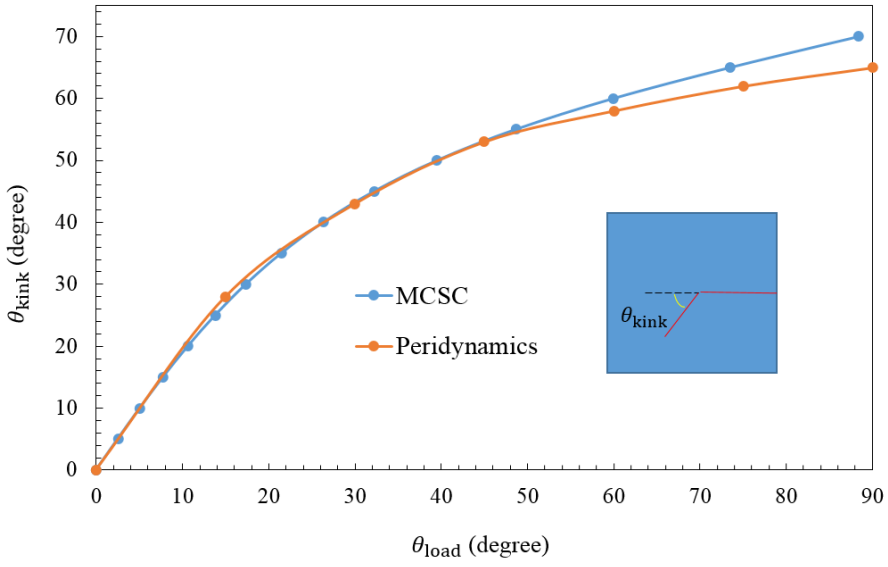

Figure 54: Kinking angle of MoS_2 as a function of the loading phase angle.

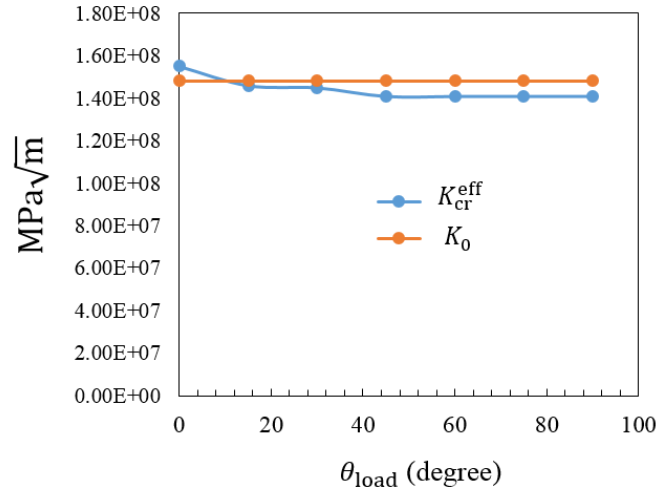

(a)

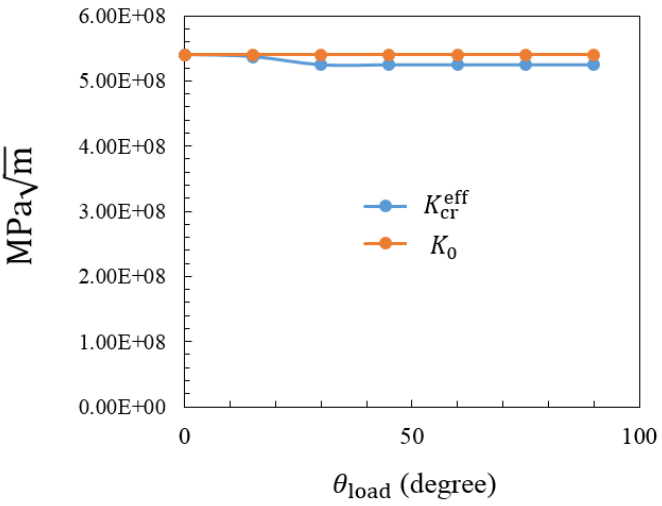

(b)

Figure 55: The effective critical stress intensity factor of (a) MoS_2 and (b) h-BN of each example. It matches the materials critical stress intensity factor, which is a material coefficient.

Figure 55 shows the effective critical stress intensity factor of MoS_2 and h-BN of each example. They are compared with the K_0, which is the critical stress intensity factor of the material. The critical stress intensity factor obtained from peridynamicsis matching the material critical stress intensity factor.

6.4 Conclusion

These examples show that,

(1) The peridynamics is able to represent the fracture phenomenon of the MoS_2 and h-BN materials from the continuum level. The cracks propagation path is not constrained by the mesh, thus it can accurately capture the cracks propagation process without remeshing. Before the simulation, the Youngs modulus, the Poissons ratio, the mass density, the critical stress intensity factor of the material are required. Especially the critical stress intensity factor is used as the criterion to determine if a pair of points still have the interaction. The new crack surfaces are naturally formed without any specific criterion to predict the cracks propagation direction.

(2) The fracture behavior of the MoS_2 and h-BN in the continuum level is similar. It is not influenced ty the atomic structure. Since the peridynamics is a continuum level method, it can not capture the size effect of the nano materials.

CHAPTER 7: THE COUPLING OF PERIDYNAMICS AND FINITE ELEMENT METHODS

7.1 Introduction

Although the peridynamic theory is capable of modeling damage formation and growth without resorting to any external criteria, numerical simulations using peridynamics are computationally expensive. The high computational cost is attributed to the nonlocality of the theory. In nonlocal theories each particle interacts with a large group of particles, resulting in costly assembly operations of the nonlocal discrete systems.

Another issue associated with peridynamics is the prescription of displacement and traction boundary conditions. Since the variation formulation of the peridynamics does not include tractions, the forces acting on the surface are prescribed as body forces acting within a fictitious boundary layer under the surface. Similar to tractions, displacements boundary conditions are imposed by constraining the displacement of material points within a fictitious boundary layer. A linear interpolation is used to approximate the value of the displacement of material points in the boundary layer based on the boundary conditions and the displacement of the points within the domain. The inaccuracy in prescribing the boundary conditions in peridynamics reduces the accuracy of modeling predictions.

In this chapter, we propose a technique for coupling peridynamics with finite el-

ements for dynamic fracture modeling. In our proposed coupling technique, peridynamics description is used only in the areas of the domain where nucleation or growth of discontinuities is probable, and finite elements are used elsewhere. Therefore, fine scale behavior is captured by the peridynamics zone and finite elements are used in the zones where solution is smooth. The proposed method takes advantages of the salient features of both techniques i.e. straight forward application of boundary conditions along with lower computational cost of finite elements and peridynamics superiority in fracture simulation.

The main challenge associated with developing coupled peridynamics–finite element methods is to minimize the fictitious interface effects. In static problems, special considerations need to be taken to remove ghost forces, while in dynamic problems, the spurious wave reflections at the interface of peridynamics and finite element domains must also be eliminated. The main source of wave reflections can be attributed to the change of constitutive behavior between an inherently nonlocal peridynamic domain and a local continuum domain, and the significant difference between the resolution of finite element mesh and the resolution of peridynamic zone. Since the minimum wave length which can be supported by FE is much larger than the minimum wave length which can be resolved by the peridynamic zone (PD), the FE/PD interface acts as a rigid boundary for those components of the wave which can not be resolved by the finite element mesh. So instead of passing smoothly into the finite element zone, the short wavelength (high frequency) components of the wave will reflect back into the PD domain. This will lead to spurious growth of the energy of the peridynamic domain, and will drastically reduce the computational accuracy.

Coupling between peridynamics and finite element has received attention recently. Erkan etl. studied a submodeling approach in which the boundary conditions of PD are imported from FEM [107]. However they assume that the submodeling details do not affect the FEM simulation and the boundary of the PD is far enough from the local features. Richard and Steward studied a way to implement the PD model in a conventional FEM code. To save the computational time, the displacement constraint between the FEM and PD is applied in a fuzzy zone [92]. Liu developed an interface element, in which the embedded points are firmly attached to the interface element, while the interaction force between the embedded points and the normal points are divided and assigned to the nodes of the interface elements [88]. Similar studies has been done by [41, 65, 115]. These coupling ideas are actually straightforwardly similar: in the overlapping zone of FEM and PD, part of the points are firmly attached on the mother element meanwhile part of the nodes are firmly attached to their surrounding points. The attaching criterion can be based on displacement or force. However, these rough ways of coupling are only tested under the linearly increased and quasi-static loadings. In a real-world example, for example, a bullet hitting a shield, or in an explosion, the loadings may be with a high rate and the increasing format can be more complex. In these cases, the coarsely meshed FEM can not represent the high frequency waves, which comes from the finely meshed PD. Thus the high frequency waves will be reflected back to the PD zone and the redundant energy is introduced and trapped inside the PD. The unexpected redundant energy does not only introduce the accumulated error, the earlier nucleated or propagated crack, it also may cause the failure near the coupling zone [135]. In this study, the PD is used to simulate the

part where fracture may occur and FEM is used to simulate the loading and boundary condition. The purpose is to discover the possibility and methodology of the coupling of FEM and PD seamlessly and smoothly. Not only the load can be transferred from FEM, the FEM should also feel the feedback from PD simultaneously. The loading is able to be a high rate dynamic loading. The mesh of the PD and the overlapping can be generated easily without much artificial effort. At the end, the PD can be inserted to a FEM software to simulate pragmatic real world problems by a general backgrounded user.

In developing our coupling techniques we aim at satisfying the following two main criteria:

1. The peridynamic zone should be properly glued to the finite element subdomain such that a smooth enough wave can travel between subdomains without getting distorted at the interface.

2. Spurious wave reflections should be eliminated. For this purpose, the high frequency waves (fine scale oscillations) which cannot travel into the finite element zone should be appropriately damped.

In this chapters, we propose a concurrent coupling technique in the framework of Arlequin approach [13, 32], which uses Lagrange multipliers to glue two disparate subdomains. The Arlequin approach has been used previously for coupling atomistic zone to finite element zone [153, 112, 164, 121, 135]. In this paper, we use this approach to couple two continuum zones to each other. To simplify the formulations, we present the coupling for linear elastic materials, however the proposed method is

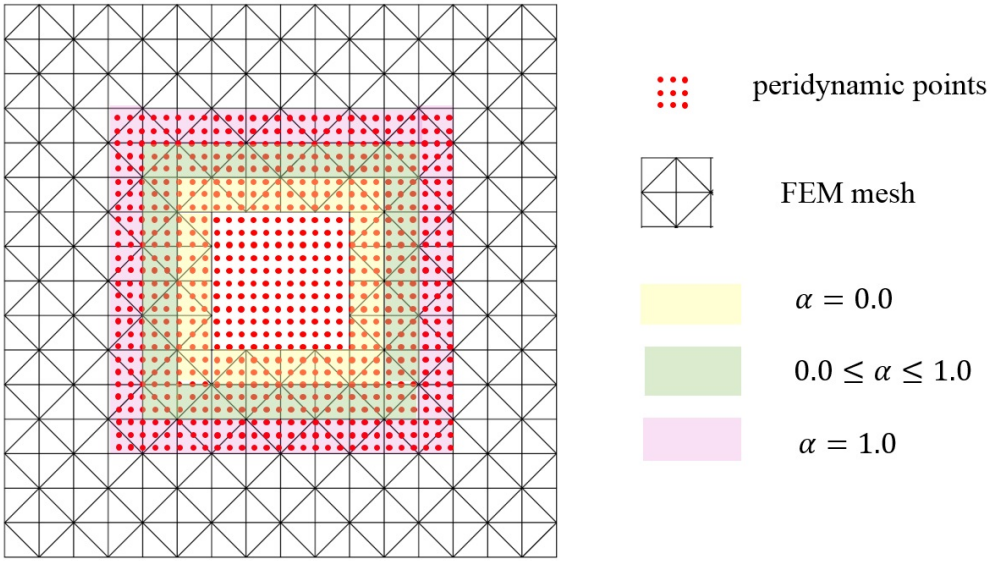

Figure 56: The overlapping zone required by EBDM.

generic and is not restricted to linear elastic materials.

7.2 Formulation of the Arlequin method

In this section we describe a method based on the Arlequin framework for coupling finite elements with peridynamics. Following the Arlequin approach, the domain is subdivided into three subdomains: a pure peridynamics (or molecular dynamics) zone, a pure finite element zone (classical continuum zone) and an overlapping zone. The domain decomposition is shown in figure 56. To reduce the computational costs, the peridynamics is used only around cracks and finite elements is used elsewhere.

In the Arlequin method the energy of the system is obtained as a linear combination of the energy from both models, i.e peridynamic (or molecular dynamics) elasticity and classical elasticity

$$\begin{aligned} H(\mathbf{u}, \dot{\mathbf{u}}) &= H_c(\mathbf{u}, \dot{\mathbf{u}}) + H_p(\mathbf{d}, \dot{\mathbf{d}}) \\ &= \alpha(\mathbf{x}) \left(W_c^{\text{kin}} + W_c^{\text{int}} - W_c^{\text{ext}} \right) + (1 - \alpha(\mathbf{x})) \left(W_p^{\text{kin}} + W_p^{\text{int}} - W_p^{\text{ext}} \right), \end{aligned} \tag{78}$$

where $\mathbf{u}$ denotes the displacement field of the finite element zone and $\mathbf{d}$ represents the displacement field of the peridynamics (or molecular dynamics) zone. The weighting coefficients α should be chosen such that

$$\alpha(\mathbf{x}) = \begin{cases} 1 & \forall \mathbf{x} \in \Omega_c \backslash \Omega_o \\ 0 & \forall \mathbf{x} \in \Omega_d \backslash \Omega_o \end{cases} \tag{79}$$

The simplest form of coefficient α which satisfies the criteria of equation 79 is a piecewise linear function

$$\alpha(\mathbf{x}) = \frac{l_1}{l_1 + l_2} \quad \forall \mathbf{x} \in \Omega_o \tag{80}$$

where l_1 and l_2 are respectively the distance from point $\mathbf{x}$ to the nearest points with $\alpha = 0$ and $\alpha = 1$. The variation of coefficient α over the domain is schematically shown in figure 56.

The mechanical compatibility between the peridynamics and finite element zones requires that the classical continuum displacement $\mathbf{u(x)}$ be conforming with the peridynamics displacement field $\mathbf{d(x)}$ on the overlapping zone. The conformity between the displacements can be satisfied by defining constraints on the two displacement fields. Different form of constraints can be considered. For example, the following constraint requires that the displacement of peridynamic (or molecular dynamics) points should be equal to the displacement of finite elements at the location of peridynamics nodes

$$\mathbf{g}_I = \mathbf{u}(\mathbf{x}_I) - \mathbf{d}_I = \sum_{J \in \mathcal{S}} N_J(\mathbf{x}_I)\mathbf{u}_J - \mathbf{d}_I = 0, \quad \forall I \in \mathcal{M}_p, \quad i = 1, 2, 3 \tag{81}$$

where $\mathbf{g}_I = \{g_{1I}, g_{2I}, g_{2I}\}$ is the set of constraints imposed on displacement of point I,

$\mathcal{M}_p$ is the set of all the peridynamic (or molecular dynamics) points in the overlapping zone and $\mathcal{S}$ is the set of all the finite element nodes whose support intersects the overlapping zone.

This constraint in applied using Lagrange multipliers. For this purpose, the total Hamiltonian of the system is modified to

$$H_L(\mathbf{u}, \mathbf{d}, \boldsymbol{\lambda}) = \alpha(\mathbf{x}) H_c(\mathbf{u}) + (1 - \alpha(\mathbf{x})) H_p(\mathbf{d}) + \sum_{I \in \mathcal{M}_p} \boldsymbol{\lambda}_I \cdot \mathbf{g}_I, \tag{82}$$

where $\boldsymbol{\lambda}_I^T = \{\lambda_{1I}, \lambda_{2I}, \lambda_{2I}\}$ is the Lagrange multipliers at peridynamic (or molecular dynamics) point I. Lagrange multipliers are approximated using a λ–mesh which is constructed over the overlapping zone

$$\boldsymbol{\lambda_I}(\mathbf{x}) = \sum_{J \in \mathcal{Q}} N_J^{\lambda}(\mathbf{x}_I) \overline{\boldsymbol{\lambda}}_J, \tag{83}$$

where N_J^{λ} is the shape function of node J of the Lagrange multiplier filed, $\mathcal{Q}$ is the set of Lagrange multiplier nodes and $\overline{\boldsymbol{\lambda}}_J$ is the value of Lagrange multiplier at λ–node J. Using equation 81 and equation 83 in equation 82 we obtain

$$H_L(\mathbf{u}, \mathbf{d}, \boldsymbol{\lambda}) = \alpha(\mathbf{x}) H_c(\mathbf{u}) + (1 - \alpha(\mathbf{x})) H_p(\mathbf{d}) + \sum_{I \in \mathcal{M}_p} \sum_{K \in \mathcal{Q}} N_K^{\lambda}(\mathbf{x}_I) \overline{\boldsymbol{\lambda}}_K \cdot \left(\sum_{J \in \mathcal{S}} N_J(\mathbf{x}_I) \mathbf{u}_J - \mathbf{d}_I \right), \tag{84}$$

A Lagrange multiplier mesh along with the finite element mesh and peridynamic (or molecular dynamics) grid is shown in figure 57. Any mesh which satisfies the Ladyzhenskaya-Babuska-Brezzi (LBB) condition can be used to construct Lagrange multipliers shape functions. We consider two types of λ–mesh. A λ–mesh whose

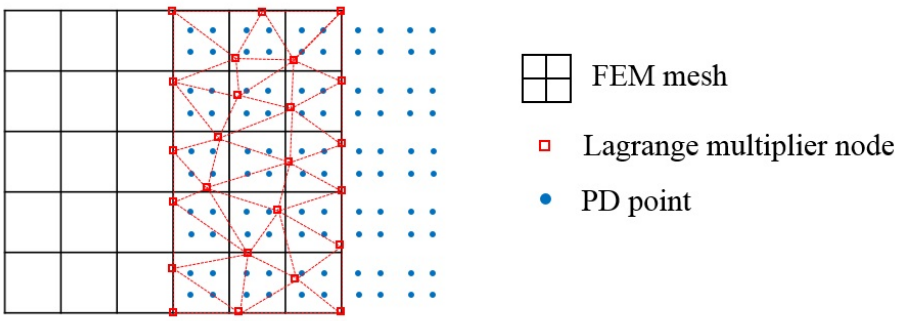

Figure 57: Lagrange multiplier interpolation.

nodes coincides with the finite element nodes, i.e $N_J^\lambda(\mathbf{x}_I) = N_J(\mathbf{x}_I)$, and a λ–mesh whose nodes coincide with the peridynamic nodes, i.e $N_J^\lambda(\mathbf{x}_I) = \delta_{IJ}$ where δ_{IJ} is the Kronecker delta. We refer to the former method as weak BDM; we call the second method as the strict BDM.

7.2.1 Equations of motion

The Hamiltonian of the FEM domain is

$$\alpha(\mathbf{x})H_c(\mathbf{u}) = \alpha(\mathbf{x})W_c^{\text{kin}} + \alpha(\mathbf{x})W_c^{\text{int}} - \alpha(\mathbf{x})W_c^{\text{ext}} \tag{85a}$$

$$\alpha(\mathbf{x})W_c^{\text{kin}} = \sum_{I\in\mathcal{M}} \alpha_I \frac{\mathbf{P}_I^c \cdot \mathbf{P}_I^c}{2M_I^c} \tag{85b}$$

$$\alpha(\mathbf{x})W_c^{\text{int}} = \int_{\Omega_c} \alpha(\mathbf{x})\psi_c d\Omega = \sum_{I\in\mathcal{M}} \left(\bar{\mathbf{f}}_I^{\text{int}}\right)_c \cdot \mathbf{u}_I \tag{85c}$$

$$\alpha(\mathbf{x})W_c^{\text{ext}} = \int_{\Omega_c} \alpha(\mathbf{x})\mathbf{u}^T\mathbf{b}d\Omega + \int_{\Gamma_t} \alpha(\mathbf{x})\mathbf{u}^T\mathbf{t}d\Gamma = \sum_{I\in\mathcal{M}} \left(\bar{\mathbf{f}}_I^{\text{ext}}\right)_c \cdot \mathbf{u}_I \tag{85d}$$

where $\alpha_I = \alpha(\mathbf{x}_I)$ and the internal and external forces are

$$\left(\bar{\mathbf{f}}_I^{\text{int}}\right)_c = \int_{\Omega_c} \alpha(\mathbf{x}) \frac{\partial N_I}{\partial x_j} \sigma_{ji} d\Omega \tag{86a}$$

$$\left(\bar{\mathbf{f}}_I^{\text{ext}}\right)_c = \int_{\Omega_c} \alpha(\mathbf{x}) N_I \rho \mathbf{b} d\Omega + \int_{\Gamma_t} \alpha(\mathbf{x}) N_I \mathbf{t} d\Gamma \tag{86b}$$

Similarly, by using equations 74–77 we obtain

$$(1-\alpha(\mathbf{x}))H_c(\mathbf{u}) = (1-\alpha(\mathbf{x}))W_p^{\text{kin}} + (1-\alpha(\mathbf{x}))W_p^{\text{int}} - (1-\alpha(\mathbf{x}))W_p^{\text{ext}} \tag{87a}$$

$$(1-\alpha(\mathbf{x}))W_p^{\text{kin}} = \sum_{I\in\mathcal{N}}(1-\alpha_I)\frac{\mathbf{P}_I^p\cdot\mathbf{P}_I^p}{2M_I^p} \tag{87b}$$

$$(1-\alpha(\mathbf{x}))W_p^{\text{int}} = \sum_{I\in\mathcal{N}}(1-\alpha_I)\psi_I^{PD}V_I = \sum_{I\in\mathcal{N}}\left(\mathbf{f}_I^{\text{int}}\right)_p\cdot\mathbf{d}_I \tag{87c}$$

$$(1-\alpha(\mathbf{x}))W_p^{\text{ext}} = \sum_{I\in\mathcal{N}}(1-\alpha_I)\mathbf{d}_I\cdot\mathbf{b}V_I = \sum_{I\in\mathcal{N}}\left(\mathbf{f}_I^{\text{ext}}\right)_p\cdot\mathbf{d}_I \tag{87d}$$

where $\left(\mathbf{f}_I^{\text{int}}\right)_p$ and $\left(\mathbf{f}_I^{\text{ext}}\right)_p$ are given by

$$\left(\mathbf{f}_I^{\text{int}}\right)_p = (1-\alpha_I)\left(\sum_{J=1}^{K}(\underline{\mathbf{T}}[\mathbf{x}_I,t]\,\langle\mathbf{x}_J-\mathbf{x}_J\rangle - \underline{\mathbf{T}}[\mathbf{x}_J,t]\langle\mathbf{x}_I-\mathbf{x}_J\rangle)V_J\right)V_I, \tag{88a}$$

$$\left(\mathbf{f}_I^{\text{ext}}\right)_p = (1-\alpha_I)\mathbf{b}V_I. \tag{88b}$$

The equations of motion can be uniquely defined by Hamilton's equations

$$\alpha_I\dot{\mathbf{P}}_I^c = -\frac{\partial H_L}{\partial\mathbf{u}_I} = \frac{\partial\left(\alpha(\mathbf{x})W_c^{\text{ext}}\right)}{\partial\mathbf{u}_I} - \frac{\partial\left(\alpha(\mathbf{x})W_c^{\text{int}}\right)}{\partial\mathbf{u}_I} - \sum_{J\in\mathcal{Q}}\mathbf{G}_{IK}\overline{\boldsymbol{\lambda}}_K \tag{89a}$$

$$\alpha_I\dot{\mathbf{u}}_I = \frac{\partial H_L}{\partial\mathbf{P}_I^c} = \alpha_I\frac{\partial H_c}{\partial\mathbf{P}_I^c} = \alpha_I\frac{\mathbf{P}_I^c}{M_I^c} \tag{89b}$$

$$(1-\alpha_I)\dot{\mathbf{P}}_I^p = -\frac{\partial H_L}{\partial\mathbf{d}_I} = \frac{\partial\left((1-\alpha_I)W_p^{\text{ext}}\right)}{\partial\mathbf{d}_I} - \frac{\partial\left((1-\alpha_I)W_p^{\text{int}}\right)}{\partial\mathbf{d}_I} + \sum_{I\in\mathcal{M}_p}\sum_{K\in\mathcal{Q}}N_k^{\lambda}(\mathbf{x}_I)\overline{\boldsymbol{\lambda}}_K \tag{89c}$$

$$(1-\alpha_I)\dot{\mathbf{d}}_I = \frac{\partial H_L}{\partial\mathbf{P}_I^p} = (1-\alpha_I)\frac{\partial H_p}{\partial\mathbf{P}_I^p} = (1-\alpha_I)\frac{\mathbf{P}_I^p}{M_I^p} \tag{89d}$$

where

$$\mathbf{G}_{IK} = \sum_{J\in\mathcal{M}_p}N_K^{\lambda}(\mathbf{x}_J)N_I(\mathbf{x}_J) \tag{90}$$

Combining equations 89a and 89b and using equations 85c and 85d we obtain

$$\alpha_I M_I^c \ddot{\mathbf{u}}_I = \left(\overline{\mathbf{f}}_I^{\text{ext}}\right)_c - \left(\overline{\mathbf{f}}_I^{\text{int}}\right)_c - \sum_{K\in\mathcal{Q}} \mathbf{G}_{IK}\overline{\boldsymbol{\lambda}}_K \tag{91}$$

Similarly, combining Equations 89c and 89d and using Equations 87c and 87d we obtain

$$(1-\alpha_I) M_I^p \ddot{\mathbf{d}}_I = \left(\overline{\mathbf{f}}_I^{\text{ext}}\right)_p - \left(\overline{\mathbf{f}}_I^{\text{int}}\right)_p + \sum_{K\in\mathcal{Q}} N_k^{\lambda}(\mathbf{x}_I)\overline{\boldsymbol{\lambda}}_K. \tag{92}$$

Equations 91 and 92 provide the complete equations of motion for finite elements and peridynamic (or molecular dynamics) points.

7.2.2 Explicit time integration

The time integration is conducted using the velocity Verlet algorithm. Since the value of Lagrange multipliers at the beginning of each time step is not known we use a prediction–correction method similar to that proposed in [152] to update the nodal displacements and velocities. In this algorithm the displacements at step $n+1$ obtained using the displacement, velocity and acceleration of step n by

$$\mathbf{u}_I^{n+1} = \mathbf{u}_I^n + \dot{\mathbf{u}}_I^n \Delta t + \frac{1}{2}\ddot{\mathbf{u}}_I^n \Delta t^2 \quad \forall I \in \mathcal{M} \tag{93a}$$

$$\mathbf{d}_I^{n+1} = \mathbf{d}_I^n + \dot{\mathbf{d}}_I^n \Delta t + \frac{1}{2}\ddot{\mathbf{d}}_I^n \Delta t^2 \quad \forall I \in \mathcal{N} \tag{93b}$$

The half step velocities are calculated using

$$\dot{\mathbf{u}}_I^{n+\frac{1}{2}} = \dot{\mathbf{u}}_I^n + \frac{\Delta t}{2}\ddot{\mathbf{u}}_I^n \quad \forall I \in \mathcal{M}, \tag{94a}$$

$$\dot{\mathbf{d}}_I^{n+\frac{1}{2}} = \dot{\mathbf{d}}_I^n + \frac{\Delta t}{2}\ddot{\mathbf{d}}_I^n \quad \forall I \in \mathcal{N}. \tag{94b}$$

The trial accelerations at step $n+1$ are calculated by ignoring the force due to the Lagrange multipliers

$$\ddot{\mathbf{u}}_I^{*n+1} = \frac{1}{\alpha M_I^c}\left[\left(\mathbf{f}_I^{\text{ext}}\right)_c^{n+1} - \left(\mathbf{f}I^{\text{int}}\right)_I^{n+1}\right] \quad \forall I \in \mathcal{M} \tag{95a}$$

$$\ddot{\mathbf{d}}_I^{*n+1} = \frac{1}{\alpha M_I^p}\left[\left(\mathbf{f}_I^{\text{ext}}\right)_c^{n+1} - \left(\mathbf{f}_c^{\text{int}}\right)_c^{n+1}\right] \quad \forall I \in \mathcal{N}. \tag{95b}$$

The trial velocities at step $n+1$ are obtained from

$$\dot{\mathbf{u}}_{n+1}^{*I} = \dot{\mathbf{u}}_I^{n+\frac{1}{2}} + \frac{\Delta t}{2}\ddot{\mathbf{u}}_I^{*n+1} \quad \forall I \in \mathcal{M}, \tag{96a}$$

$$\dot{\mathbf{d}}_{n+1}^{*I} = \dot{\mathbf{d}}_I^{n+\frac{1}{2}} + \frac{\Delta t}{2}\ddot{\mathbf{d}}_I^{*n+1} \quad \forall I \in \mathcal{N}. \tag{96b}$$

The trial constraint is obtained by substituting the trial velocities in the time derivative of constraint equation 81

$$\dot{\mathbf{g}}_I^{*n+1} = \dot{\mathbf{u}}(\mathbf{x}_I)^{*n+1} - \dot{\mathbf{d}}_I^{*n+1} = \sum_{J\in\mathcal{S}} N_J(\mathbf{x}_I)\dot{\mathbf{u}}_J^{*n+1} - \dot{\mathbf{d}}_I^{*n+1} \quad \forall I \in \mathcal{M}_p, \tag{97}$$

The correct velocities are obtained by considering the Lagrange multipliers force in the calculation of accelerations

$$\begin{aligned}\dot{\mathbf{u}}_I^{n+1} &= \dot{\mathbf{u}}_I^n + \frac{\Delta t}{2}\left[\ddot{\mathbf{u}}_I^n - \frac{1}{\alpha_I M_I^c}\sum_{K\in\mathcal{Q}}\mathbf{G}_{IK}\overline{\boldsymbol{\lambda}}_K^n + \ddot{\mathbf{u}}_I^{n+1} - \frac{1}{\alpha_I M_I^c}\sum_{K\in\mathcal{Q}}\mathbf{G}_{IK}\overline{\boldsymbol{\lambda}}_K^{n+1}\right] \\ &= \dot{\mathbf{u}}_I^{*n+1} - \frac{\Delta t}{\alpha_I M_I^c}\sum_{K\in\mathcal{Q}}\mathbf{G}_{IK}\overline{\boldsymbol{\lambda}}_K^{n+\frac{1}{2}}\end{aligned} \tag{98a}$$

$$\begin{aligned}\dot{\mathbf{d}}_I^{n+1} = \dot{\mathbf{d}}_I^n + \frac{\Delta t}{2}\Bigg[&\ddot{\mathbf{d}}_I^n + \frac{1}{(1-\alpha_I)M_I^c}\sum_{K\in\mathcal{Q}}N_k^\lambda(\mathbf{x}_I)\overline{\boldsymbol{\lambda}}_K^n + \ddot{\mathbf{d}}_I^{n+1} + \\ &\frac{1}{(1-\alpha_I)M_I^c}\sum_{K\in\mathcal{Q}}N_k^\lambda(\mathbf{x}_I)\overline{\boldsymbol{\lambda}}_K^{n+1}\Bigg] = \dot{\mathbf{d}}_I^{*n+1} + \frac{\Delta t}{(1-\alpha_I)M_I^p}\sum_{K\in\mathcal{Q}}N_k^\lambda(\mathbf{x}_I)\overline{\boldsymbol{\lambda}}_K^{n+\frac{1}{2}}\end{aligned} \tag{98b}$$

Figure 58: The displacement of PD is discomposed into a fine and a coarse part.

where $\overline{\boldsymbol{\lambda}}_K^{n+\frac{1}{2}} = \frac{1}{2}\left(\overline{\boldsymbol{\lambda}}_K^n + \overline{\boldsymbol{\lambda}}_K^{n+1}\right)$. By using equation 98 in the time derivative form of equation 81 we obtain

$$\begin{aligned}\dot{\mathbf{g}}_I^{n+1} = \dot{\mathbf{u}}(\mathbf{x_I})^{n+1} - \dot{\mathbf{d}}_I^{n+1} = \dot{\mathbf{g}}_I^{*n+1} - \frac{\Delta t}{\alpha_I M_I^c}\sum_{J\in\mathcal{S}} N_J(\mathbf{x}_I)\sum_{K\in\mathcal{Q}}\mathbf{G}_{JK}\overline{\boldsymbol{\lambda}}_K^{n+\frac{1}{2}} \\ + \frac{\Delta t}{(1-\alpha_I)M_I^p}\sum_{K\in\mathcal{Q}} N_K^{\lambda}(\mathbf{x}_I)\overline{\boldsymbol{\lambda}}_K^{n+\frac{1}{2}}\end{aligned} \tag{99}$$

which can be simplified as

$$\sum \mathbf{A}_{IK}\boldsymbol{\lambda}_K = \dot{\mathbf{g}}_I^{*n+1}, \tag{100}$$

where

$$\mathbf{A}_{IK} = \frac{\Delta t}{\alpha_I M_I^c}\sum_{J\in\mathcal{S}} N_J(\mathbf{x}_I)\mathbf{G}_{JK} - \frac{\Delta t}{(1-\alpha_I)M_I^p}N_K^{\lambda}(\mathbf{x}_I)\mathbf{I}, \tag{101}$$

where I is the identity matrix.

To save in the computational costs, matrix $\mathbf{A}$ is diagonalized by

$$\mathbf{A}_{II} = \sum_{K\in\mathcal{Q}}\left[\frac{\Delta t}{\alpha_I M_I^c}\sum_{J\in\mathcal{S}} N_J(\mathbf{x}_I)\mathbf{G}_{JK} - \frac{\Delta t}{(1-\alpha_I)M_I^p}N_K^{\lambda}(\mathbf{x}_I)\right] \tag{102}$$

The Lagrange multiplier of each λ-node is obtained from

$$\boldsymbol{\lambda}_K = \mathbf{A}_{II}^{-1}\dot{\mathbf{g}}_I^{*n+1}. \tag{103}$$

7.3 Removing the spurious reflections

The method presented in section 7.2 provides mechanical coupling between the classical elasticity and peridynamics zones and significantly reduces the spurious wave reflections if the overlapping size is reasonably large. In this section, we improve the efficiency of the method in removing the spurious wave reflections by adding a damping term to the equations of motion of the fine scale oscillations. For this purpose, we decompose the oscillations of the damping nodes into fine and coarse oscillations as shown in figure 58. The decomposition can be written as

$$\mathbf{d}_I = \mathbf{d}_I^{\text{coarse}} + \mathbf{d}_I^{\text{fine}}. \tag{104}$$

It is assumed that the fine scale oscillations can not transmit into the finite element zone and reflect back if they are not appropriately damped. We assume that the coarse scale displacement of each peridynamic node is equal to the displacement of the classical elasticity subdomain at the location of the peridynamic node. Using the finite element shape functions the coarse scale displacements can be approximated as

$$\mathbf{d}_I^{\text{coarse}} = \sum_{J \in \mathcal{S}} N_J(\mathbf{x}_I)\mathbf{u}_J. \tag{105}$$

By combining equation 105 and equation 104 the fine scale displacements are

$$\mathbf{d}_I^{\text{fine}} = \mathbf{d}_I - \sum_{J \in \mathcal{S}} N_J(\mathbf{x}_I)\mathbf{u}_J, \tag{106}$$

and subsequently the fine scale oscillations are

$$\ddot{\mathbf{d}}_I^{\text{fine}} = \ddot{\mathbf{d}}_I - \sum_{J \in \mathcal{S}} N_J(\mathbf{x}_I)\ddot{\mathbf{u}}_J. \tag{107}$$

By multiplying both sides of 107 with $\alpha_I M_I^p$ and using Equations 91 and 92 we obtain

$$(1-\alpha_I) M_I^p \ddot{\mathbf{d}}_I^{\text{fine}} = \mathbf{f}_I^{\text{fine}}, \tag{108}$$

where $\mathbf{f}_I^{\text{fine}}$ is

$$\begin{aligned} \mathbf{f}_I^{\text{fine}} = & \left(\mathbf{f}_I^{\text{ext}}\right)_p - \left(\mathbf{f}_I^{\text{int}}\right)_p + \sum_{K\in\mathcal{Q}} N_K^{\lambda}(\mathbf{x}_I)\overline{\boldsymbol{\lambda}}_K \\ & - \sum_{J\in\mathcal{S}} (1-\alpha_I) M_I^p N_J(\mathbf{x}_I) \frac{\left(\mathbf{f}_J^{\text{ext}}\right)_c - \left(\mathbf{f}_J^{\text{int}}\right)_c - \sum_{K\in\mathcal{Q}} \mathbf{G}_{IK}\overline{\boldsymbol{\lambda}}_K}{\alpha_I M_J^c}. \end{aligned} \tag{109}$$

Since the fine scale oscillations cannot be transferred into the finite element zone, we damp the fine scale oscillations by modifying the equation of motion (equation 108) to include a viscous damping term as

$$(1-\alpha_I) M_I^p \ddot{\mathbf{d}}_I^{\text{fine}} = \mathbf{f}_I^{\text{fine}} - (1-\alpha_I) M_I^p C_I \dot{\mathbf{d}}_I^{\text{fine}}, \tag{110}$$

where $\dot{\mathbf{d}}_I^{\text{fine}}$ is the velocity of fine scale oscillations obtained from

$$\dot{\mathbf{d}}_I^{\text{fine}} = \dot{\mathbf{d}}_I - \sum_{J\in\mathcal{S}} N_J(\mathbf{x}_I)\dot{\mathbf{u}}_J, \tag{111}$$

and C_I is the damping coefficient. The choice of damping coefficient can affect the success of the method in eliminating spurious reflections. In this paper, we approximate the damping function using the following parabolic equation

$$C_I = \overline{C}\frac{c}{L_1 + L_2}(1-\alpha_I)^2 \tag{112}$$

The velocity Verlet algorithm is used to integrate the fine scale equation of motion

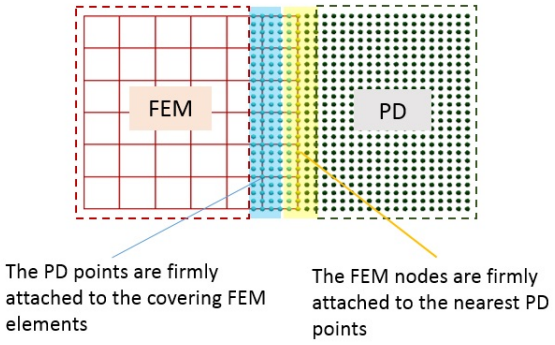

Figure 59: Schematic mechanisms of a bad connection. It only has the FEM dominate zone and peridynamics dominate zone without an interaction zone. It causes the spurious reflection problem.

(equation 108) in time.

$$\left(\mathbf{d}_I^{n+1}\right)^{\text{fine}} = \left(\mathbf{d}_I^{n}\right)^{\text{fine}} + \Delta t \left(\dot{\mathbf{d}}_I^{n}\right)^{\text{fine}} + \frac{1}{2}\Delta t^2 \left(\ddot{\mathbf{d}}_I^{n}\right)^{\text{fine}}, \tag{113a}$$

$$\left(\dot{\mathbf{d}}_I^{n+\frac{1}{2}}\right)^{\text{fine}} = \left(\dot{\mathbf{d}}_I^{n}\right)^{\text{fine}} + \frac{1}{2}\Delta t \left(\ddot{\mathbf{d}}_I^{n}\right)^{\text{fine}}, \tag{113b}$$

$$\left(\ddot{\mathbf{d}}_I^{n+1}\right)^{\text{fine}} = \frac{1}{(1-\alpha_I)M_I^p}\left(\mathbf{f}_I^{n+1}\right)^{\text{fine}} - C_I \left(\dot{\mathbf{d}}_I^{n+\frac{1}{2}}\right)^{\text{fine}}, \tag{113c}$$

$$\left(\dot{\mathbf{d}}_I^{n+1}\right)^{\text{fine}} = \left(\dot{\mathbf{d}}_I^{n+\frac{1}{2}}\right)^{\text{fine}} + \frac{1}{2}\Delta t \left(\ddot{\mathbf{d}}_I^{n+1}\right)^{\text{fine}}. \tag{113d}$$

7.4 2D examples —spurious reflection problem

In this section, we compare three ways of the coupling of peridynamics and FEM. The first one is a bad connection, in which the overlapping zone is simply divided into two parts. In one part, the nodes are firmly attached to their neighbor points, while in the other part, the points are firmly attached to its covering element as shown in figure 59. Currently, many studies couple FEM and peridynamics in similar ways. We will show that this coupling technique may introduce spurious reflection.

The second way of coupling is to use strict BDM. In this method, the Lagrange multipliers are solved for each point, and the constraint from the FEM to the peri-

Table 7: Material coefficients for the 2D examples, they represent the Al.

Young's Modulus	69 GPa
Poisson's ratio	0.3
mass density	2700 kg/m^3

dynamics reaches the maximum state. We will show that this excessive constraint also may introduce the spurious reflection problem. The third way of coupling is to use the weak BDM, in which the Lagrange multipliers are for each node, thus the constraint from the FEM to the peridynamics is minimized. This is the recommended way of the coupling in this study.

The coupling configuration is shown in figure 60, where the length and width of the panel are $L_1 = 400$ cm, $L_2 = 220$ cm and $W = 8$ cm. Peridynamics is used at the center part and FEM is used at the left and right parts. The mesh sizes of FEM and peridynamics are about 2 cm and 0.25 cm respectively. The material properties are provided in table 7, which represents aluminum.

In these examples, a combination of fine and coarse waves are initialized in the center of a 2D ribbon as described in equation 114 (see figure 61(a)). where $a_1 = 0.0003$, $a_2 = 0.3$, $w_1 = 48$, $w_2 = 3$.

$$d_x|_{t=0} = \begin{cases} a_1 + \left(\cos\frac{2\pi|x|}{w_1} + 1\right) + \left[1 + a_2\cos\frac{2\pi}{w_2(x+0.5w_1)}\right] & (-0.5w_1 \leq x \leq 0.5w_1) \\ 0 & (x < -0.5w_1 \; or \; x > 0.5w_1) \end{cases} \tag{114}$$

We firstly run a pure peridynamics example as a reference. As expected, the waves split into two groups and propagate to the left and right (see figure 61(b)).

We test the examples in two step times: $\Delta t = 10^{-7}$ s and $\Delta t = 10^{-8}$ s. From figure 61 we can see that, the "bad connection" causes spurious reflection of the high

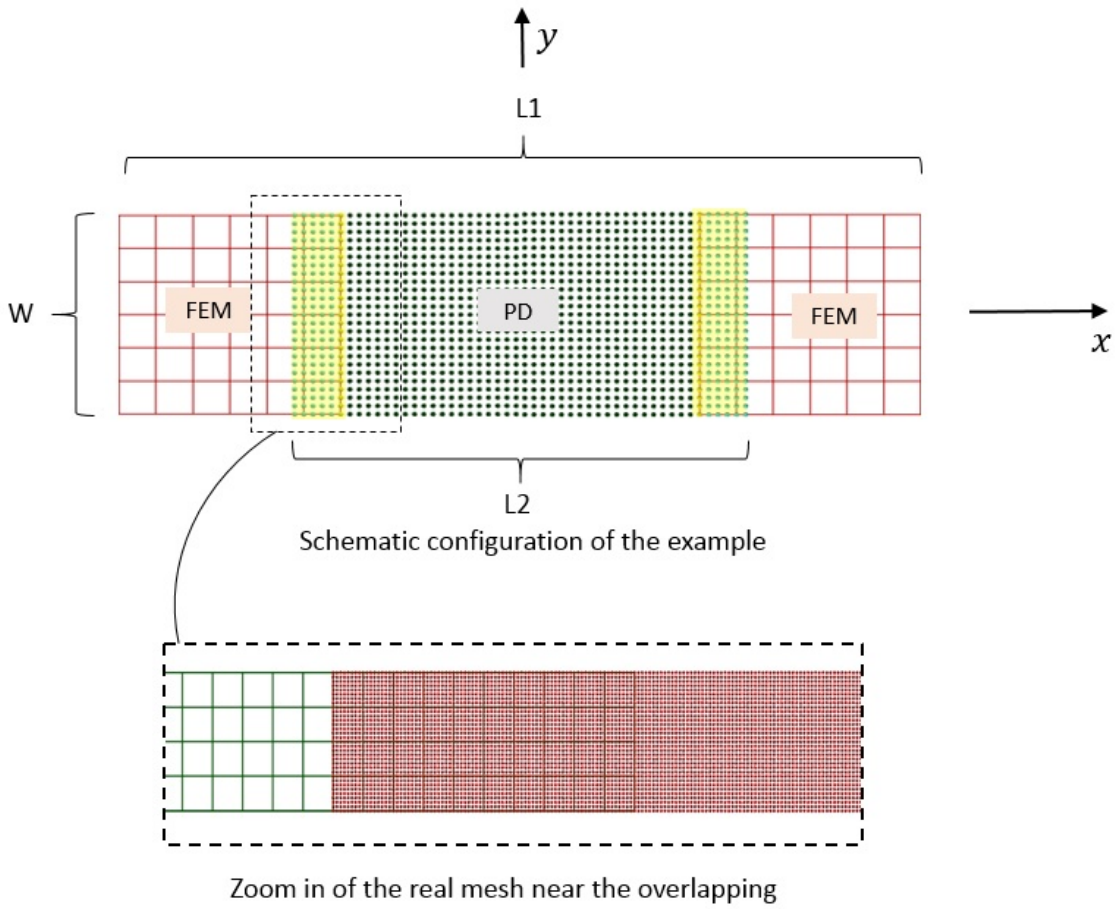

Figure 60: Configuration of the 2D examples and the zooming of the mesh around the overlapping zone.

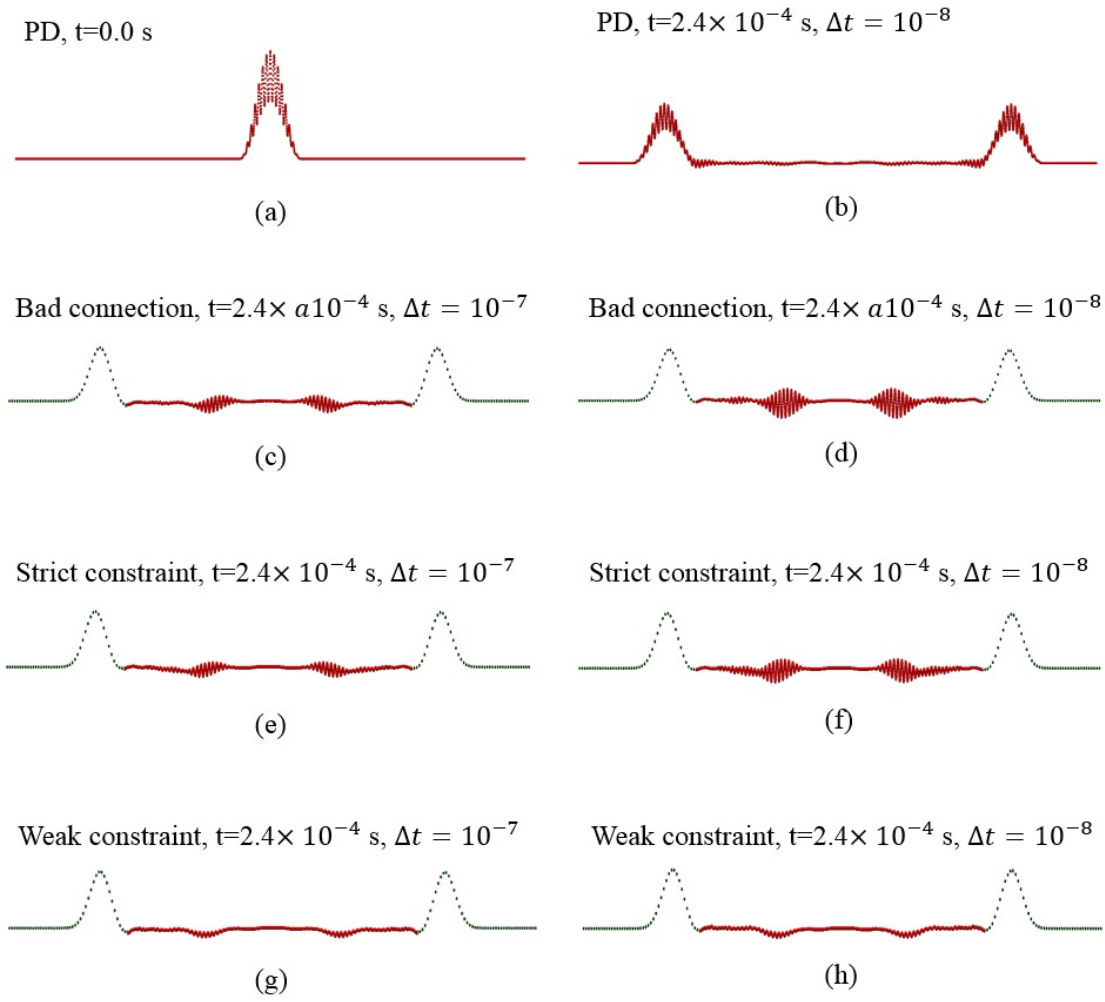

Figure 61: Snapshots of the central line of points and nodes. The height represent the displacement in the x direction. The initial waves are supposed to split and transfer to the ends. However, a bad connection causes the spurious reflection of the high frequency waves. EBDM effectively reduces the reflection.

frequency waves, only the low frequency waves can be passed to the FEM domains. When the time step is smaller, the spurious reflection is even worse. For the strict BDM, the coarse wave can be passed to the FEM, but the fine waves are reflected back to the peridynamics domain as well. Similar to the "bad connection" simulations, the spurious reflection is worse when the time step is smaller. Due to the overexerted constraint from FEM, the fine waves can not "penetrate" into the center of the overlapping zone, thus the damping can not be effectively applied to the fine waves. However, the amplitudes of the reflected waves are smaller than the ones in the "bad connection" examples.

For the enhanced BDM examples, the coarse waves are transferred to the FEM smoothly, meanwhile the fine waves are reduced by the damping. The result is not influenced by the steptime. The result is much better than the strict BDM, simply because the constraint from FEM is minimized, and the points have much more freedom to oscillate in a high frequency when they "penetrate" into the overlapping zone. Thus the high frequency movements can be detected and eliminated by the damping.

Figure 62 compares the results from the energy perspective. We plot the total strain energy, kinetic energy and Hamiltonian of all the peridynamics points (expressed as equation 74). The initial kinetic energy and strain energy are introduced by the initial waves. The energies of all the points remain constant until the split waves reach the overlapping zones. The decrease of the energy indicates that the waves are passing into the FEM domains. Finally, the energy should be reduced to zero, since the waves should be transferred to the FEM.

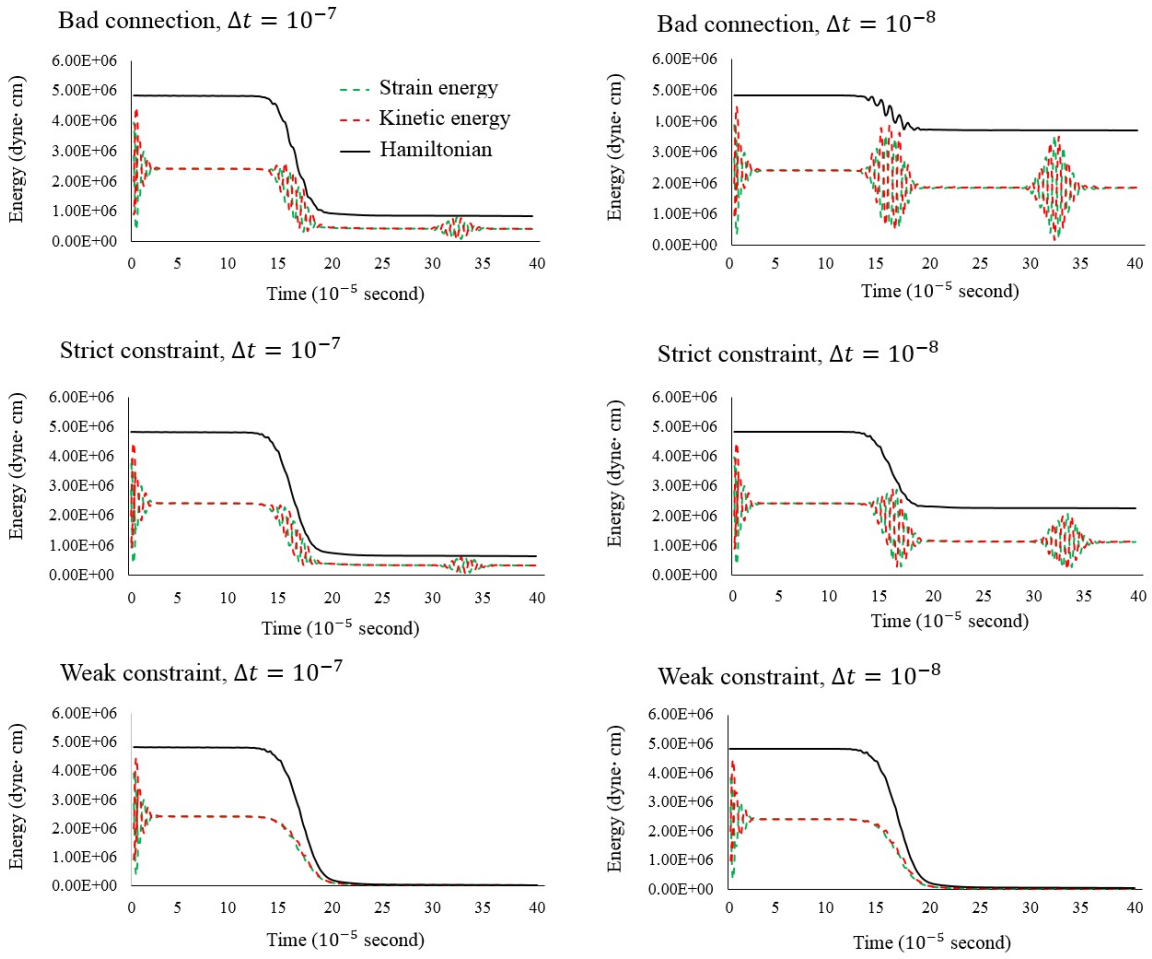

Figure 62: Energies of the peridynamics part. After the waves passed into the FEM zones, the strain energy, kinetic energy and the total Hamiltonian of the EBDM example are all zero. Meanwhile the bad connection causes redundant oscillations which are tracked inside the peridynamics zone.

If the "bad connection" is used, because of the spurious reflection, the high frequency waves are trapped inside the peridynamics domain and Hamiltonian of peridynamics doesn't become zero. There are nonnegligible oscillations between the strain energy and kinetic energy whenever the fine waves reach the overlapping zones. Note that the first group of the unexpected oscillations represent the moment that both the fine waves and coarse waves first reach the overlapping zone. The second group of the unexpected oscillations represents the moment that, after the left and right fine waves being reflected back to the center and meet each other, they get separated and transfer towards the left and right directions, and again get reflected back by the overlapping zones. It means that the energies are trapped in the peridynamics domain forever, no matter how many times the high frequency waves reach the overlapping zone. When the time step is smaller, the trapped redundant Hamiltonian is larger and the amplitude of the oscillation between the kinetic energy and strain energy is more significant.

The strict constraint shows a similar issue. But the redundant Hamiltonian is smaller and the oscillation amplitude is smaller.

Ideal results are obtained when weak constraint is used. The Hamiltonian reduce to zero when waves travel out of the peridynamics zone. Moreover, there is no energy oscillation when the waves are passing the overlapping zones, which means the waves are transferred smoothly and seamlessly. We have the same energy curves for both large and small steptimes.

7.5 Smart Layer method

Developing the overlapping meshes, indicating the edge of FEM and peridynamics and describing the nonlocal scalar functions –these steps require users to have special training of numerical analysis. Here we firstly introduce a Smart Layer method. It automatically formulate the overlapping zone, peridynamics mesh and scalar function, based on only four integer arguments given from FEM users. Thus, the BDM can be plugged into a FEM software.

Here are the steps of the Smart Layers (shown in figure 63):

1. Initially, after the FEM mesh, different parts are formulated. The Part ID to be transferred into peridynamics and overlapping zone is the first argument of Smart Layers.

2. A group of surface nodes can be simply picked by the mesh tool (for example, LS-prepost). Any elements attached to these nodes are marked as the 1st layer, then any elements attached to the i layer elements are marked as the i+1 layer, until N1 layer of elements are marked. The Group ID of the surface nodes and number of the overlapping layers N1 is the second and third argument.

3. All elements of this part transfer into peridynamics points. In this thesis, I studied two transfer criteria (figure 64). The first criterion to transfer a FEM element into the peridynamics points is called the "samescale" transfer. It transfer each FEM node into a peridynamics point. The second criterion is called the "multiscal" transfer. It transfers each Gauss point into a peridynamics point. In this study, each hexahedral element has 8 Gauss points. The overlapping elements (N layers of elements) are kept

while the unmarked elements are deleted.

4. Note that when the scalar factor α=1.0, it represents the domination of FEM. This domination from FEM to peridynamics should cover a distance, which is longer than the radius of the horizon of peridynamics. N_2 represents the number of layers that α=1.0. It is the last arguments. For the scalar factor α, it equals: (a) 1.0 if the nodes and points are within the $1 \sim N_2$ layer. (b) 0.0 if the nodes and ponts are within the N_1 layer. (c) $l_1/(l_1+l_2)$, where l_1 is the distance from the current location to its nearest α=1.0 point, l_2 is the distance from the current location to its nearest α=0.0 point. The schematic distribution of α is shown in figure 56.

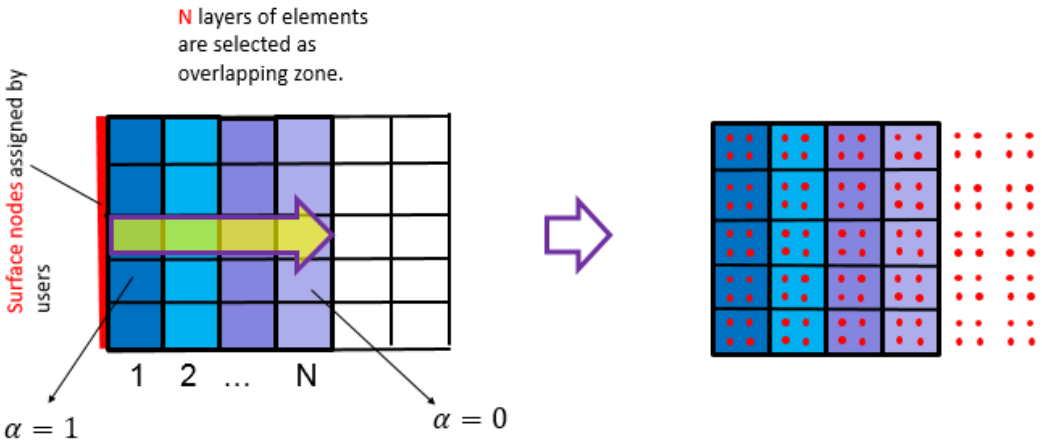

Figure 63: The schematic idea of the smart layer method, which is used to transfer a finite element part into the peridynamics points and the overlapping of the finite elements and points.

7.6 3D Examples —impact

In this section, we show an example in which a steel bar hits a steel plate. The material coefficients are shown in table 8. The mesh is shown in figure 66. A square

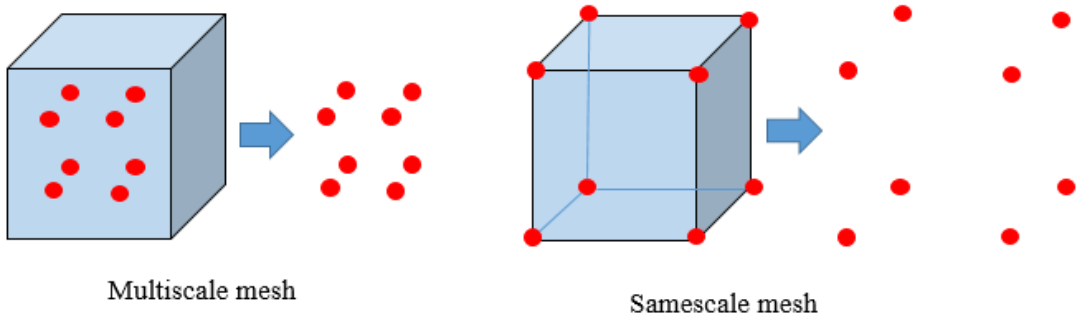

Figure 64: There are two criteria to transfer each element into points. One is to transfer the Gauss points into the peridynamics points, the other one is to transfer the nodes into the points.

Table 8: Material coefficients for the 3D impact examples, they represent the steel.

Young's Modulus	200 GPa
Poisson's ratio	0.3
mass density	7823 kg/m^3

bar ($1\times1\times10$ cm^3) with an initial velocity v_z=100 cm/s moves towards an independent plate ($1.4 \times 1.4 \times 0.2$ cm^3) at a small distance ($= 0.01$ cm) from the bar. The peridynamics is in the center (with a length of 4 cm) and the FEM are on the left and right of the bar. The time step is $\Delta t = 5.0 \times 10^{-8}$ s.

Initially, the whole mesh was generated using the FEM software Velodyne [138]. The bar was divided into three parts: the left, middle and right parts. We then used the Smart Layer method to convert the middle part into the overlapping zone and the peridynamics mesh (see figure 65). Figure 66 shows the after-transferred mesh following the multiscale transfer criterion.

After the impact, initially, the velocity on the right end reduces to a very small value, this reduction of velocity is then spread from the right end of FEM to the peridynamics zone, after that it is pread from the center peridynamics zone to the

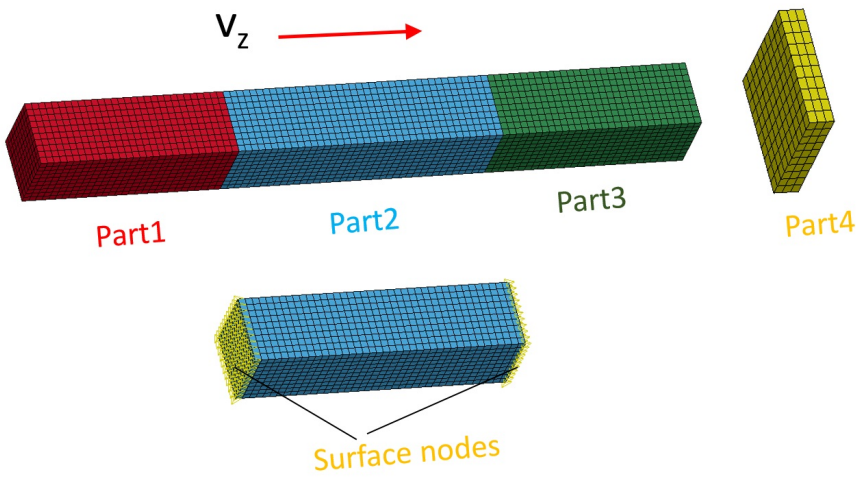

Figure 65: Initial finite element mesh from software Velodyne. The center part is to be transfered. The selected surface nodes are marked by yellow.

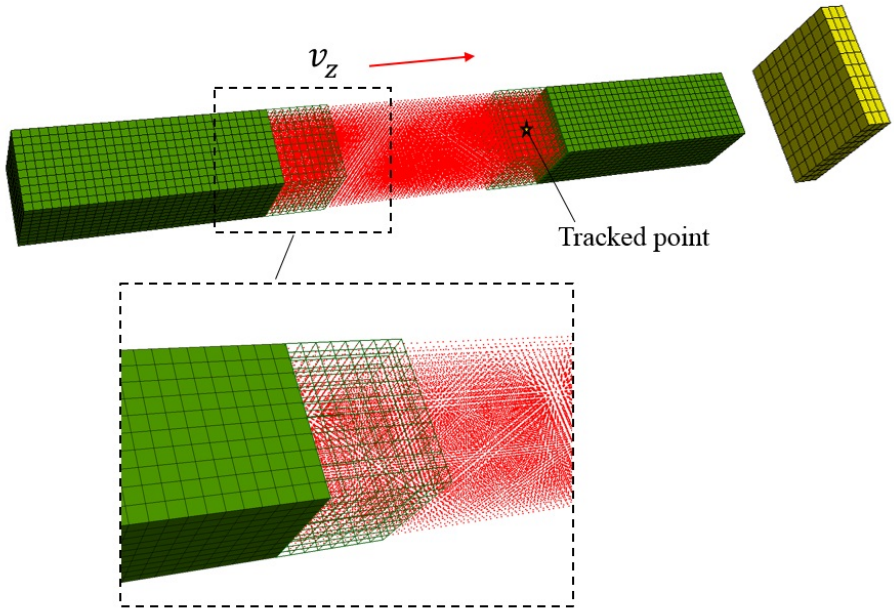

Figure 66: The multiscale mesh of FEM and peridynamics. for each overlapping zone, there are 8 layers of elements overlapping with peridynamics points. The steel bar has an initial velocity towards an independent plate.

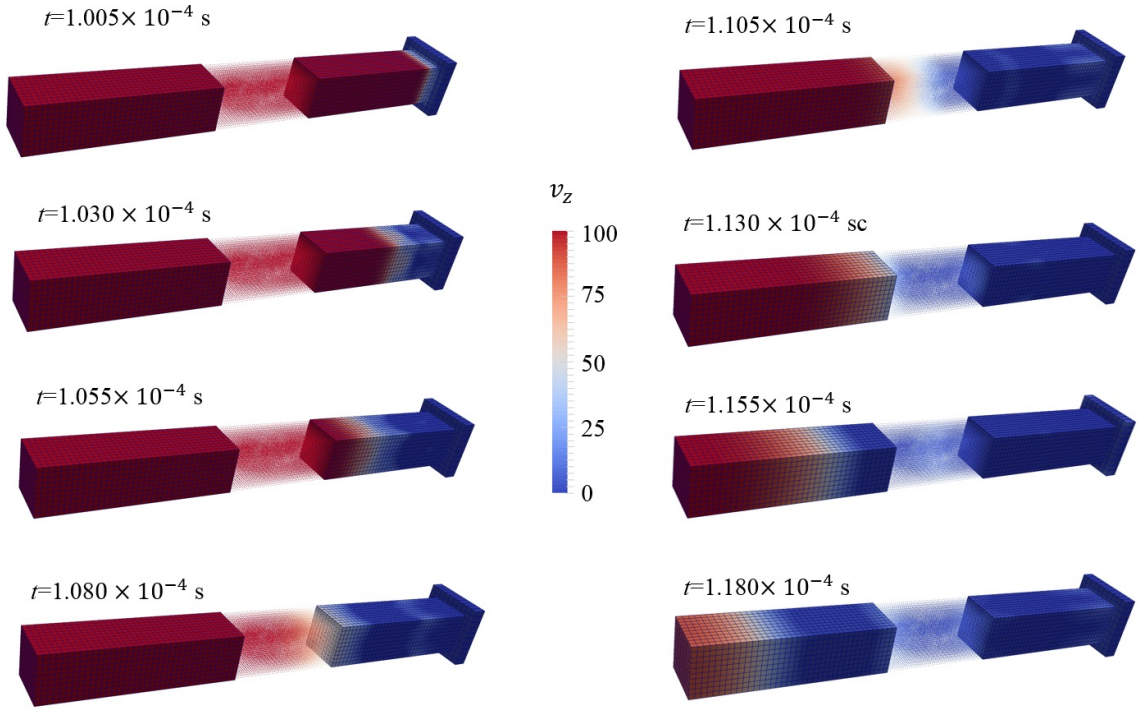

Figure 67: Snapshots of contours of velocities. The velocity reduces after the bar hits the plate. This reduction of velocity is then spreaded from the right to the left of the bar. Enhanced BDM transfers the wave smoothly.

left end of FEM; and again, from the left FEM to the peridynamics and to the right FEM. Based on the multiscale transfer criterion example, figure 67 shows 8 snapshots from $t = 1.005 \times 10^{-4}\ s$ to $t = 1.180 \times 10^{-4}\ s$ with the v_z contour. These snapshots show the progress that the waves are generated, and then smoothly transferred in the sequence of FEM-peridynamics-FEM.

To verify and compare our results, the v_z of three points are tracked and compared with the result from a pure FEM simulation (figure 68, 69 and 70). The first point is within the right overlapping zone, the second point sites in the middle of the bar, the third point is within the left overlapping zone. Using the multiscale transfer criterion, the v_z vs. time curves match the FEM results. Note that the first suddenly drop of

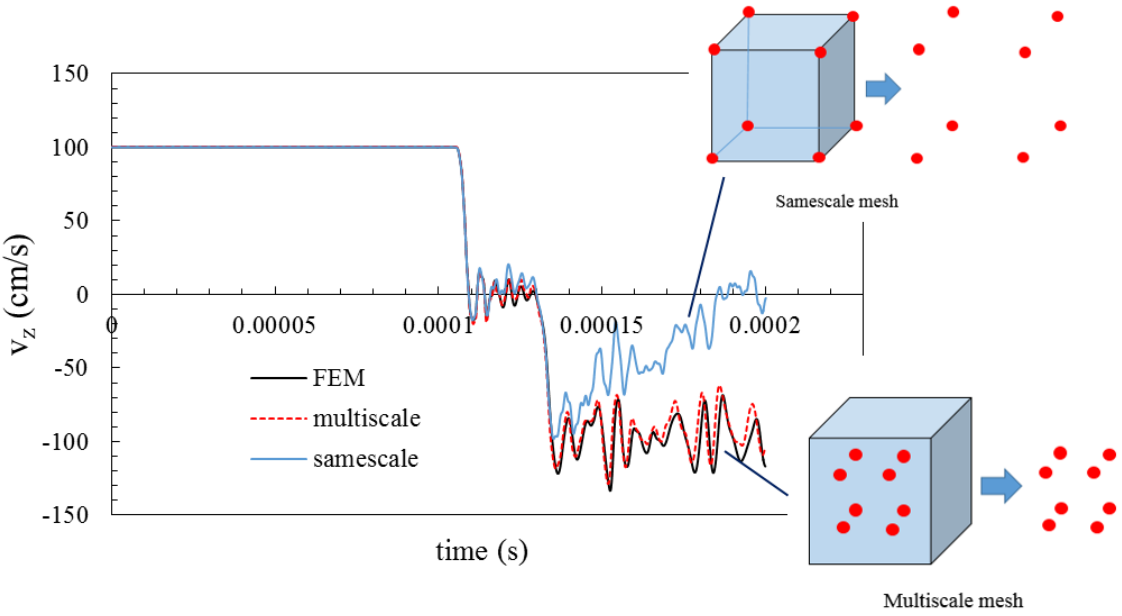

Figure 68: The time history of the velocity of a point within the right overlapping zone. The result comes from the enhanced BDM simulation is very closed to the pure FEM simulation.

the velocity represents the moment when the wave is transferred from the right FEM to peridynamics for the first time, and the second drop represents the moment that after the wave reached the left end, it goes through the left FEM and peridynamics, and reaches this point again. It shows that for the multiscale example, the waves pass through the overlapping zones for 4 times without much error. However, if the FEM nodes are simply transfered into the peridynamics points, it accumulates error during the progress when the waves pass through the peridynamics part.

This example also shows an advantage of enhanced BDM, in which the contact is simply simulated by FEM, and the error due to the surface problem of peridynamics is avoided.

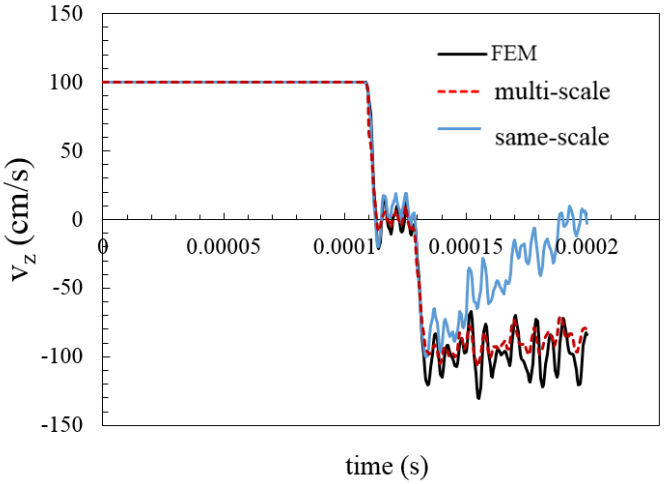

Figure 69: The time history of the velocity of a point within the middle of the peridynamics zone. The result comes from the enhanced BDM simulation is very closed to the pure FEM simulation.

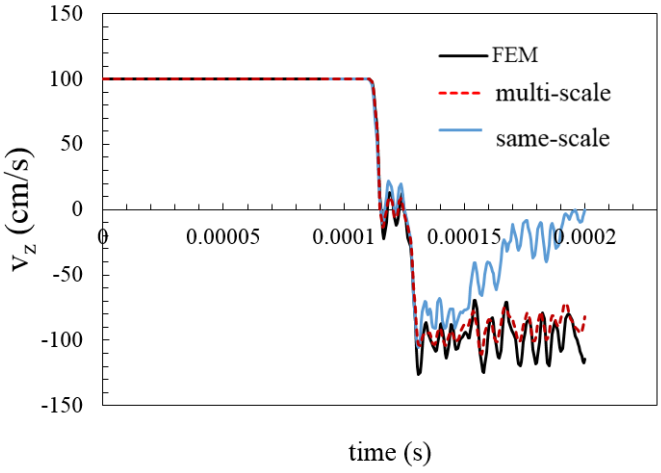

Figure 70: The time history of the velocity of a point within the left overlapping zone. The result comes from the enhanced BDM simulation is very closed to the pure FEM simulation.

Table 9: Material coefficients for the 3D mixed-mode fracture simulations, they represent the Al.

Young's Modulus	69 (GPa)
Poisson's ratio	0.29
mass density	2.3 g/cm^3
G_0	36 KJ·m^2

7.7 3D examples —mixed-mode fracture

In this section, we simulate the mixed-mode fracture phenomenon of an aluminum panel (figure 71). The Young's modulus and Poison's ratio are 29 GPa and 0.29. The critical energy release rate G_0=36 KJ/m^2. The panel with an edge crack is initially meshed with 2 parts. Based on the argued surface nodes, Part 1 is transferred into the peridynamics and overlapping zones. For peridynamics, any bond that pass through the initial edge crack are marked as broken bond. The points that are related to any broken bond are shown in red. The mixed-mode loadings are described by equation 3a and 3b in chapter 2.

We use the $\Delta K_{\text{eff}} = 10^{11} \frac{\text{dyne}\sqrt{\text{cm}}}{\text{cm}^2 \cdot \text{s}}$ as the effective stress intensity factor per second, which is equivalent to a low loading rate ($\approx$ 0.5 cm/s). The step time is $\Delta t = 5.0 \times 10^{-8}$.

Figure 77 compares the cracks propagation directions with the maximum circumferential stress criterion, which assumes that the cracks propagate along the direction which makes minimum strain energy. The results from out simulation are close to the theoretical values. Figure 76 shows the critical energy release rate for each example, all the values are close to the G_0.

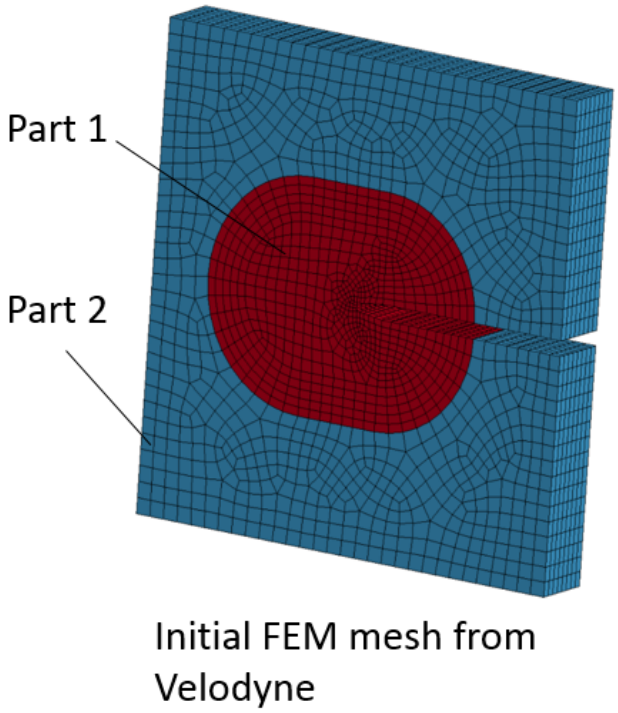

Figure 71: The initial mesh from the FEM software "Velodyne". It has two parts. Part 1, which is in the center of the panel, is to be transfered into the peridynamics points and the overlapping zone.

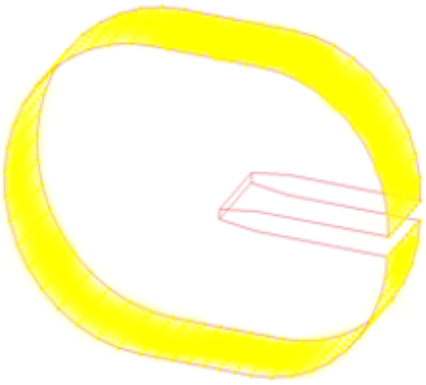

Figure 72: Users should pick a group of "surface points". They are a group of certain points on the surface of the to-be-transfered part. Based on these surface points, the overlapping zone will be developed.

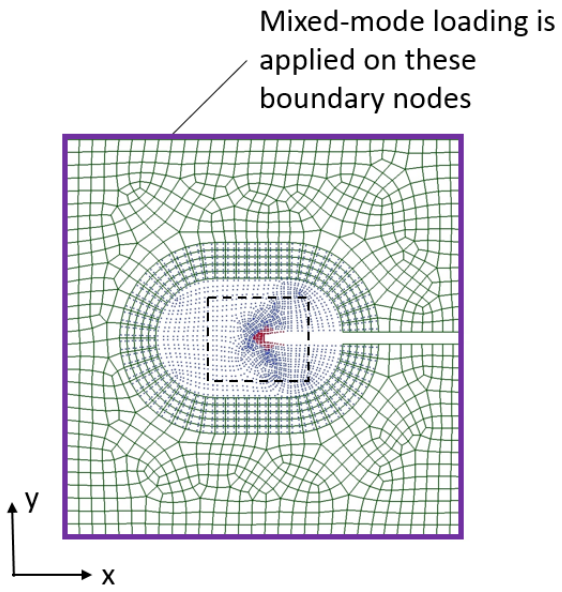

Figure 73: The mixed-mode loadings are applied on the boundary FEM nodes of the panel.

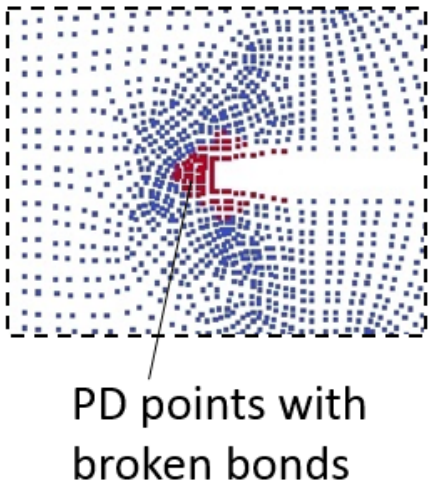

Figure 74: Zoom in around the initial crack tip. Any point who has a broken bond is marked as red.

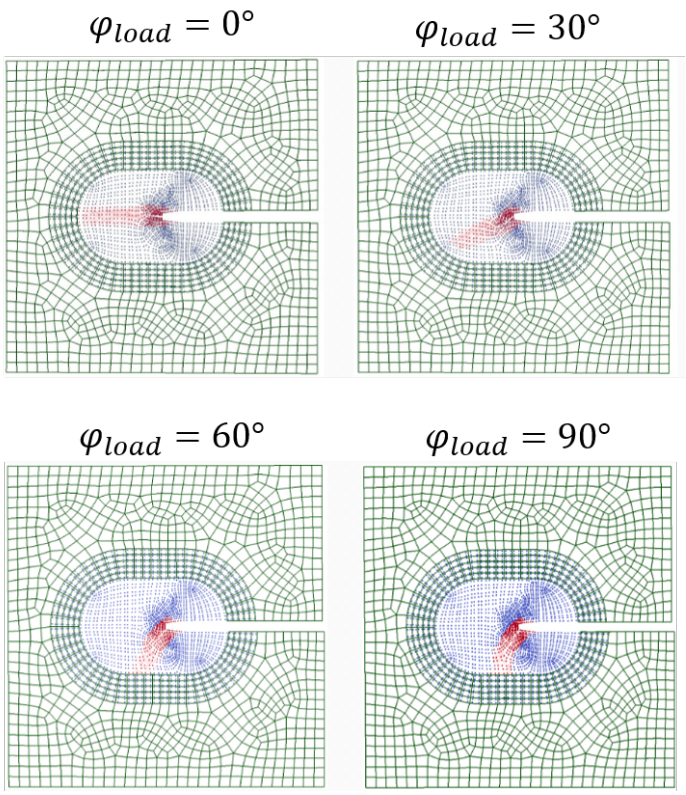

Figure 75: The crack's propagation path with the quasi-static mixed-mode loadings. The FEM mesh is shown in green, the peridynamics points are shown in blue. Especially, the broken points are shown in the red color.

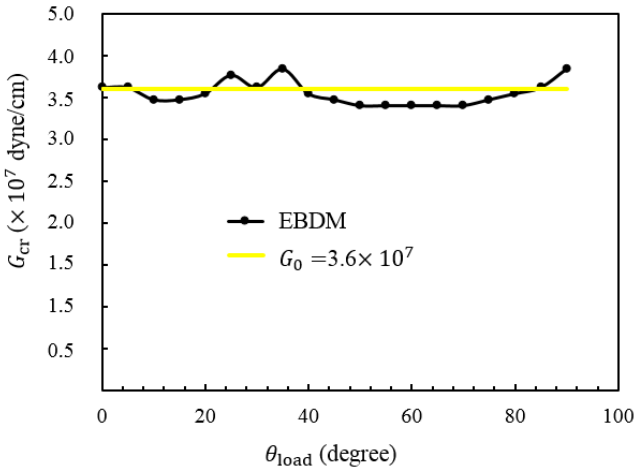

Figure 76: In a small loading rate, the critical energy release rate from the simulations are close to the critical energy release rate of the material.

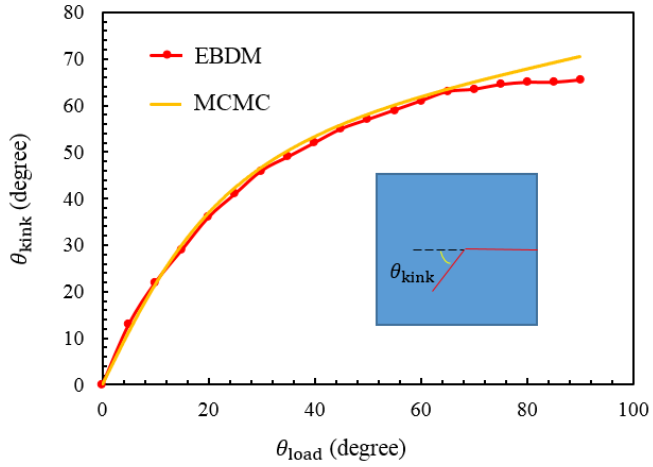

Figure 77: The crack's kinking angles match the maximum circumferential stress criterion.

7.8 Conclusion

In this study, we discussed different ways of coupling the finely meshed Peridynamics and coarsely meshed FEM. It showed the necessity of applying an advanced coupling method: if the peridynamics and FEM are badly linked, spurious reflection may occur and cause error. The enhanced weak BDM is proved to be able to detect and eliminate the high frequency waves, which are moving from peridynamics towards FEM. Differently from connecting MD with FEM, the scalar factor here is not simply a linear function. It keeps equaled to 1 for a distance. In our 2D examples, the combination of low and high frequency waves are transferred from peridynamics to FEM. It presented the spurious reflection problem, which can be reduced by enhanced BDM. Our 3D example simulated the impact and fracture problems. In the impact problem, the waves are transferred between FEM and peridynamics for 4 times with validated accuracy. In the fracture problem, our simulations are validated

by the theoretical criterion. The enhanced weak BDM can be applied to other similar local (for example, XFEM) and nonlocal (for example, MD and SPH) methods as well. Note that in the 3D example, we used the Smart Layer method to automatically transfer a FEM part into the mesh of peridynamics and the overlapping zone. We show that the multi-scale criterion to transfer a FEM element into peridynamics points performs better than same-level transfer criterion.

CHAPTER 8: SUMMARY

8.1 Atomic level studies with the molecular dynamics method

8.1.1 Fracture study of MoS_2

In the chapter 2, we have employed the molecular dynamics simulations to study the failure mechanism of the armchair and zigzag cracks in the monolayer MoS_2 sheets under the mixed fracture mode I and II loadings. Our molecular dynamics simulations predict that, similar to graphene, both the armchair and zigzag cracks prefer to propagate in the direction which makes a new zigzag crack. The direction of the cracks propagation depends on the loading phase angle. By increasing the loading phase angle, the kind angle increases. Depending on the loading phase angle and the crack chirality, the critical stress intensity factors for MoS_2 sheets are in the range of $K_{\rm cp}^{\rm cr} = 1$ and 2.5 (MPa$\sqrt{\rm m}$). A main difference between the fracture in MoS_2 sheets and the graphene is the buckling fracture. Although under mode II loading, both the graphene and the MoS_2 sheets undergo the out-of-plane deformation, buckling cracks have not been observed in graphene. This might be due to a higher stiffness of the graphene which limits the amplitude of the buckling. The amplitude of buckling in MoS_2 depends on the loading phase angle and no buckling is observed if the loading phase angle is less than 45°, and buckling cracks develop only if the loading phase angle is larger than 45°.

8.1.2 Fracture study of h-BN

In the chapter 3, we have studied the fracture properties of monolayer boron nitride sheet using molecular dynamics method. The results show that the crack edge chirality, crack tip configuration and loading phase angle affect the critical stress intensity factor and crack propagation path of the boron nitride sheet. In all the cases studied in this paper, the critical stress intensity factor corresponding to pure mode II loading is higher than that of pure mode I loading. Furthermore, all the cracks propagate along a zigzag direction, although some cracks kink during growth in which case a short path of crack growth can be along armchair direction. Besides the propagation of main crack, excessive out-of-plane deformation of BN sheet under mixed mode loading can lead to the formation of buckling cracks. Buckling cracks are more important in sheets with a zigzag crack since in such sheets buckling cracks can form when the loading phase angle is larger than 45°. In BN sheets containing armchair crack, buckling cracks can only initiate when the crack tip configuration in blunt and the loading phase angle is larger than 75°.

8.1.3 Thermal conductivity study of MoS_2

In chapter 4, we used the nonequilibrium molecular dynamics method to study the thermal conductivity with different configurations, strains, and defect densities. Our result shows,

(1) the thermal conductivity for an infinity long MoS_2 nanoribbon is about 33∼54 W/mK. The zigzag nanoribbon is more thermal conductive than armchair ribbon.

(2) The thermal conductivity of MoS_2 nanoribbon is very stable. It is insensitive

to width and strain. The nanoribbon's length and defects are the ways to tailor MoS_2 nanoribbons thermal conductivity. When more sulphur vacancies introduced, the thermal conductivity reduces moderately. Molybdenum vacancy influences the thermal conductivity more than S vacancy. At 3% vacancy density, the thermal conductivity is reduced by about 50 % (knowing that hexagonal BN can be reduced by 80% at 3% vacancy density). Larger length improves κ effectively. Even with a length of 300 nm, the nanoribbon is still almost within the ballistic region.

(3) The similarity of our result and experimental value verifies that the modified SW potential for single layer MoS_2 is precise for the analysis of the thermal conductivity of single layer MoS_2. It is because that, this potential is developed based on the phonon dispersion curve of bulk MoS_2. At the same time, the parameters of this potential also consider the nonlinear mechanical behavior of single layer MoS_2. So it is recommended for later study of single layer MoS_2 considering mechanical and thermal loadings. However, this potential also has some drawbacks. For example, it can not be used to simulate several layers of MoS_2 or bulk MoS_2; it can not represent the antisite defects like Mo-S_2 or Mo-S, which are the observed defects in single layer MoS_2 obtained using chemical vapor deposition. When we tried to simulate these defects, the system can not converge into a proper morphology after minimize.

Our simulation procedure and result can be a reference for further study of single layer MoS_2. For example, the design of relative thermoelectric materials and devices or the tailor of composite nano materials contains MoS_2 nanoribbon.

8.2 Continuum level studies with the peridynamics method

In chapter 6, we used the peridynamics method to simulate the crack's propagation under the mixed-mode loadings. Our results show that, peridynamics is able to represent the fracture phenomenon of the MoS_2 and h-BN materials at the continuum level. The crack's propagation path is not constrained by the mesh, thus it can accurately capture the crack's propagation process without remeshing. To conduct the simulation, Young's modulus, Poisson's ratio, mass density and the critical stress intensity factor of the material are required. Especially the critical stress intensity factor is used as the criterion to determine if a pair of points still have the interaction. The new crack surfaces are naturally formed without any specific criterion to predict the cracks propagation direction.

8.3 Comparison of different numerical methods

In this dissertation, different levels of the numerical simulations are studied, used and coupled . Table 10 summarizes the difference between these methods.

The molecular dynamics simulation is on the atomic level. It can capture the size effect of the nano materials. In molecular dynamics, it uses a potential function to describe the interaction forces between the atoms. Since it is a nonlocal method, an atom interacts with its neighbor atoms, hence the molecular dynamics simulation is computationally expensive. It is impossible to use the molecular dynamics to simulate macro size domains with the current computational power.

The finite element simulation is on the continuum level. FEM can not capture cracks propagation and nucleation without remeshing. However the computational

cost of FEM is significantly lower than MD.

Peridynamics is a continuum level model. In peridynamics, points interact with each other based on the force density function. Since it is a particle based method, it can simulate the fracture phenomenon without remeshing and with a high accuracy. However, since it is a nonlocal method, it is much more time consuming than the FEM. On the other hand, the force density function is obtained based on the continuum level assumption, so that the peridynamics can not capture the atomic level phenomenon.

In this dissertation, the different material properties are observed based on different scale level simulations. For the mix-mode fracture simulations of MoS_2 and h-BN, in the continuum level, the crack's propagation direction smoothly changes according to the loading phase angles. However, in the atomic level, the crack's kinking angle is always a multiple of 30°, due to the hexagonal atomic structures.

Based on the thermal conductivity quality studies, we observe that, in the atomic level, the thermal conductivity of single layer MoS_2 is effected by the configuration and chiral direction. The thermal conductivity of different nano materials – for example, h-BN, MoS_2 and graphene – are different from each other, even if their atomic structures are very similar. Under the longitudinal tensile strain, the thermal conductivity of a MoS_2 ribbon is very stable; while under the same loading, the thermal conductivity of a h-BN ribbon should increase at first and then decrease; meanwhile for a graphene, the thermal conductivity should decrease. In the continuum level, for the bulk materials, the thermal conductivity should not be influenced by the length and width of a ribbon, and there is no chirality effect. Under a tensile strain, the thermal conductivity of a bulk material should decrease.

8.4 Multi-level simulations with the EBDM coupling method

8.4.1 Coupling the molecular dynamics and finite element methods

In chapter 5, we investigated the performance of standard bridging domain method as a function of overlapping length size, the form of Lagrange multipliers discretization (strict versus weak compatibility), the type of constraint matrix (consistent versus diagonalized), the integration time step size, and the type of constraint between atomistic and continuum domain in the overlapping zone (displacement versus velocity constraint). Our numerical simulations indicate that:

(1) by increasing the width of overlapping zone, the performance of bridging domain method improves.

(2) Strict compatibility is more efficient than weak compatibility in removing spurious reflections.

(3) Performance of diagonalized constraint matrix in removing the spurious reflections is significantly better than consistent constraint matrix.

(4) By reducing the size of time step the capability of standard BDM in eliminating spurious reflections reduces.

(5) Velocity constraint is less sensitive to time integration step size and is the form of constraint which should be used.

The key contribution of the chapter is to propose the new technique to enhance the performance of bridging domain method in eliminating the spurious wave reflections at the interface of atomistic and continuum domain. In our proposed enhancement the overlapping zone plays two important roles: (a) it glues the continuum domain

to atomistic domain, and (b) it is used as a damping zone which damps the high frequency waves that cannot travel into the continuum domain. To damp the high frequency waves, we decomposed the total displacement field of atoms located within the overlapping zone into a fine and coarse scale. The fine scale oscillations correspond to the small wavelength (high frequency) components of the wave and need to be eliminated. To damp the fine scale oscillations, we included a viscous damping term in their equations of motion.

Our numerical results showed that the proposed enhancement significantly improves the capability of the bridging domain method in removing the spurious reflections. In contrast to the standard bridging domain methods, by reducing the time step size, the performance of enhanced bridging domain method improves. Also, the numerical results obtained from one and two-dimensional problems indicate that the proposed technique is capable in eliminating spurious reflections using a much smaller overlapping length than those required by the standard BDM.

8.4.2 Coupling the peridynamics and finite element methods

In chapter 7, we discussed different ways of coupling peridynamics and FEM. It showed that the necessity of applying an advanced coupling method: if the peridynamics and FEM are not appropriately linked, spurious reflection may occur. The enhanced weak BDM is proved to be able to detect and eliminate the high frequency waves, which are moving from peridynamics towards FEM. Differently from connecting MD with FEM, the scalar factor here is not simply a linear function. It keeps equaled to 1 for a distance. In our 2D examples, the combination of low and high

frequency waves are transferred from peridynamics to FEM. It presented the spurious reflection problem, which can be reduced by enhanced BDM. Our 3D example simulated the impact and fracture problems. In the impact problem, the waves are transferred between FEM and peridynamics for 4 times with validated accuracy. In the fracture problem, our simulations are validated by the theoretical criterion. The enhanced weak BDM can be applied to other similar local (for example, XFEM) and nonlocal (for example, MD and SPH) methods as well. Note that in the 3D example, we used the Smart Layer method to automatically transfer a FEM part into the mesh of peridynamics and the overlapping zone. We show that the multi-scale criterion to transfer a FEM element into peridynamics points performs better than same-level transfer criterion.

Table 10: Comparing of the three numerical methods in this thesis.

Method	simulation level	basic element	interaction	unit	local/ nonlocal	benefit	disadvantage
molecular dynamics	atomic	atom	potential function	nm, $\mathring{A}$	nonlocal	can capture atomic phenomenon	can't be applied to macro size simulations
finite element	continuum	element	material model	m, cm	local	high computational speed	can't capture atomic level phenomenon; can't represent the fracture without remeshing.
peridynamics	continuum	points	force density function	m, cm	nonlocal	without remeshing, it can represent the fracture phenomenon with high accuracy	can't capture the atomic level phenomenon; computationally expensive.

REFERENCES

[1] E. M. Abigail Agwai, Ibrahim Guven. Predicting crack initiation and propagation using xfem, czm and peridynamics: A comparative study. In *2010 Proceedings 60th Electronic Components and Technology Conference (ECTC)*, pages 1178–1185, June 2010.

[2] F. Abraham, J. Broughton, N. Bernstein, and E. Kaxiras. Spanning the length scales in dynamic simulation. *Computers in Physics*, 12:538–546, 1998.

[3] B. Alali and R. Lipton. Multiscale dynamics of heterogeneous media intheperidynamic formulation. *Journal of Elasticity*, 106(1):71–103, 2012.

[4] T. Alireza. Thermal conductivity of monolayer hexagonal boron nitride nanoribbons. *Computational Materials Science*, 108:66–71, 2015.

[5] S. S. Alireza Tabarraei, Xiaonan Wang. Mechanical properties of monolayer molybdenum difulfide. In *ASME 2014 International Mechanical Engineering Congress and Exposition*, 2014.

[6] G. Anciauxand, S. B. Ramisetti, and J. F. Molinari. A finite temperature bridging domain method for MD-FE coupling and application to a contact problem. *Computer Methods in Applied Mechanics and Engineering*, 205-208:204–212, 2012.

[7] E. Askari, F. Bobaru, R. B. Lehoucq, M. L. Parks, S. A. Silling, and O. Weckner. Peridynamics for multiscale materials modeling. *Journal of Physics: Conference Series*, 125(1):012078, 2008.

[8] S. Badia, P. Bochev, R. Lehoucq, M. Parks, J. Fish, M. A. Nuggehally, and M. Gunzburger. A force-based blending model for atomistic-to-continuum coupling. *International Journal for Multiscale Computational Engineering*, 5(5):387–406, 2007.

[9] S. Balendhran, S. Walia, H. Nili, J. Ou, S. Zhuiykov, R. Kaner, S. Sriram, M. Bhaskaran, and K. Kalantar-zadeh. Two-dimensional molybdenum trioxide and dichalcogenides. *Advanced Functional Materials*, 23:3952–3970, 2013.

[10] P. T. Bauman, H. B. Dhia, N. Elkhodja, J. T. Oden, and S. Prudhomme. On the application of the arlequin method to the coupling of particle and continuum models. *Computational Mechanics*, 42(4):511–530, 2008.

[11] T. Belytschko and S. Xiao. Coupling methods for continuum model with molecular model. *International Journal for Multiscale Computational Engineering*, 1:115–126, 2003.

[12] T. Belytschko and S. Xiao. Coupling methods for continuum model with molecular model. *International Journal for Multiscale computational engineering*, 1(1):115–126, 2003.

[13] H. Ben Dhia. Multiscale mechanical problems: the arlequin method. *Comptes Rendus de l'Academie des Sciences Series IIB Mechanics Physics Astronomy*, 326(12):899–904, 1998.

[14] S. Bhowmick and V. B. Shenoy. Effect of strain on the thermal conductivity of solids. *The Journal of Chemical Physics*, 125(16):164513, 2006.

[15] E. Biyikli, Q. Yang, and A. C. To. Multiresolution molecular mechanics: dynamics. *Computer Methods in Applied Mechanics and Engineering*, 274:42–55, 2014.

[16] F. Bobaru and M. Duangpanya. A peridynamic formulation for transient heat conduction in bodies with evolving discontinuities. *Journal of Computational Physics*, 231(7):2764 – 2785, 2012.

[17] P. O. Bouchard, F. Bay, Y. Chastel, and I. Tovena. Crack propagation modelling using an advanced remeshing technique. *Computer Methods in Applied Mechanics and Engineering*, 189(3):723–742, 2000.

[18] R. Brighenti. Buckling of cracked thin-plates under tension or compression. *Thin-Walled Structures*, 43:209–224, 2005.

[19] R. Brighenti. Influence of a central straight crack on the buckling behaviour of thin plates under tension, compression or shear loading. *International Journal of Mechanics and Materials in Design*, 6(1):73–87, 2010.

[20] L. Britnell, R. V. Gorbachev, R. Jalil, B. D. Belle, F. Schedin, M. I. Katsnelson, L. Eaves, S. V. Morozov, A. S. Mayorov, N. M. R. Peres, A. H. Castro Neto, J. Leist, A. K. Geim, L. A. Ponomarenko, and K. S. Novoselov. Electron tunneling through ultrathin boron nitride crystalline barriers. *Nano Letters*, 12(3):1707–1710, 2012.

[21] J. Broughton, F. Abraham, N. Bernstein, and E. Kaxiras. Concurrent coupling of length scales: Methodology and application. *Physical Review B*, 60:2391–2403, 1999.

[22] M. Buscema, M. Barkelid, V. Zwiller, H. S. J. van der Zant, G. A. Steele, and A. Castellanos-Gomez. Large and tunable photothermoelectric effect in single-layer mos2. *Nano Letters*, 13(2):358–363, 2013.

[23] A. Castellanos-Gomez, M. Poot, G. A. Steele, H. S. J. van der Zant, N. Agrat, and G. Rubio-Bollinger. Elastic properties of freely suspended mos2 nanosheets. *Advanced Materials*, 24(6):772–775, 2012.

[24] L. Ci, L. Song, C. Jin, D. Jariwala, D. Wu, Y. Li, A. Srivastava, Z. F. Wang, K. Storr, L. Balicas, F. Liu, and P. M. Ajayan. Atomic layers of hybridized boron nitride and graphene domains. *Nature Materials*, 9:430–435, 2010.

[25] F. Collino and C. Tsogka. Application of the perfectly matched absorbing layer model to the liner elastodayamic problem in anisotropic heterogeneous media. *Geophysics*, 66(1):294–307, 2011.

[26] R. Cooper, C. Lee, C. Marianetti, X. Wei, J. Hone, and J. Kysar. Nonlinear elastic behavior of two-dimensional molybdenum disulfide. *Physical Review B*, 87:035423, 2013.

[27] W. A. Curtin and R. E. Miller. Atomistic/continuum coupling in computational materials science. *Modelling and Simulation in Materials Science and Engineering*, 11(3):R33–R68, 2003.

[28] K. Dayal and K. Bhattacharya. Kinetics of phase transformations in the peridynamic formulation of continuum mechanics. *Journal of the Mechanics and Physics of Solids*, 54(9):1811 – 1842, 2006.

[29] C. Dean, A. Young, I. Meric, C. Lee, L. Wang, S. Sorgenfrei, K. Watanabe, T. Taniguchi, P. Kim, K. Shepard, and J. Hone. Boron nitride substrates for high-quality graphene electronics. *Nature Nanotechnolgy*, 5:722–726, 2010.

[30] P. N. Demmie and S. A. Silling. An approach to modeling extreme loading of structures using peridynamics. *Journal of Mechanics of Materials and Structures*, 2(10):1921–1945, 2007.

[31] M. Dewapriya, R. Rajapakse, and A. Phani. Atomistic and continuum modelling of temperature-dependent fracture of graphene. *International Journal of Fracture*, 187:199–212, 2014.

[32] H. B. Dhia and G. Rateau. The arlequin method as a flexible engineering design tool. *International Journal for Numerical Methods in Engineering*, 62(11):1442–1462, 2005.

[33] W. E and B. Engquist. The heterogeneous multiscale methods. *Communications in Mathematical Sciences*, 1(1):87–132, 2003.

[34] W. E, B. Engquist, and Z. Huang. Heterogeneous multiscale method: a general methodology for multiscale modeling. *Physical Review B*, 67:092101, Mar 2003.

[35] W. E, B. Engquist, and Z. Huang. Heterogeneous multiscale method: A general methodology for multiscale modeling. *Physical Review B*, 67:092101, 2003.

[36] J. X. Ebrahim Askari. Peridynamic analysis of damage and failure in composites, 2006.

[37] J. Eichler and C. Lesniak. Boron nitride (BN) and BN composites for high-temperature applications. *Journal of the European Ceramic Society*, 28(5):1105 – 1109, 2008.

[38] W. J. Evans, L. Hu, and P. Keblinski. Thermal conductivity of graphene ribbons from equilibrium molecular dynamics: Effect of ribbon width, edge roughness, and hydrogen termination. *Applied Physics Letters*, 96(20):203112, 2010.

[39] D. D. Fan, H. J. Liu, L. Cheng, P. H. Jiang, J. Shi, and X. F. Tang. Mos2 nanoribbons as promising thermoelectric materials. *Applied Physics Letters*, 105(13):133113, 2014.

[40] J. Fish, M. Nuggehally, M. Shephard, C. Picu, S. Badia, M. Parks, and M. Gunzburger. Concurrent atc coupling based on a blend of the continuum stress and the atomistic force. *Computer Methods in Applied Mechanics and Engineering*, 196:4548–4560, 2007.

[41] U. Galvanetto, T. Mudric, A. Shojaei, and M. Zaccariotto. An effective way to couple FEM meshes and peridynamics grids for the solution of static equilibrium problems. *Mechanics Research Communications*, 76:41–47, 2016.

[42] G. Giovannetti, P. A. Khomyakov, G. Brocks, P. J. Kelly, and J. van den Brink. Substrate-induced band gap in graphene on hexagonal boron nitride: Ab initio density functional calculations. *Phys. Rev. B*, 76:073103, Aug 2007.

[43] C. Goupil. *Continuum Theory andModeling of Thermoelectric Elements*. Weinheim : Wiley-VCH, 2016.

[44] R. Gracie and T. Belytschko. Concurrently coupled atomistic and xfem models for dislocatins and cracks. *International Journal for Numerical Methods in Engineering*, 78:354–378, 2009.

[45] P. Guidault and T. Belytschko. Bridging domain methods for coupled atomistic-continuum models with L2 or H1 couplings. *International Journal for Numerical Methods in Engineering*, 77:1566–1592, 2009.

[46] P. A. Guidault and T. Belytschko. On the L2 and the H1 couplings for an overlapping domain decomposition method using lagrange multipliers. *International Journal for Numerical Methods in Engineering*, 70(3):322–350, 2007.

[47] Y. D. Ha and F. Bobaru. Studies of dynamic crack propagation and crack branching with peridynamics. *International Journal of Fracture*, 162(1):229–244, 2010.

[48] Y. D. Ha and F. Bobaru. Characteristics of dynamic brittle fracture captured with peridynamics. *Engineering Fracture Mechanics*, 78(6):1156 – 1168, 2011.

[49] T. Han, Y. Luo, and C. Wang. Effects of temperature and strain rate on the mechanical properties of hexagonal boron nitride nanosheets. *Journal of Physics D: Applied Physics*, 47(2):025303, 2014.

[50] Y. Hanqing, Q. H. Jerry, F. Feifei, Z. Ting, W. Baolin, and W. Yujie. Griffith criterion for brittle fracture in graphene. *Nano Letters*, 15(3):1918–1924, 2015.

[51] J. Hong, Z. Hu, M. Probert, K. Li, D. Lv, X. Yang, L. Gu, N. Mao, Q. Feng, L. Xie, J. Zhang, D. Wu, Z. Zhang, C. Jin, W. Ji, X. Zhang, J. Yuan, and Z. Zhang. Exploring atomic defects in molybdenum disulphide monolayers. *Nat Commun*, 6:6293, 2015.

[52] M. Hu, X. Zhang, and D. Poulikakos. Anomalous thermal response of silicene to uniaxial stretching. *Phys. Rev. B*, 87:195417, May 2013.

[53] M. Hu, X. Zhang, and D. Poulikakos. Anomalous thermal response of silicene to uniaxial stretching. *Physical Review B*, 87(19):195417, 2013.

[54] Y. Hwangbo, C. Lee, S. Kim, J. Kim, K. Kim, B. Jang, H. Lee, S. Lee, S. Kim, J. Ahn, and S. Lee. Fracture characteristics of monolayer cvd-graphene. *Scientific Reports*, 4:4439, 2014.

[55] M. Iqbal, S. Khan, R. Ansari, and N. Gupta. Experimental and numerical studies of double-nosed projectile impact on aluminum plates. *International Journal of Impact Engineering*, 54:232 – 245, 2013.

[56] D. Jariwala, V. Sangwan, L. Lauhon, T. Marks, and M. Hersam. Emerging device applications for semiconducting two-dimensional transition metal dichalcogenides. *ACS Nano*, 8:1102–1120, 2014.

[57] J. A. K. Jeremy D. Seidt, Amos Gilat and J. R. Leach. High strain rate, high temperature constitutive and failure models for EOD impact scenarios, 2007.

[58] J. W. Jiang. Parametrization of stillinger-weber potential based on valence force field model: application to single-layer MoS_2 and black phosphorus. *Nanotechnology*, 26(31):315706, 2015.

[59] J.-W. Jiang, H. S. Park, and T. Rabczuk. Molecular dynamics simulations of single-layer molybdenum disulphide (mos2): Stillinger-weber parametrization, mechanical properties, and thermal conductivity. *Journal of Applied Physics*, 114(6):064307, 2013.

[60] J.-W. Jiang, J.-S. Wang, and B. Li. Young's modulus of graphene: A molecular dynamics study. *Phys. Rev. B*, 80:113405, Sep 2009.

[61] O. W. Jifeng Xu, Abe Askari and S. Silling. Peridynamics analysis of impact damage in composite laminates. *Journal of Aerospace Engineering*, 21:187–194, 2008.

[62] G. Johnso and W. Cook. "fracture characteristics of three metals subjected to various strains, strain rates, temperatures and pressures. *Engineering Fracture Mechanics*, 21(1):31–48, 1985.

[63] M. K, H. K, S. J, and H. T. Control of vallel polarization in monolayer MoS_2 by optical helicity. *Nature Nanotechnology*, 7(494-8), 2012.

[64] A. R. Khoei, R. Yasbolaghi, and S. O. R. Biabanaki. A polygonal finite element method for modeling crack propagation with minimum remeshing. *International Journal of Fracture*, 194(2):123–148, 2015.

[65] B. Kilic. *Peridynamic theory for progressive failure prediction in homogeneous and heterogeneous materials*. Thesis, The University of arizona, 2017.

[66] B. Kilic, A. Agwai, and E. Madenci. Peridynamic theory for progressive damage prediction in center-cracked composite laminates. *Composite Structures*, 90(2):141 – 151, 2009.

[67] B. Kilic and E. Madenci. Prediction of crack paths in a quenched glass plate by using peridynamic theory. *International Journal of Fracture*, 156(2):165–177, 2009.

[68] B. Kilic and E. Madenci. Structural stability and failure analysis using peridynamic theory. *International Journal of Non-Linear Mechanics*, 44(8):845 – 854, 2009.

[69] A. Kınacı, J. B. Haskins, C. Sevik, and T. Çağın. Thermal conductivity of BN-C nanostructures. *Physical Review B*, 86(11):115410, 2012.

[70] J. Knap and M. Ortiz. An analysis of the quasicontinuum method. *Journal of the Mechanics and Physics of Solids*, 49(9):1899 – 1923, 2001. The {JW} Hutchinson and {JR} Rice 60th Anniversary Issue.

[71] H. P. Komsa and A. V. Krasheninnikov. Native defects in bulk and monolayermos2from first principles. *Physical Review B*, 91(12), 2015.

[72] L. T. Kong. Phonon dispersion measured directly from molecular dynamics simulations. *Computer Physics Communications*, 182(10):2201–2207, 2011.

[73] J. Kotakoski, C. H. Jin, O. Lehtinen, K. Suenaga, and A. V. Krasheninnikov. Electron knock-on damage in hexagonal boron nitride monolayers. *Phys. Rev. B*, 82:113404, Sep 2010.

[74] Y. Kubota, K. Watanabe, O. Tsuda, and T. Taniguchi. Deep ultraviolet light-emitting hexagonal boron nitride synthesized at atmospheric pressure. *Science*, 317(5840):932–934, 2007.

[75] Q. D. Kun Zhou. Mathematical and numerical analysis of linear peridynamic models with nonlocal boundary conditions. *SIAM Journal on Numerical Analysis*, 48(5):1759–1780, 2010.

[76] S. N. Laboratories. Lammps, Feb. 2014.

[77] M. Le and R. Batra. Single-edge crack growth in graphene sheets under tension. *Computational Material Science*, 69:381–388, 2013.

[78] Y. H. Lee, X. Q. Zhang, W. Zhang, M. T. Chang, C. T. Lin, K. D. Chang, Y. C. Yu, J. T. Wang, C. S. Chang, L. J. Li, and T. W. Lin. Synthesis of large-area MoS_2 atomic layers with chemical vapor deposition. *Advanced Materials*, 24(17):2320–5, 2012.

[79] P. Li, Z. You, and T. Cui. Graphene cantilever beams for nano switches. *Applied Physics Letters*, 101:093111, 2012.

[80] T. Li. Ideal strength and phonon instability in single-layer MoS_2. *Physical Review B*, 85(23):235407, 2012.

[81] X. Li, X. Hao, M. Zhao, Y. Wu, J. Yang, Y. Tian, and G. Qian. Exfoliation of hexagonal boron nitride by molten hydroxides. *Adv Mater*, 25(15):2200–4, 2013.

[82] X. Li, K. Maute, M. L. Dunn, and R. Yang. Strain effects on the thermal conductivity of nanostructures. *Phys. Rev. B*, 81:245318, Jun 2010.

[83] X. Li, K. Maute, M. L. Dunn, and R. Yang. Strain effects on the thermal conductivity of nanostructures. *Physical Review B*, 81(24):245318, 2010.

[84] X. Li, J. Yang, and W. E. A multiscale coupling method for the modeling of dynamics of solids with application to brittle cracks. *Journal of Computational Physics*, 229:3970–3987, 2010.

[85] T. Liang, S. R. Phillpot, and S. B. Sinnott. Parametrization of a reactive many-body potential for mos systems. *Physical Review B*, 79:245110, 2009.

[86] M. Liao, Y. Wang, S. Ju, T. Lien, and L. Huang. Deformation behaviors of an armchair boron-nitride nanotube under axial tensile strains. *Journal of Applied Physics*, 110(5):054310, 2011.

[87] J. Liu, Z. Zeng, X. Cao, G. Lu, L.-H. Wang, Q.-L. Fan, W. Huang, and H. Zhang. Preparation of mos2-polyvinylpyrrolidone nanocomposites for flexible nonvolatile rewritable memory devices with reduced graphene oxide electrodes. *Small*, 8(22):3517–3522, 2012.

[88] W. Liu and J.-W. Hong. A coupling approach of discretized peridynamics with finite element method. *Computer Methods in Applied Mechanics and Engineering*, 245-246:163–175, 2012.

[89] W. Liu, H. Park, and E. Karpov. An introduction to computational nanomechanics and materials. *Computer Methods in Applied Mechanics and Engineering*, 193(17-20):1529–1578, 2004.

[90] Z. Liu, L. Ma, G. Shi, W. Zhou, Y. Gong, S. Lei, X. Yang, J. Zhang, J. Yu, K. Hackenberg, A. Babakhani, J. Idrobo, R. Vajtai, J. Lou, and P. Ajayan. In-plane heterostructures of graphene and hexagonal boron nitride with controlled domain sizes. *Nature nanotechnology*, In Press, 2013.

[91] H. B. D. Ludovic Chamoin, Serge Prudhomme and T. Oden. Ghost forces and spurious effects in atomic-to-continuum coupling methods by the arlequin approach. *International Journal for Numerical Methods in Engineering*, 83(8-9):1081–1113, 2010.

[92] R. W. Macek and S. A. Silling. Peridynamics via finite element analysis. *Finite Elements in Analysis and Design*, 43(15):1169–1178, 2007.

[93] K. Mak, K. He, J. Shan, and T. Heinz. Control of valley polarization in monolayer MoS_2 by optical helicity. *Nature Nanotechnology*, 7:494–498, 2012.

[94] K. Mak, C. Lee, J. Hone, J. Shan, and T. Heinz. Atomically thin MoS_2: A new direct-gap semiconductor. *Physical Review Letters*, 105:136805, 2010.

[95] K. Markstrom and B. Storakers. Buckling of cracked members under tension. *International Journal of Solid Mechanics*, 16:217–229, 1980.

[96] R. Miller and E. Tadmor. The quasicontinuum method: Overview, applications and current directions. *Journal of Computer-Aided Materials Design*, 9:203–239, 2002.

[97] R. E. Miller and E. B. Tadmor. Hybrid continuum mechanics and atomistic methods for simulating materials deformation and failure. *MRS Bulletin*, 32(11):920926, 2007.

[98] R. E. Miller and E. B. Tadmor. A unified framework and performance benchmark of fourteen multiscale atomistic/continuum coupling methods. *Modelling and Simulation in Materials Science and Engineering*, 17(5):053001, 2009.

[99] N. Moes, J. Dolbow, and T. Belytschko. A finite element method for crack growth without remeshing. *International journal for numerical methods in engineering*, 46:131–150, 1999.

[100] N. Moës, J. Dolbow, and T. Belytschko. A finite element method for crack growth without remeshing. *International Journal for Numerical Methods in Engineering*, 46:131–150, 1999.

[101] N. Moes, J. Dolbow, and T. Belytschko. A finite element method for crack growth without remeshing. *International Journal for Numerical Methods in Engineering*, 46:131–150, 1999.

[102] B. Mortazavi, G. Cuniberti, and T. Rabczuk. Mechanical properties and thermal conductivity of graphitic carbon nitride: A molecular dynamics study. *Computational Materials Science*, 99:285 – 289, 2015.

[103] P. Moseley, J. Oswald, and T. Belytschko. Adaptive atomistic-to-continuum modeling of propagating defects. *International Journal for Numerical Methods in Engineering*, 92(10):835–856, 2012.

[104] P. Moseley, J. Oswald, and T. Belytschko. Adaptive atomistic-continuum modeling of defect interaction with the debdm. *International Journal for Multiscale Computational Engineering*, 11(6):505–525, 2013.

[105] F. Müller-Plathe. A simple nonequilibrium molecular dynamics method for calculating the thermal conductivity. *The Journal of chemical physics*, 106(14):6082–6085, 1997.

[106] M. Osada and T. Sasaki. Two-dimensional dielectric nanosheets: Novel nanoeletronics from nanocrystal builidng blocks. *Advanced Materials*, 24:210–5528, 2012.

[107] E. Oterkus, E. Madenci, O. Weckner, S. Silling, and P. Bogert. Combined finite element and peridynamics analyses for predicting failure in a stiffeded composite curved panel with a central slot. *Composite Structure*, 94, 2012.

[108] B. Partoens and F. M. Peeters. From graphene to graphite: Electronic structure around the k point. *Phys. Rev. B*, 74:075404, Aug 2006.

[109] Q. Peng, A. R. Zamiri, W. Ji, and S. De. Elastic properties of hybrid graphene/boron nitride monolayer. *Acta Mechanica*, 223:2591–2596, 2012.

[110] F. Perkins, A. Friedman, E. Cobas, P. Campbell, G. Jernigan, and B. Jonker. Chemical vapor sensing with monolayer MoS_2. *ACS Nano*, 13:668–673, 2013.

[111] R. Picu, T. Borca-Tasciuc, and M. Pavel. Strain and size effects on heat transport in nanostructures. *Journal of applied physics*, 93(6):3535–3539, 2003.

[112] S. Prudhomme, H. B. Dhia, P. T. Bauman, N. Elkhodja, and J. T. Oden. Computational analysis of modeling 390 error for the coupling of particle and continuum models by the arlequin method. *Computer Methods in Applied Mechanics and Engineering*, 197(41):3339–3409, 2008.

[113] B. Radisavljevic, A. Radenovic, J. Brivio, V. Giacometti, and A. Kis. Single-layer MoS_2 transistors. *Nature Nanotechnology*, 6(147-50), 2011.

[114] M. Rafiee, J. Rafiee, I. Srivastava1, Z. Wang, H. Song, Z. Yu, and N. Koratkar. Fracture and fatigue in graphene nanocomposites. *Small*, 6:179–183, 2008.

[115] B. Ren, H. Fan, G. L. Bergel, R. A. Regueiro, X. Lai, and S. Li. A peridynamicsSPH coupling approach to simulate soil fragmentation induced by shock waves. *Computational Mechanics*, 55(2):287–302, 2015.

[116] R. Ross and O. Sandberg. The thermal conductivity of four solid phases of NH_4F, and a comparison with H_2O. *Journal of Physics C: Solid State Physics*, 11(4):667, 1978.

[117] R. G. Ross and O. Sandberg. The thermal conductivity of four solid phases of nh_4f, and a comparison with h 2 o. *Journal of Physics C: Solid State Physics*, 11(4):667, 1978.

[118] R. Rudd and J. Broughton. Coarse-grained molecular dynamics and the atomic limit of finite elements. *Physical Review B*, 58:R5893–R5896, 1998.

[119] R. Rudd and J. Broughton. Coarse-grained molecular dynamics: Nonlinear finite elements and finite temperature. *Physical Review B*, 72:144104, 2005.

[120] A. Sadeghirad and F. Liu. A three-layer-mesh bridging domain for coupled atomisticcontinuum simulations at finite temperature: Formulation and testing. *Computer Methods in Applied Mechanics and Engineering*, 268:299–317, 2014.

[121] A. Sadeghirad and A. Tabarraei. A damping boundary condition for coupled atomistic–continuum simulations. *Computational Mechanics*, 52(3):535–551, 2013.

[122] E. Saether, V. Yamakov, and E. Glaessgen. An embedded statistical method for coupling molecular dynamics and finite element analyses. *International Journal for Numerical Methods in Engineering*, 78:1292–1319, 2009.

[123] S. Sahoo, A. P. S. Gaur, M. Ahmadi, M. J. F. Guinel, and R. S. Katiyar. Temperature-dependent raman studies and thermal conductivity of few-layer MoS_2. *The Journal of Physical Chemistry C*, 117(17):9042–9047, 2013.

[124] P. K. Schelling, S. R. Phillpot, and P. Keblinski. Comparison of atomic-level simulation methods for computing thermal conductivity. *Phys. Rev. B*, 65:144306, Apr 2002.

[125] W. Sekkal, B. Bouhafs, H. Aourag, and M. Certier. Molecular-dynamics simulation of structural and thermodynamic properties of boron nitride. *Journal of Physics: Condensed Matter*, 10(23):4975, 1998.

[126] C. Sevik, A. Kinaci, J. B. Haskins, and T. Çağ ın. Characterization of thermal transport in low-dimensional boron nitride nanostructures. *Physical Review B*, 84:085409, Aug 2011.

[127] A. Shahani and M. A. Fasakhodi. Finite element analysis of dynamic crack propagation using remeshing technique. *Materials & Design*, 30(4):1032–1041, 2009.

[128] G. Sih and Y. Lee. Tensile and compressive buckling of plates weakened by cracks. *Theoretical and Applied Fracture Mechanics*, 6:129–138, 1986.

[129] S. Silling and E. Askari. A meshfree method based on the peridynamic model of solid mechanics. *Computers & Structures*, 83(1718):1526 – 1535, 2005. Advances in Meshfree Methods.

[130] S. A. Silling and R. B. Lehoucq. Convergence of peridynamics to classical elasticity theory. *Journal of Elasticity*, 93(1):13, 2008.

[131] S. A. Silling, O. Weckner, E. Askari, and F. Bobaru. Crack nucleation in a peridynamic solid. *International Journal of Fracture*, 162(1):219–227, 2010.

[132] J. C. Simo, J. Oliver, and F. Armero. An analysis of strong discontinuities induced by strain-softening in rateindependent inelastic solids. *Computational Mechanics*, 12:277–296, 1993.

[133] A. Tabarraei, S. Shadalou, and J.-H. Song. Mechanical properties of graphene nanoribbons with disordered edges. *Computational Materials Science*, 96:10–19, 2015.

[134] A. Tabarraei and X. Wang. Anomalous thermal conductivity of monolayer boron nitride. *applied physics letters*, 108:181904–1 181904–5, 2016.

[135] A. Tabarraei, X. Wang, A. Sadeghirad, and J. H. Song. An enhanced bridging domain method for linking atomistic and continuum domains. *Finite Elements in Analysis and Design*, 92:36–49, 2014.

[136] E. Tadmor, M. Ortiz, and R. Phillips. Quasicontinuum analysis of defects in solids. *Philosophical Magazine A*, 73:1529–1563, 1996.

[137] A. Taube, J. Judek, A. Lapinska, and M. Zdrojek. Temperature-dependent thermal properties of supported MoS_2 monolayers. *ACS Appl Mater Interfaces*, 7(9):5061–5, 2015.

[138] C. Technology, 2009.

[139] J. Tersoff. New empirical approach for the structure and energy of covalent systems. *Physical Review B*, 37:6991–7000, Apr 1988.

[140] J. Tersoff. New empirical approach for the structure and energy of covalent systems. *Physical Review B*, 37(12):6991, 1988.

[141] A. To and S. Li. Perfectly matched multiscale simulations. *Physical Review B*, 72:035414, 2005.

[142] V. Verma, V. K. Jindal, and K. Dharamvir. Elastic moduli of a boron nitride nanotube. *Nanotechnology*, 18(43):435711, 2007.

[143] G. Wagner, E. Karpov, and W. Liu. Molecular dynamics boundary conditions for periodically repeating atomic lattices. *Computer Methods in Applied Mechanics and Engineering*, 193:1579–1601, 2004.

[144] G. Wagner and W. Liu. Coupling of atomistic and continuum simulations using a bridging scale decomposition. *Journal of Computational Physics*, 190:249–274, 2003.

[145] H. Wang, L. Yu, Y.-H. Lee, Y. Shi, A. Hsu, M. L. Chin, L.-J. Li, M. Dubey, J. Kong, and T. Palacios. Integrated circuits based on bilayer mos2 transistors. *Nano Letters*, 12(9):4674–4680, 2012.

[146] Q. Wang, K. Kalantar-Zadeh, A. Kis, J. Coleman, and M. Strano. Electronics and optoelectronics of two-dimensional transition metal dichalcogenides. *Nature Nano Technology*, 7:699–712, 2012.

[147] S. Wang, Z. Qin, G. S. Jung, F. J. Martin-Martinez, K. Zhang, M. J. Buehler, and J. H. Warner. Atomically sharp crack tips in monolayer MoS_2 and their enhanced toughness by vacancy defects. *ACS Nano*, 10(11):9831–9839, 2016.

[148] X. Wang, A. Tabarraei, and D. E. Spearot. Fracture mechanics of monolayer molybdenum disulfide. *Nanotechnology*, 26(17):175703, 2015.

[149] N. Wei, L. Xu, H. Wang, and J. Zheng. Strain engineering of thermal conductivity in graphene sheets and nanoribbons: a demonstration of magic flexibility. *Nanotechnology*, 22(10):105705, 2011.

[150] F. B. Wenke Hu, Youn Doh Ha. Modeling dynamic fracture and damage in a fiber-reinforced composite lamina with peridynamics. *Journal for Multiscale Computational Engineering*, 9:707–726, 2011.

[151] F. B. Wenke Hu, Youn Doh Ha. Peridynamic model for dynamic fracture in unidirectional fiber-reinforced composites. *Computer Methods in Applied Mechanics and Engineering*, 217-220:247–261, Apr 2012.

[152] S. Xiao and T. Belytschko. A bridging domain method for coupling continua with molecular dynamics. *Computer Methods in Applied Mechanics and Engineering*, 193:1645–1669, 2004.

[153] S. P. Xiao and T. Belytschko. A bridging domain method for coupling continua with molecular dynamics. *Computer Methods in Applied Mechanics and Engineering*, 193(17-20):1645–1669, 2004.

[154] M. Xu and T. Belytschko. Conservation properties of the bridging domain method for coupled molecular/continuum dynamics. *International Journal for Numerical Methods in Engineering*, 76:278–294, 2008.

[155] M. Xu, A. Tabarraei, J. Paci, and T. Belytschko. Coupled quantum/continuum mechanics study of graphene fracture. *Internation Journal of Fracture*, 173:163–173, 2012.

[156] M. Xu, A. Tabarraei, J. T. Paci, J. Oswald, and T. Belytschko. A coupled quantum/continuum mechanics study of graphene fracture. *International Journal of Fracture*, 173(2):163–173, 2012.

[157] X. Xu, L. F. C. Pereira, Y. Wang, J. Wu, K. Zhang, X. Zhao, S. Bae, T. B. Cong, R. Xie, J. T. L. Thong, B. H. Hong, K. P. Loh, D. Donadio, B. Li, and B. Özyilmaz. Length-dependent thermal conductivity in suspended single-layer graphene. *Journal of Applied Physics*, 114(5):053506, 2013.

[158] R. Yan, J. R. Simpson, S. Bertolazzi, J. Brivio, M. Watson, X. Wu, A. Kis, T. Luo, A. R. Hight Walker, and H. G. Xing. Thermal conductivity of monolayer molybdenum disulfide obtained from temperature-dependent raman spectroscopy. *ACS Nano*, 8(1):986–93, 2014.

[159] J. T. Ye, Y. J. Zhang, R. Akashi, M. S. Bahramy, R. Arita, and Y. Iwasa. Superconducting dome in a gate-tuned band insulator. *Science*, 338(6111):1193–1196, 2012.

[160] Z. Zeng, Z. Yin, X. Huang, H. Li, Q. He, G. Lu, F. Boey, and H. Zhang. Single-layer semiconducting nanosheets: High-yield preparation and device fabrication. *Angewandte Chemie International Edition*, 50:11093–11097, 2011.

[161] Z. Zeng, Z. Ying, X. Huang, H. Li, Q. He, G. Lu, F. Boey, and H. Zhang. Single-layer semiconductiong nanosheets: high-yield preparation and device fabrication. *Angewandte Chemie International Edition*, 50:11093–7, 2011.

[162] B. Zhang, L. Mei, and H. Xiao. Nanofracture in graphene under complex mechanical stresses. *Applied Physics Letter*, 101:121915, 2012.

[163] M. Zhang, R. C. T. Howe, R. I. Woodward, E. J. R. Kelleher, F. Torrisi, G. Hu, S. V. Popov, J. R. Taylor, and T. Hasan. Solution processed mos2-pva composite for sub-bandgap mode-locking of a wideband tunable ultrafast er:fiber laser. *Nano Research*, 8(5):1522–1534, 2015.

[164] S. Zhang, R. Khare, Q. Lu, and T. Belytschko. A bridging domain and strain computation method for coupled atomistic-continuum modelling of solids. *International Journal for numerical methods in engineering*, 70:913–933, 2007.

[165] S. Zhang, S. Mielke, R. Khare, D. Troya, R.S., G. Schatz, and T. Belytschko. Mechanics of defects in carbon nanotubes: atomistic and multiscale simulations. *Physical Review B*, 71:115403, 2005.

[166] W. Zhou, X. Zou, S. Najmaei, Z. Liu, Y. Shi, J. Kong, J. Lou, P. M. Ajayan, B. I. Yakobson, and J. C. Idrobo. Intrinsic structural defects in monolayer molybdenum disulfide. *Nano Lett*, 13(6):2615–22, 2013.

[167] J. M. Ziman. *Electrons and phonons: the theory of transport phenomena in solids*. Carendon Press, Oxford, UK, 2001.